TECHNISCHE UNIVERSITÄT MÜNCHEN

Fakultät für Medizin

T-cell receptor avidity of polyclonal CD8$^+$ T-cell populations

Philipp Lückemeier

Vollständiger Abdruck der von der Fakultät für Medizin der Technischen Universität München zur Erlangung des akademischen Grades eines

Doktors der Medizinischen Wissenschaft (Dr. med. sci.)

genehmigten Dissertation.

Vorsitz: Prof. Dr. Klaus-Peter Janssen

Prüfer*innen der Dissertation:

1. Prof. Dr. Dirk H. Busch

2. Prof. Dr. Gabriele Multhoff

Die Dissertation wurde am 13.01.2023 bei der Technischen Universität München eingereicht und durch die Fakultät für Medizin am 19.04.2023 angenommen.

Parts of this thesis have previously been published:

Lückemeier, P., K. L. Molter, S. Jarosch, P. Huppertz, A. Purcarea, M. J. P. Effenberger, M. Nauerth, E. D'Ippolito, K. Schober, and D. H. Busch. 2022. Global k_{off}-rates of polyclonal T-cell populations merge subclonal avidities and predict functionality. Eur. J. Immunol., 52: 582-596.

Schober, K., F. Voit, S. Grassmann, T. R. Müller, J. Eggert, S. Jarosch, B. Weißbrich, P. Hoffmann, L. Borkner, E. Nio, L. Fanchi, C. R. Clouser, A. Radhakrishnan, L. Mihatsch, P. Lückemeier, J. Leube, G. Dössinger, L. Klein, M. Neuenhahn, J. D. Oduro, L. Cicin-Sain, V. R. Buchholz, and D. H. Busch. 2020. Reverse TCR repertoire evolution toward dominant low-affinity clones during chronic CMV infection. Nature immunology. 21: 434-441.

Table of Contents

Abbreviations

APC	Allophycocyanin *or* antigen-presenting cell
A2	APL with amino acid sequence SAINFEKL
allo-HCT	Allogeneic hematopoietic stem cell transplantation
APL	Altered peptide ligand
β2m	Human β2-microglobulin
CD	Cluster of differentiation
ddH_20	Milli-Q prepared water (resistance of 18,2 MΩ·cm)
DMSO	Dimethyl sulfoxide
FCM	Flow cytometry
FCS	Fetal calf serum
HLA	Human leukocyte antigen
IFN-γ	Interferon-γ
GvHD	Graft vs. host disease
mAb	Monoclonal antibody
mβ2m	Murine β2-microglobulin
MFI	Mean fluorescence intensity
MHC (I / II)	Major histocompatibility complex (class I / class II)
NTA	Ni^{2+}-nitrilotriacetic acid
PE	Phycoerythrin
PBMC	Peripheral blood mononuclear cell
PBS	Phosphate buffered saline
pHLA	Peptide-human leukocyte antigen
PMA	Phorbol-12-myristat-13-acetat
pMHC (I / II)	Peptide-major histocompatibility complex (class I / class II)
Q4	APL with amino acid sequence SIIQFEKL
rpm	Rounds per minute
RTCA	Real Time Cell Analyzer
SPF	Specific-Pathogen-Free
T_{CM}	Central memory T cells
T_{EM}	Effector memory T cells
T_{EC}	Effector T cells
T_{scm}	Stem cell memory T cells

TIL	Tumor-infiltrating lymphocytes
TNF	Tumor necrosis factor
TRBV	T-cell receptor beta variable#
TZR	T-Zell-Rezeptor
Y0	Y-intercept of a graph
Y3	APL with amino acid sequence SIYNFEKL
YFV	Yellow fever virus

List of Figures

1. Zusammenfassung / Summary

1.1 Zusammenfassung

Die Avidität von T-Zell-Rezeptoren (TZR) gegenüber ihrem Antigen ist von entscheidender Bedeutung für die Effektivität von T-Zellen in ihrer Immunreaktion auf Infektionen und maligne Prozesse. Eine hohe TZR-Avidität ist mit höherer T-Zell-Funktionalität assoziiert, während T-Zellen mit niedriger Avidität einzigartige Rollen in der Immunantwort übernehmen. Dies spiegelt sich in der Breite der TZR-Avidität und der Polyklonalität von physiologischen Immunantworten wider. Auch ein Großteil der T-Zell-Therapeutika wie z.B. virusspezifische T-Zellen oder Tumor-infiltrierende Lymphozyten sind polyklonal. Die meisten Studien über die Auswirkungen unterschiedlicher TZR-Avidität haben jedoch ausschließlich monoklonale Populationen wie Zelllinien oder transgene T-Zellen untersucht. Gründe dafür sind u.a. die Heterogenität und wechselnde Qualität der Assays zur Analyse der TZR-Avidität polyklonaler Populationen.

Ziel dieser Arbeit war es, die TZR-Avidität von polyklonalen $CD8^+$ T-Zell-Populationen mit Hilfe des durchflusszytometrischen Streptamer-basierten TZR-Liganden-k_{off}-Raten-Assays zu quantifizieren und mit ihrer Funktionalität zu korrelieren. Vorarbeiten haben dies bereits mit der mikroskopischen Version des Assays an Klonen und Zelllinien gezeigt und die durchflusszytometrische Version für humane Zellen etabliert.

In dieser Arbeit wurde das durchflusszytometrische Assay zunächst für monoklonale murine T-Zell-Populationen etabliert und dann auf polyklonale Infekt-induzierte Populationen ausgeweitet. Die so gewonnenen TZR-Liganden-Dissoziationen erlaubten die Messung von "globalen" Dissoziationsraten (k_{off}-Raten), die ein neues, ganzheitliches Maß für die TZR-Avidität polyklonaler Populationen darstellen. Dafür wurde auch ein Analysemodell für Dissoziationen von polyklonalen Populationen geschaffen. Mit Hilfe von Mischpopulationen aus einer TZR-Klon-Bibliothek konnte gezeigt werden, dass Subpopulationen mit unterschiedlicher Avidität gleichsam und proportional zu ihren k_{off}-Raten und Frequenzen auf die globalen k_{off}-Raten einwirken.

Um die Assoziation zwischen globalen k_{off}-Raten und Funktionalität zu untersuchen, wurde ein Infektionsmodell mit polyklonalen T-Zell-Populationen mit robust abgestufter TZR-Avidität gegenüber dem OVA-Epitop entworfen. Infektionen mit Listerien-Stämmen, die leicht veränderte Aminosäuresequenzen (genannt "APL") des OVA-Epitops exprimieren, induzierten in Mäusen große $CD8^+$ T-Zellpopulationen mit Kreuzreaktivität gegenüber OVA. Für jedes dieser APL-Epitope wurden Assay-Reagenzien hergestellt, mit denen vergleichbare globalen k_{off}-Raten und damit vergleichbare inhärente strukturelle Avidität in diesen Populationen nachgewiesen werde konnte. In Bezug auf das OVA-Epitop zeigten die APL-induzierten Populationen jedoch je nach APL-Epitop eine stark abgestufte TZR-Avidität. Dieselbe Abstufung fand sich auch in der als "funktionelle Avidität" bezeichneten Peptidempfindlichkeit gegenüber OVA, welche stark mit den globalen k_{off}-Raten korrelierte. Die Immunphänotypen der Populationen und ihre Peptidsensitivität gegenüber dem kognitiven Epitop waren vergleichbar, wodurch eine inhärent geringere Antigenreaktivität als Störfaktor ausgeschlossen werden konnte. Auch die Fähigkeit der unterschiedlich induzierten T-Zellen, OVA-exprimierende Tumore abzutöten, war in vitro stark positiv mit ihren globalen k_{off}-Raten korreliert und folgte der zuvor beobachteten TZR-Aviditätsabstufung in in vivo Tumorprotektions-Experimenten in Mäusen.

In einem translationalen Ansatz wurden schließlich humane T-Zell-Klone verwendet, um die murinen Ergebnisse zu validieren. Anschließend konnte eine Methodik entwickelt werden, mit der die globalen k_{off}-Raten von Mischpopulationen aus den Dissoziationsparametern der einzelnen Klone vorhergesagt werden können. Diese Methodik könnte die Entwicklung von T-

Zell-Populationen mit maßgeschneiderter globalen k_{off}-Rate aus T-Zell-Bibliotheken ermöglichen.

Insgesamt etablieren diese Ergebnisse die globale TZR-Liganden-k_{off}-Rate als neues Maß für die durchschnittliche strukturelle Avidität polyklonaler CD8+ T-Zellpopulationen. Ihre starke Korrelation mit mehreren funktionellen Parametern und ihre schnelle Anwendbarkeit machen sie zu einem vielversprechenden Prognoseinstrument für die klinische Forschung. Dabei ebnet die umfassende Charakterisierung und die hier nachgewiesene Vorhersagbarkeit der globalen k_{off}-Rate aus einzelnen T-Zell-Klonen den Weg für deren Nutzung für polyklonale T-Zell-Therapeutika.

1.2 Summary

T-cell receptor avidity is a crucial factor in the efficacy of the T-cell response to malignancies and infections. Higher TCR avidity has been linked to superior T-cell functionality while low-avidity T cells take on distinct roles in the immune response. This is reflected in the breadth of TCR avidity in physiological immune responses through polyclonality. Likewise, most T-cell therapeutics in clinical applications are polyclonal, *e.g.*, virus-specific T cells and tumor-infiltrating lymphocytes. Most studies that investigated the impact of TCR avidity, however, have exclusively analyzed monoclonal populations like cell lines or transgenic T-cell populations. Moreover, assays to analyze TCR avidity have been non-uniform and of varying quality, especially in the polyclonal setting.

This work aimed to utilize the flow cytometric streptamer-based TCR-ligand k_{off}-rate assay to assess the TCR avidity of polyclonal $CD8^+$ T-cell populations and link it to their functionality. Prior to this work, the microscopic version of the assay was shown to correlate with functionality in clones and cell lines, and the flow cytometric version was newly implemented. Herein, the flow-cytometric assay was applied to polyclonal populations. An analysis model of exponential decay curve fitting was developed for polyclonal populations. Their TCR-ligand dissociations yielded the herein termed 'global' k_{off}-rates as a consolidating measure of TCR avidity of polyclonal populations. Global k_{off}-rates were further analyzed to ensure unbiased integration of low- and high-avidity subpopulations. To this end, multiple pre-characterized clones from a TCR library were carefully mixed to reveal that global k_{off}-rates merge subclonal avidities according to their k_{off}-rates and frequencies without bias.

To investigate whether the global k_{off}-rates would corroborate the postulated effects of TCR avidity on functionality, an infection model inducing polyclonal T-cell populations with robustly tiered TCR avidity towards the OVA epitope was established. Infections with *Listeria* strains expressing a slightly altered amino acid sequence ('APL') of the OVA epitope induced sizable $CD8^+$ T-cell populations with partial cross-reactivity towards OVA. k_{off}-rate assay reagents were produced for each APL to reveal comparable inherent structural avidity in all populations towards their cognate epitope. Towards the OVA epitope, however, the APL-induced populations displayed robustly tiered global k_{off}-rates depending on the inducing APL. This tiering was closely mirrored in their peptide sensitivity (termed 'functional avidity') towards OVA and resulted in a strong correlation between global k_{off}-rates and functional avidity. The populations proved comparable in phenotypic composition and functional avidity towards their cognate epitope, excluding an inherently lower antigen reactivity as a confounding factor. Similarly, tumor killing capacity of OVA-expressing tumors by the differentially induced T cells was strongly positively correlated to their global k_{off}-rates in vitro and followed the previously observed TCR avidity tiering in an in vivo setting.

Lastly, human YFV-specific T-cell clones were used to merge monoclonal k_{off}-rates into a global k_{off}-rate, thereby mirroring and translating the findings from murine T-cell populations to humans. Moreover, global k_{off}-rates of polyclonal populations mixed from these clones could be predicted with high fidelity from the dissociation parameters of the constituent clones which may enable the design of global k_{off}-rates of T-cell populations from T-cell libraries.

Collectively, these results establish the global TCR-ligand k_{off}-rate as a novel parameter of the average structural avidity of polyclonal $CD8^+$ T-cell populations. Its strong correlation with multiple functional parameters and fast applicability makes it a promising tool in clinical research. Conversely, the extensive characterization and herein demonstrated predictability of the global k_{off}-rate from constituent T-cell clones paves the way to avidity-tailoring of composite T-cell therapeutics.

2. Introduction

2.1 T-cell immunity

The human immune system can be categorized into an innate and an adaptive arm. T cells and B cells are lymphocytes and essential elements of the adaptive immune system. Both cell types originate from hematopoietic stem cells in the bone marrow or fetal liver. While B-cell development continues in the bone marrow, T-cell progenitors emigrate to mature in the thymus. Utilizing similar proteins and mechanisms in a process called somatic gene rearrangement, B and T cells create a tremendous repertoire of antigen receptors capable of recognizing virtually every possible foreign antigen. B cell receptors recognize antigens directly while T-cell receptors (TCRs) recognize antigens as peptides presented on major histocompatibility complex class I (pMHC I) or class II molecules (pMHC II). Lymphocytes rearrange and slightly mutate a set of TCR genes or immunoglobulin genes, respectively, to develop an antigen receptor with a quasi-random binding site. Cells with dysfunctional receptors get deleted while the rest undergo positive and negative selection. For B cells, this starts in the bone marrow and continues in the periphery with somatic hypermutation under T-cell supervision with the aim of producing and secreting large quantities of highly specific antibodies that bind foreign -but not self- antigen. For most T-cell precursors, on the other hand, selection entails migration to the thymus where they express the co-receptors cluster of differentiation (CD) 4 and CD8 to interact with self-peptide bound to MHC on the surface of thymic cells. The binding strength of the TCR and co-receptors to these self-pMHCs plays a paramount role at this developmental stage: Cells whose TCRs bind either insufficiently, too strongly, or without the need of a co-receptor, die through apoptosis or become anergic (negative selection), whereas weakly binding cells are deemed potentially functional and self-tolerant (positive selection) (Ashton-Rickardt et al. 1994). Survivors predominantly go on to downregulate one of the co-receptors, retaining CD4 if they bind to pMHC II or CD8 if they bind to pMHC I, respectively (He et al. 2005). To become effector T cells, these naïve T cells first require activation. They emigrate from the thymus and circulate through secondary lymphoid tissues where they encounter antigen-presenting cells (APCs) stemming mainly from the innate immune system. Most prominently, dendritic cells sample antigens in the periphery and recognize them as foreign or as part of an inflammatory environment via conserved pattern-recognition receptors. This upregulates co-stimulatory molecules like B7 and prompts the migration to lymphoid tissues to present the antigens in a processed form on MHC I and MHC II molecules. Naïve antigen-specific T cells engage these pMHCs with their TCRs and co-receptors, become activated, stop circulating, and start to express co-stimulatory proteins like CD28. Only through both signals of TCR – pMHC interaction and interaction of co-stimulatory molecules like B7 and CD28 do the naïve T cells get fully activated and start to proliferate and differentiate into effector T cells (Chen und Flies 2013). Further signals from interleukins produced by APCs or other T cells guide differentiation and regulate proliferation. Activated T cells undergo massive expansion of several orders of magnitude and differentiate into distinct subsets. The major subset of ‘licensed’ effector T cells generally leave the lymphoid tissue and migrate to sites of inflammation where they carry out their effector function upon TCR ligation without requiring additional co-stimulation. In an acute infection setting with pathogen clearance, the peak of effector T-cell expansion is reached within 7-10 days, after which most of these T cells undergo apoptosis. A small subset of ‘memory’ T cells survives and sometimes persists for decades (Sprent und Tough 2001). These can rapidly respond to re-exposure of antigen and are a main prerequisite to pathogen-specific immunity. Memory T cells can be

further subdivided. Central memory T cells (T_{CM}), like naïve T cells, patrol secondary lymphoid organs and possess a high proliferative, but low immediate effector capacity, whereas effector memory T cells (T_{EM}) more heavily patrol or reside in nonlymphoid tissues and can confer swift protection upon antigen re-encounter (Sallusto et al. 1999).

The class of pMHC that T cells recognize and the co-receptor they express shape their roles in the immune response: $CD4^+$ T cells differentiate into several subsets which orchestrate, facilitate, or inhibit most known pathways of the immune response by producing cytokines and instructing MHC II-expressing cells. $CD8^+$ cytotoxic T cells secrete Interferon-γ (IFN-γ) which upregulates MHC I expression and they directly kill infected and cancerous cells that present recognized peptides on MHC I molecules by inducing apoptosis. This is mediated either via expression of tumor necrosis factor (TNF) family proteins like Fas-L that ligate apoptosis-inducing receptors like Fas on target cells or via secretion of cytotoxic granules containing granzymes and perforins which perforate target cell membranes and induce intrinsic apoptosis pathways once inside the cytosol (Russell und Ley 2002).

2.1.1 TCR and pMHC structure and interaction

T cells either bear a γ:δ TCR or an α:β TCR. γ:δ T cells primarily reside in the mucosa or other epithelia, do largely not express the CD4 or CD8αβ co-receptor, usually bind to non-peptide ligands, and are thus placed in between the innate and the adaptive immune system (Hayday 2000). This thesis was exclusively focused on α:β T cells, which constitute the vast majority of T cells in the blood and in lymphoid organs. Their TCR is composed of an α- and a β-chain which in turn consist of a variable region (V), a constant region (C), a stalk, a transmembrane domain, and a cytoplasmatic tail (**Figure 2-1**A). It is generated by somatic gene rearrangement of multiple 'V', 'J', and 'C' segments in the α- and β-chain locus, respectively, and four extra 'D' segments in the β-chain locus, as well as random addition of a few base pairs between all segments (Schatz und Swanson 2011). This leads to a vast diversity in the antigen binding site. For the TCR to be expressed at the cell surface, it has to be complexed with CD3δ, CD3γ, CD3ε, and CD3ζ chains to form the T-cell receptor complex. Beyond stabilization, the CD3 chains also initiate the intracellular activation signaling cascade upon TCR ligation via cytoplasmatic tails with motifs for phosphorylation (Call et al. 2002).

The MHC molecules are divided into MHC class I and MHC class II molecules. In humans, they are more specifically called human leukocyte antigens (HLAs), but the following statements apply to the MHCs of many vertebrates. MHC I molecules consist of a large α-chain that is anchored in the membrane and a smaller, non-covalently bound β_2-microglobulin. MHC II molecules consist of an α- and a β-chain -both anchored in the membrane- and resemble MHC I molecules in structure (**Figure 2-1**C). Both MHC classes have a peptide-binding groove in which they stably, but non-covalently, bind peptides, which in turn are required for stable MHC surface expression. Peptides are processed from proteins and loaded onto MHC molecules intracellularly (Grommé und Neefjes 2002). pMHC molecules (pMHC I in particular) thereby serve as a window into the cell that presents them and allows T cells to identify and kill cells with pathological protein production which is otherwise hidden behind cell membranes.

MHC proteins are highly polymorphic within and between individuals due to an abundance of MHC genes. Moreover, each MHC can bind a variety of peptides leading to a tremendous number of possible peptide:MHC combinations and an even larger amount of possible TCR – pMHC interactions.

The co-receptor CD4 consists of only one chain and binds to MHC II molecules, whereas CD8 binds to MHC I molecules and consists of the CD8α and the CD8β-chain as a heterodimer or rarely of two CD8α-chains as a homodimer (**Figure 2-1**B). Intracellularly, both co-receptors are associated with the kinase Lck, which promotes TCR phosphorylation and signaling upon co-localization (Davis und van der Merwe 2011).

Most TCRs bind pMHC diagonally with only their variable regions of both TCR chains being in contact with the peptide and the peptide-binding groove of the pMHC (**Figure 2-1**D). The recognition of both the MHC molecule and the peptide explains the phenomenon of MHC-restriction: T cells recognize virus epitopes presented by an infected cell only when the cell expresses a certain MHC genotype (Zinkernagel und Doherty 1974). TCR – pMHC interaction is therefore highly specific. The CD8 and CD4 co-receptors enhance this interaction by binding to peptide-distant sites on the pMHC molecule, which are preserved between the MHC classes (**Figure 2-1**D, Gáspár et al. 2001).

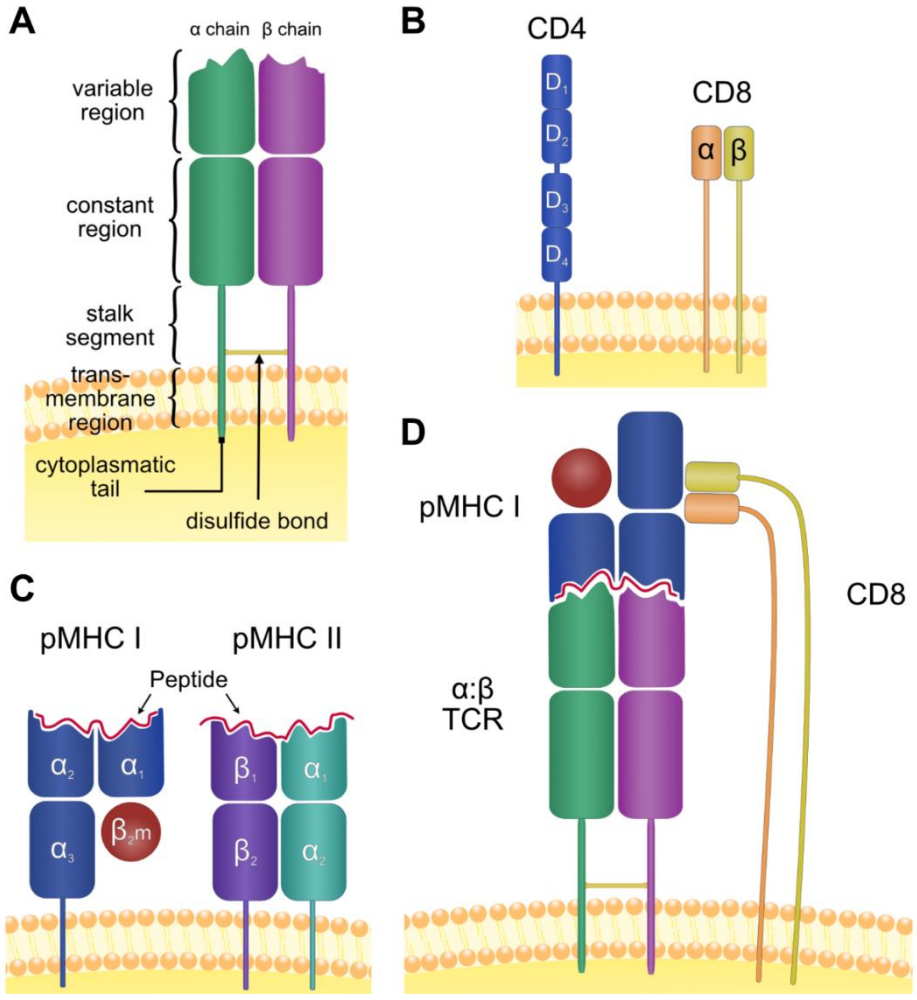

Figure 2-1. Structure and interaction of TCR, co-receptor, and pMHC molecules. **A**: Structure of the α:β TCR. The TCR is composed of an α- and a β-chain which in turn consist of a variable region (V), a constant region (C), a stalk, a transmembrane domain and a cytoplasmatic tail. The α:β chains are fused by a disulfide bond. They associate with CD3 subunits to form the TCR complex (not shown). **B**: CD4 and CD8 co-receptors. CD4 consists of only one chain with 4 subdomains. CD8 is a heterodimer consisting of the CD8α and the CD8β-chain. Rarely, CD8 forms as a homodimer of two CD8α-chains. CD4 and CD8 have transmembrane domains and a cytoplasmatic tail, and associate with Lck intracellularly, respectively (not shown). **C**: pMHC class I (left) and pMHC class II (right). Both MHC classes have a peptide-binding cleft (apical region) and are anchored in the membrane. MHC I consists of a polymorphic α-chain that binds to the peptide and pairs with the invariant β_2-microglobulin, whereas

MHC II consists of polymorphic α- and β-chains, which both contribute to the peptide-binding cleft. **D**: α:β TCR – pMHC I – CD8 interaction. α:β TCRs almost always engage the pMHC diagonally, scanning both the peptide and the apical part of the MHC. The co-receptor binds to an invariant region of the MHC located far from the peptide-binding cleft. α:β TCR – pMHC II – CD4 interactions display a similar mode of engagement.

2.1.2 TCR–pMHC binding strength

TCR–pMHC binding strength is called TCR affinity and can be quantified with dissociation constant K_D which describes the concentration of pMHC at which half of the TCR are bound and half are unbound to pMHC. K_D is mathematically defined as the ratio of the rate and concentration at which the TCR and the pMHC associate (k_{on}-rate) and the rate at which they dissociate (k_{off}-rate). The k_{off}-rate divided by $ln(2)$ yields the half-life ($t_{1/2}$) of the TCR–pMHC interaction. All of these parameters greatly depend on temperature and solution pH. When factors like co-receptor interaction and TCR clustering are considered in addition to TCR affinity, the cumulative binding strength is termed TCR structural avidity. It can be described with k_{on}-rate and k_{off}-rate as well, which can vary widely from that of the sole TCR–pMHC interaction. TCR affinity and TCR structural avidity are often ill-defined and used interchangeably in the literature. Herein, TCR affinity is used where solely a TCR and a pMHC interact, whereas TCR structural avidity is used where additional interactions exist.

Impact of TCR affinity and structural avidity on T-cell behavior

The importance of TCR structural avidity in T-cell activation and development in the thymus is well recognized and was described above. Its importance in mature T-cell behavior, however, is more obscure. Over the course of the immune response, a multitude of naïve T cells that happen to express a TCR specific for the same antigen get activated and proliferate, leading to a diverse antigen-specific T-cell population consisting of multiple T-cell clones (‘polyclonal’) with varying TCR structural avidity. The extent to which T cells expand upon antigen stimulation and the timing of their subsequent migration to the periphery was shown to strongly depend on the strength of TCR ligation. T cells responding to ligands with a low activation potential seem to undergo a curtailed expansion and a faster egress from lymphoid organs, presumably so that these T cells can provide a sub-optimal but fast adaptive immune response (Zehn et al. 2009). To this end, low-avidity T cells can even dominate the early T-cell response (Martinez et al. 2016). These T cells still significantly contribute to the memory T cell pool, albeit at a lower rate than T cells with a higher TCR avidity (Zehn et al. 2009). As a result, polyclonal T-cell populations undergo an ‘avidity maturation’ in subsequent immune responses as T cells with higher TCR structural avidity also get recruited more readily (Busch und Pamer 1999; Savage et al. 1999). In analogy to B-cell receptor affinity maturation, TCR avidity maturation forms the basis of an improved TCR repertoire in recurrent infections but does so without additional somatic mutation. There is evidence, however, that the TCR repertoire does not always evolve towards higher TCR avidity. In chronic CMV infections, the immunogenic antigens persist over years and decades, leading to an inflation of CMV-specific T cells. After an initial increase in TCR avidity shortly after primary infection, TCR avidity plateaus and then declines over time in conjunction with a change in TCR repertoire (Schober et al. 2020b). This ‘reverse repertoire evolution’ presumably occurs due to senescence of high-avidity T cells and compensatory expansion of low-avidity T cells.

These findings point to a preference of the immune response towards higher avidity T cells at least in acute infections, which implies that they confer superior effector functions. To test this hypothesis more rigorously, several TCR affinity and avidity assays have been developed and

their results correlated with functional parameters. Some of these assays were also used to acquire the results described above but will now be described in detail.

TCR affinity and avidity assays

An assay that is often considered to be the 'gold standard' of TCR-pMHC affinity measurement utilizes surface plasmon resonance (SPR). SPR exploits a phenomenon that occurs when polarized light traveling through a prism hits a thin metal layer: At a specific angle, the light excites the electrons in the metal layer causing so called surface plasmon polaritons. This leads to changes in the intensity of the reflected light, which is recorded with a light sensor. The surface plasmons are highly sensitive to changes in mass at the surface so that binding of even small molecules to the surface cause a shift in the angle at which they form. This in turn leads to a change of the reflected light in real-time which is detected by the sensors (Nguyen et al. 2015). This can be utilized for TCR-pMHC binding assays by immobilizing one of the two binding partners on the surface layer and flushing a solution containing the other over it. The proteins bind to each other according to their k_{on}-rate and eventually reach a binding equilibrium, after which a buffer solution can flush out the protein so that the dissociation rate can be observed (**Figure 2-2**A, (Corr et al. 1994)). TCR affinity measurements with SPR revealed K_D ranging from ~1µM to ~100µM with dissociation half-lives typically <100s (Bridgeman et al. 2012). While this assay provides both a k_{on}-rate as well as a k_{off}-rate with intriguing precision, the low throughput by virtue of the high effort of recombinant production of both pMHC and TCR has hampered widespread adoption. More importantly, several works have reported conflicting results regarding the relationship between the SPR acquired TCR affinity values and TCR functionality, which might be explained by the lack of cell-cell interactions and co-receptors in this assay (Stone et al. 2009; Adams et al. 2011).

In contrast, TCR structural avidity measurements take place on the cell surface of T-cells and are therefore a more physiological approach. However, they have been challenging to standardize due to the added complexity and due to the diversity of assays.

Micropipette adhesion assays with and without biomembrane force probes utilize a red blood cell as adhesion and force sensor with or without a glass bead mounted to its apex. They are coated in streptavidin and biotinylated pMHC immobilized to their surface (**Figure 2-2**B). By bringing a T cell that is also held by a micropipette close to a defined area of the pMHC coated surface and by retracting it again, the adhesion frequency and bond lifetime can be inferred visually and/or via force measurements by the stretch of the red blood cell membrane. For TCR - pMHC k_{off}- and k_{on}-rate calculations, TCR density on the probed T cell and pMHC density on the red blood cell/glass bead must be determined, *e.g.*, through flow cytometry (**Figure 2-2**B). These TCR avidity measurements have shown striking correlations with T-cell effector functions (Huang et al. 2010; Liu et al. 2014). However, this assay also has a very low throughput as it requires manual single cell measurements as well as production and fixation of recombinant pMHC molecules.

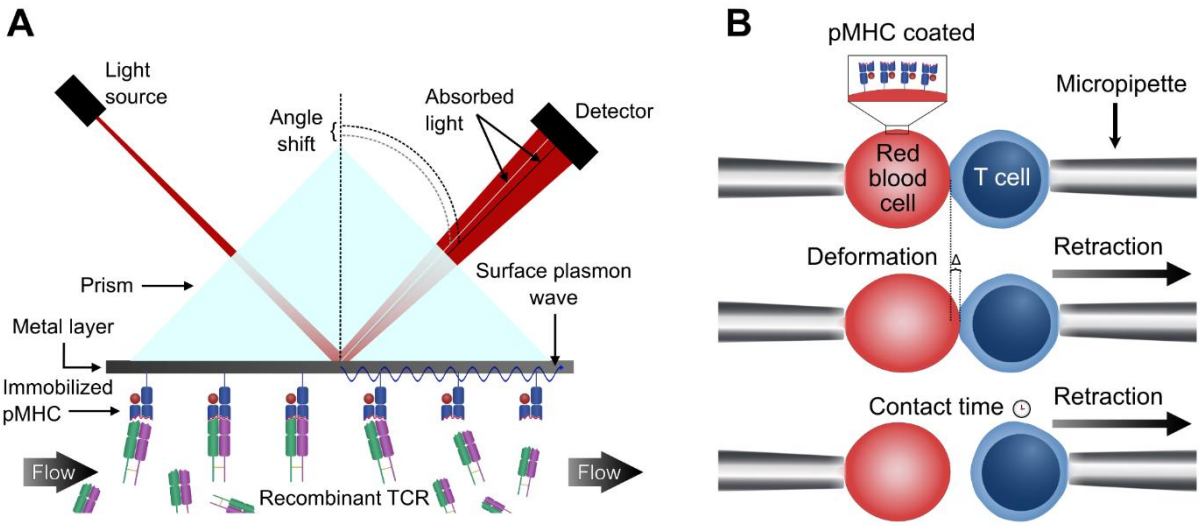

Figure 2-2. Surface plasmon resonance and micropipette adhesion TCR – pMHC assays. A: Surface plasmon resonance-based assay. pMHC molecules are immobilized on a thin metal layer at which a laser is directed. The light travels through a prism and is reflected. At a specific angle, the light excites a surface plasmon polariton which causes a decrease in the intensity of reflected light at this angle. Recombinantly expressed TCR is then flushed along the pMHC at a given concentration. When TCR-pMHC binding occurs, it slightly changes the refractive index of the prism/metal construct and therefore the angle at which the polariton forms. This leads to a difference in light intensity in real-time, allowing for a measurement of the TCR-pMHC k_{on}-rate. By flushing a buffer along the surface, the dissociation of the TCR-pMHC pairs is initiated and the k_{off}-rate measured via the change in the reflected light. **B:** Micropipette adhesion assay. A red blood cell is held in place by a micropipette and is used as an adhesion and force sensor. It is then functionalized by attaching a pMHC coated glass bead to its apex (=biomembrane force probe, not shown) or by covering itself with a streptavidin coating and biotinylated pMHC. A T cell is held by another micropipette and brought in contact with the red blood cell or glass bead multiple times. Adhesion is observed visually upon retraction of the T cell by deformation of the red blood cell membrane, or by deflection of the glass bead, respectively. Adhesion frequency, contact time, and force can be measured and the TCR - pMHC k_{off}- and k_{on}-rate inferred from these parameters and the TCR and pMHC density.

As evidenced by the abovementioned assay, both k_{on}-rate and k_{off}-rate of the TCR-pMHC interaction are implicated to majorly influence T-cell behavior, but current TCR signaling models place an emphasize on the k_{off}-rate (Lever et al. 2014). Although not completely understood, the proposed kinetic proofreading with limited signaling model best fits experimental data. It suggests that a lower k_{off}-rate, *i.e.*, a longer dissociation time, leads to more potent activation, but only up to a supposed optimum, after which a longer binding leads to inhibitory signals (Lever et al. 2014). The importance of the k_{off}-rates motivated the development of TCR-ligand assays that exclusively measure k_{off}-rates, which are highlighted below.

These assays employ multimers consisting of multiple recombinant pMHC molecules non-covalently bound to a backbone molecule (**Figure 2-3**A). After staining a T cell with them, multimers consisting of 4 or more pMHCs typically display dissociation $t_{1/2}$ of several hours instead of seconds as for monomers, because every TCR-pMHC bond needs to be broken for multimers to dissociate ('avidity gain'). Moreover, re-binding of TCR-pMHC pairs frequently occur, further prolonging multimer binding time. This has been exploited to stably label antigen-specific T cells with multimers for a plethora of experiments since its conception (Altman et al. 1996). Moreover, dissociation time of pMHC multimers has been used as a popular parameter to measure TCR structural avidity because of its ex vivo applicability. However, due to the very long dissociation $t_{1/2}$, blocking agents are usually required to inhibit re-binding of pMHC

molecules and allow for timely dissociation of the multimers to occur. Using this approach, many groups have found correlations of T-cell functionality and $t_{1/2}$ (Yee et al. 1999; Schmid et al. 2010). However, due to the multivalent nature of pMHC multimers, great variance in the blocking agents, multimer reagents, and experiment parameters employed in these works, multimer dissociation experiments allow limited insight into TCR structural avidity (Wang und Altman 2003).

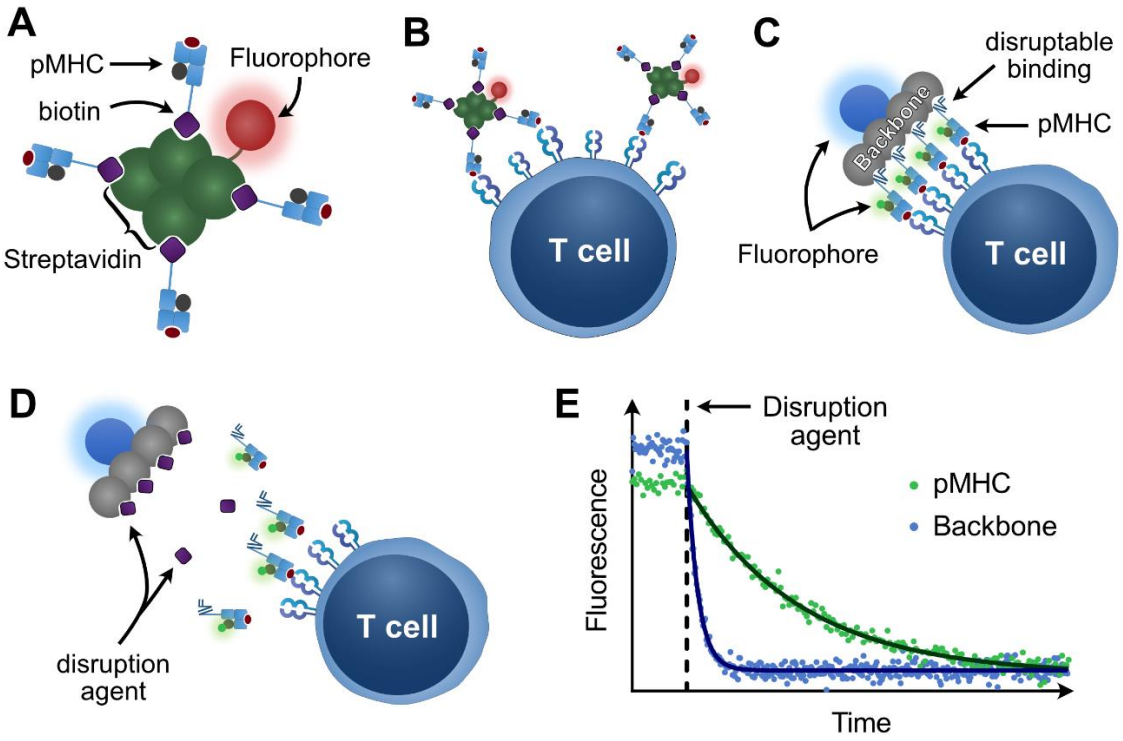

Figure 2-3. pMHC multimers and reversible multimer TCR – pMHC dissociation assays. A: Schematic structure of a fluorescently labeled pMHC multimer. Streptavidin is a homo-tetramer with extraordinarily high affinity for biotin. This is exploited to stably multimerize up to 4 biotinylated pMHC molecules. **B**: Antigen-specific T cells can be stably labeled for hours with the multimers described in (A), because all TCR – pMHC bonds need to be broken for the multimer to dissociate. **C**: Reversible multimer staining. Fluorescently labeled pMHCs are multimerized by a fluorescently labeled backbone and can stably label antigen-specific T cells. The moieties on the tail end of the pMHC molecules have a high affinity for the backbone but can be rapidly displaced by a disruption agent with much higher affinity for the backbone. **D**: When a disruption agent is added to the staining described in (C), it displaces the pMHC molecules and the backbone dissociates, effectively reversing the multimerization. The now monomeric TCR - pMHC bindings are unstable and dissociate according to the k_{off}-rate of the interaction. **E**: Dissociation of the backbone and the pMHC molecules described in (D) can be tracked by the fluorescence decay over time. To calculate the k_{off}-rates, exponential decay curves can be fitted to the measured fluorescence after addition of the disruption agent. All panels omit co-receptors for simplicity. However, co-receptors can significantly contribute to the interaction with pMHC molecules.

To remedy these shortcomings, TCR-ligand k_{off}-rate assays utilizing reversible pMHC-multimer stainings have been developed. Reversible pMHC-multimers display properties similar to conventional pMHC-multimers but additionally yield an exceptionally high affinity to a disruption agent at the pMHC binding sites of the backbone. When these agents are added to the sample, they quickly disrupt pMHC-backbone binding, leaving pMHCs monomerically bound to the TCR of the antigen-specific T cells. The TCR-pMHC pairs dissociate over time according to the k_{off}-rate of their interaction. If the pMHC molecules are labeled with a fluorophore, this dissociation can be observed over time and the $t_{1/2}$ of the dissociation can be measured by the fluorescence decay (**Figure 2-3**C, D, E).

To this end, besides the so-called MHC-Streptamer technology (see below), reversible multimers called 'NTAmers' consisting of chelate complexes of fluorescently labeled recombinant pMHC with an oligo-histidine tag (His-tag) and a backbone with Ni^{2+}-nitrilotriacetic acid (NTA) moieties were developed for a TCR-ligand k_{off}-rate assay. The His-tag binds strongly to NTA, but can be displaced by the disruption agent imidazole, which can disrupt multimers within minutes (Schmidt et al. 2011). The assay was used to measure the TCR avidity of a large number of T-cell clones and cell lines (Schmidt et al. 2011; Hebeisen et al. 2015; Allard et al. 2017). The TCR-ligand k_{off}-rate was shown to correlate well with a multitude of functional measures in vitro and in vivo while displaying a remarkable stability over several days in contrast to other popular proxies for TCR functionality like cytotoxicity (Allard et al. 2017). This relative independence of the functional activity of the T cell at any given time emphasizes the prognostic value of TCR structural avidity measurements.

Streptamer-based TCR-ligand k_{off}-rate assay

The TCR-ligand k_{off}-rate assay developed by our group utilizes reversible multimers called 'streptamers' consisting of fluorescently labeled recombinant pMHC with a Strep-tagIII, which has a high affinity to the binding sites of a Strep-Tactin backbone. D-biotin, however, has a much higher affinity to these binding sites and rapidly displaces the pMHCs upon addition to the sample, disrupting the streptamers within seconds (**Figure 2-3**C, D) (Knall 2007). TCR-ligand k_{off}-rates of individual T cells can be measured by observing the fluorescence decay of the labeled pMHC from the cell surface over time under a microscope. The obtained k_{off}-rates were maintained even after recombinant re-expression of the inspected TCRs and were predictive of peptide sensitivity and in vivo protectivity of antigen-specific T-cell lines (Nauerth et al. 2013). The development also enabled quantification of an average TCR avidity within polyclonal populations as well as observation of their avidity distribution. This allows for a more representative analysis of the naturally polyclonal T-cell response as compared to the analysis of monoclonal populations which most of the abovementioned TCR-ligand assays are restricted to. The microscopic version of this assay, however, was still limited in scale and speed of analysis as it required sorting of antigen-specific T cells from heterogenous cell samples to enrich the analytic sample enough to enable analysis.

To overcome these limitations, a flow cytometric version of the streptamer-based TCR-ligand k_{off}-rate assay was developed. In this version, monoclonal antigen-specific T cells are stained with a streptamer and analyzed with a flow cytometer. After a few seconds of acquisition, D-biotin is injected into the sample tube which facilitates the rapid disruption of the streptamers with a prompt dissociation of the Strep-Tactin backbones. The dissociation of the monomeric pMHC-TCR pairs the occurs according to their k_{off}-rate (**Figure 2-3**C, D). Slight differences in the k_{off}-rate and (auto-)fluorescence between the monoclonal cells within the sample are averaged out and the mean k_{off}-rate quantified by fitting an exponential-decay curve to the pMHC fluorescence decay (**Figure 2-3**E).

To obviate the need for prior cell sorting and to enable ex vivo measurements, a double multimer staining was developed that stably labels antigen-specific T cells in heterogenous cell samples. In addition to the reversible streptamer, a conventional irreversible multimer with the same pMHC specificity was added to the staining. By gating on the constant fluorescent signal of the irreversible multimer during the dissociation, the antigen-specific T cells could be reliably tracked, and their k_{off}-rates quantified. The thereby measured values were comparable to those acquired without double multimer staining and those from the microscopic version of the assay (Nauerth et al. 2016).

The improved speed and ex vivo applicability of this flow cytometric version came at the price of losing the ability to measure single cell k_{off}-rates as the flow cytometer can only capture a snapshot of each cell. In fact, none of the abovementioned assays is able to provide rapid ex vivo single cell k_{off}-rate measurements, which constricts most analyses to monoclonal populations or small-scale sample surveys of polyclonal populations.

As will be discussed in the next section, most clinical T-cell products are polyclonal. To harness the prognostic power of TCR structural avidity for these populations, it would be therefore highly desirable to develop an assay that can comprehensively measure TCR avidity of polyclonal populations. It was the aim of this thesis to adapt the flow cytometric streptamer-based TCR-ligand k_{off}-rate assay for it to provide a measure of TCR avidity of polyclonal populations and to correlate this measure with functional parameters.

2.2 Clinical applications of T cells

T cells can exert powerful effector functions on virtually all human tissues and have therefore been the focus of development of therapeutics for many diseases. As elucidated above, the T-cell receptor is of crucial importance to T-cell functionality and the TCR avidity pivotal for the strength and duration of the response. The following paragraphs will introduce therapeutic approaches that involve T-cell populations and will highlight the role of polyclonality and TCR avidity.

2.2.1 Adoptive T-cell therapy

A most direct treatment with T cells is the transfer of them into a patient. This procedure is called adoptive T-cell transfer and can involve a patient's own ('autologous') T cells, or the T cells of a donor ('allogeneic'). It is most often applied in cancer therapy or for the treatment of viral infections in immunocompromised individuals and can include selection and/or manipulation steps in vitro to increase the specificity and efficacy of the T-cell product.

A crucial concept in adoptive T-cell therapy is the phenomenon of alloreactivity: A share of the physiological T-cell repertoire can recognize foreign HLA molecules without prior exposure, in part due to an intrinsic affinity of TCRs towards HLA (Felix und Allen 2007). Alloreactivity leads to the rejection of T-cell products from allogeneic sources by the host's T cells and, conversely, to an immune response of the T-cell product against the host's cells. Many T-cell products are designed to circumvent alloreactivity via use of autologous T cells, or to mitigate it by selecting T-cell donors with matching HLAs. Others exploit it to achieve an anti-cancer effect while accepting the risk of collateral damage to healthy tissue.

Allogeneic hematopoietic stem cell transplantation and donor lymphocyte infusions

The first clinically effective adoptive T-cell therapies were achieved through allogeneic hematopoietic stem cell transplantations (allo-HCT) in hematological malignancies. Strong conditioning chemotherapies that deplete endogenous T cells are required to prohibit the rejection of the allogeneic stem cells. However, this also allows allogeneic T cells present in the transplant to engraft. At first, these T-cells were seen as a contaminant, as they can cause severe morbidity through alloreactivity by attacking healthy tissue of the host; a syndrome called 'graft vs. host disease' (GvHD), which makes the prophylactic application of powerful immunosuppressive drugs a prerequisite of allo-HCT. However, it quickly became clear that these donor T cells confer most of the effectivity of the graft on the malignancy ('graft vs. tumor effect') (Weiden et al. 1979). Similarly, the apheresis and administration of additional doses of

donor T cells as donor lymphocyte infusions (DLIs) can induce further remissions after relapse post-allo-HCT (Kolb et al. 1990). Because these donor T cells are not selected for any specific antigen and the antigens they recognize in any given host are largely unknown, the role of TCR avidity in their effectivity is unclear. However, they do appear to retain polyclonality and mount malignancy-directed immune responses (Hofmann et al. 2019).

Virus-specific T cells

Virus-specific T-cell therapy represents a selectively antigen-directed approach. The T cells are typically derived from a partially or fully HLA-matched donor, pre-sorted via pMHC multimer staining or cytokine capture, and ex vivo expanded with virus-related peptide pools (Keller und Bollard 2020; Neuenhahn et al. 2017). The T-cell product is then transferred into immunocompromised patients with uncontrolled virus infections, *e.g.*, patients who have recently undergone allo-HCT. This targeted approach has yielded high response rates in clinical trials while occurrence of GvHD was relatively rare, presumably because of the high specificity of the selected T cells (Keller und Bollard 2020; Schmitt et al. 2011). In preclinical models, a higher TCR avidity towards viral epitopes was associated with superior viral clearance (Derby et al. 2001), but rigorous studies of TCR avidity of virus-specific T-cell therapeutics and its association with anti-viral properties in humans are lacking.

Cancer-targeting T cells

As was demonstrated in allo-HCT, T-cell transfer has the potential to induce remissions in cancer patients. Many solid cancers are infiltrated by tumor-infiltrating lymphocytes (TILs), some of which recognize tumor-associated self-antigens or neoantigens expressed exclusively by the tumor (Schumacher und Schreiber 2015). Expansion and re-infusion of these TILs has shown promising efficacy for some tumor entities (Rosenberg et al. 1988; Rosenberg et al. 2011). TIL populations are polyclonal and typically target many tumor antigens, but they also harbor a large proportion of T cells with low avidity or with no detectable reactivity towards the tumor at all (Oliveira et al. 2021).

To overcome these hurdles, T-cell therapeutics with genetically engineered antigen receptors were developed. T cells harvested from the patient's blood can be transduced to express an antigen receptor, expanded in vitro, and then re-infused in great number to exert effector functions against cancer cells expressing the target antigen. Synthetic chimeric antigen receptors (CARs) consist of antibody fragments fused to TCR and co-receptor signaling domains. CAR-T-cell therapeutics have shown astonishing clinical efficacy and have revolutionized the treatment of B-cell malignancies (Maude et al. 2018; Neelapu et al. 2017). CARs circumvent HLA-restriction by directly binding to cell surface molecules, but unlike TCRs, virtually no CAR can target intracellular proteins. TCR-engineered T-cell therapy aims to remedy this, and many early clinical trials are currently ongoing (Zhang et al. 2022). TCR binding strength is pivotal in preclinical TCR selection as high-affinity TCRs show superior antitumor responses and can even enable $CD4^+$ T cells to recognize and kill tumor cells (Zhong et al. 2013; Zhao et al. 2007). While antigen receptor engineered T cells show great promise, their monoclonal nature makes them prone to antigen escape of the cancer cells, which is a common mechanism of resistance (Majzner und Mackall 2018). Equipping T cells with multiple recombinant antigen receptors might ameliorate this issue.

2.2.2 Immune checkpoint inhibitors

Immune checkpoint molecules physiologically inhibit T cell activation and effector functions to regulate the immune response and minimize collateral damage. However, many types of

cancer exploit these pathways to curb the immune response against them and to proliferate unchecked. By blocking immune checkpoint molecules, T cells can mediate deep and lasting remissions. The most prominent and very potent axes are mediated by PD1, PDL1, and CTLA4, all of which have been successfully targeted by immune checkpoint inhibitor therapy.

PD1/PDL1 blockade

PD1 is upregulated by activated T cells and binds to PDL1, which is expressed by APCs as well as peripheral tissues in inflammatory contexts (Fife und Bluestone 2008). Upon ligation, PD1 can facilitate exhaustion or apoptosis of T cells. This is commonly exploited by cancer cells to repress T-cell responses. Monoclonal antibodies blocking PD1 or PDL1 have shown remarkable success in clinical trials of a wide variety of malignancies (Robert et al. 2015). Blockade of the PD1/PDL1 axis leads to an influx of new T-cell clonotypes into the tumor resulting in a polyclonal cancer-specific T-cell response (Nagasaki et al. 2022). The role of TCR avidity in this response is largely unknown, but monoclonal murine models suggest that both high- and low-avidity T cells contribute to the ensuing anti-tumor response (Martínez-Usatorre et al. 2018; Shimizu et al. 2021).

CTLA4 blockade

CTLA4 is upregulated by activated T cells, constitutively expressed by regulatory T cells, and binds to B7 expressed on APCs more avidly than CD28. CTLA4 ligation leads to inhibition of activated T cells and to sequestration of B7 which deprives naïve T cells of activation (Fife und Bluestone 2008). Inhibition of CTLA4 via antibodies has led to survival benefits for patients with melanoma; a tumor entity that generally carries a high mutational burden (Schadendorf et al. 2015). The response is largely driven by emerging polyclonal T-cell responses against neoantigens expressed by the tumor (Snyder et al. 2014). TCR avidity of these responding T-cell populations remains unexplored.

2.2.3 Therapeutic cancer vaccination

Therapeutic cancer vaccination elicits immune responses against select epitopes, just like prophylactic vaccination against infectious diseases. Unlike prophylactic vaccines, however, therapeutic cancer vaccination aims to cause the elimination of malignant cells which mostly express self-antigens and few novel antigens (‘neoantigens’) produced by expression of aberrant proteins. Overcoming self-tolerance, vaccinations with tumor-associated self-antigens can induce polyclonal T-cell populations with high TCR avidity (Carretero-Iglesia et al. 2019). However, several large clinical trials testing therapeutic cancer vaccination have reported negative outcomes (Saxena et al. 2021). Possible reasons for this failure include immune escape, immune suppression, and low durability and numbers of T cells.

Subsequently, vaccinations against cancer-specific neoantigens have become the most popular approaches as they have the potential to yield high efficacy as well as minimal toxicity (Waldman et al. 2020). T-cell recognition is at the core of the immune response against cancer-neoantigen (Matsushita et al. 2012). Therefore, the focus of therapeutic cancer vaccination design has been on the identification of cancer-specific pMHC epitopes from patient material (Waldman et al. 2020). This approach has shown promising results in small clinical trials and has been shown to induce antigen-specific polyclonal T-cell populations (Sahin et al. 2017; Carreno et al. 2015). Despite a high interest in TCR functional avidity of these populations (Hu et al. 2021), the TCR structural avidity of neoantigen-vaccination-induced T-cell populations remains unstudied. Elucidating the effect of different approaches on TCR structural avidity could inform future vaccine designs and their clinical potential. Although there is currently no approved therapeutic cancer vaccine, several ongoing clinical trials with a diverse range of

cancer entities and delivery approaches give hope that patients will soon benefit from this immunotherapy.

In summary, the clinical application of T cells is a rapidly growing field of research and has produced remarkable therapeutics that have revolutionized cancer and infection therapy. However, the high failure rate of past clinical trials in the field emphasizes the need for more rigorous preclinical evaluation and improved assays that can meaningfully assess critical properties. Moreover, the oftentimes high economic costs of T-cell therapies mean that prognostic markers for therapeutic efficacy become increasingly important. TCR avidity is a widely accepted marker for T-cell functionality, but also challenging to assess quickly and robustly especially in polyclonal populations. The development and validation of an assay with such capabilities could inform the design of T-cell therapeutics and might help predict their clinical efficacy.

3. Aims of this Thesis

T cells are a central pillar of the adaptive immune system and powerful actors in immune responses to infections or malignancies. T cells exert effector functions upon recognition of target-epitopes with their T-cell receptors. Beyond mere recognition, the strength of this interaction is predictive of the scope of T-cell functionality. Structural TCR avidity is therefore an appealing prognostic marker for T-cell therapeutics and has been subject of intense study. Many assays measuring various aspects of structural TCR avidity have been developed and their measurements correlated with functional parameters. A particularly fast and comprehensive assay is the recently developed flow cytometric streptamer-based TCR-ligand k_{off}-rate assay for $CD8^+$ T cells. Notwithstanding, like virtually all assays, it had only been capable of measuring the structural TCR avidity of monoclonal T-cell populations. However, since physiological T-cell responses and most T-cell therapeutics are polyclonal, there is a great need for assays capable of assessing the structural TCR avidity of polyclonal T-cell populations.

It was the aim of this thesis to adapt the flow cytometric streptamer-based TCR-ligand k_{off}-rate assay to assess polyclonal $CD8^+$ T-cell populations to yield a measure of 'global' TCR avidity and to correlate this measure with functional parameters. Moreover, it aimed to explore the impact of the TCR avidity of subclonal T-cell populations on the global TCR avidity of polyclonal populations.

To this end, the methodology for measuring TCR avidity of murine polyclonal $CD8^+$ T-cell populations needed to be established. Analogous to TCR avidity measurements of monoclonal populations, the aim was to use the flow-cytometric streptamer k_{off}-rate assay to develop and validate a single dissociation constant for polyclonal populations that integrates the multiple TCR-ligand interactions of different avidities and captures the 'global' avidity of the population. In a next step, T-cell populations with varying ranges of avidities towards a model epitope needed to be generated to isolate and examine the effects of global TCR avidity on functionality while controlling for confounding factors like phenotypic composition. These populations would then be tested for their functional TCR avidity and tumor killing capacity and the results correlated with their TCR avidity measurements. A final goal was to translate the methodology to human polyclonal T-cell populations to enable clinical applications of the developed technology.

4. Materials and Methods

4.1 Materials

4.1.1 Antibodies

All the following antibodies are directed against murine antigens and titrated for optimal staining intensity.

Antigen	Fluorophore	Clone	Supplier
APC	/	APC003	Biolegend, San Diego, USA
APC	/ (microbeads)	N/A	Miltenyi Biotec, Bergisch Gladbach, Germany
CD8α	PO	5H10	Life Technologies, Darmstadt, Germany
CD8α	PB	5H10	Life Technologies, Darmstadt, Germany
CD8α	APC	5H10	Life Technologies, Darmstadt, Germany
CD8α	PE-Cy7	5H10	Life Technologies, Darmstadt, Germany
CD8α	FITC	53-6.7	Biolegend, San Diego, USA
CD16/32 (Fc-block)	/	2.4G2	BD Biosciences, Heidelberg, Germany
CD19	PE-CF594	6D5	Biolegend, San Diego, USA
CD27	PE	LG.7F9	Life Technologies, Darmstadt, Germany
CD27	PE-Cy7	LG.7F9	Life Technologies, Darmstadt, Germany
CD44	APC	IM7	Biolegend, San Diego, USA
CD44	FITC	IM7	Biolegend, San Diego, USA
CD45.2	APC-eFluor 780	104	Life Technologies, Darmstadt, Germany
CD45.2	PerCP-Cy5.5	104	Biolegend, San Diego, USA
CD62L	APC	MEL-14	Biolegend, San Diego, USA
CD62L	APC-Cy7	MEL-14	Biolegend, San Diego, USA
CD90.2	APC-eFluor 780	53-2.1	Life Technologies, Darmstadt, Germany
IFN-γ	APC	XMG1.2	Life Technologies, Darmstadt, Germany
PE	/ (microbeads)	N/A	Miltenyi Biotec, Bergisch Gladbach, Germany
Vβ TCR 2	FITC	B20.6	BD Biosciences, Heidelberg, Germany
Vβ TCR 3	FITC	KJ25	BD Biosciences, Heidelberg, Germany
Vβ TCR 4	FITC	KT4	BD Biosciences, Heidelberg, Germany
Vβ TCR 5.1 & 5.2	FITC	MR9-4	BD Biosciences, Heidelberg, Germany
Vβ TCR 6	FITC	RR4-7	BD Biosciences, Heidelberg, Germany
Vβ TCR 7	FITC	TR310	BD Biosciences, Heidelberg, Germany
Vβ TCR 8.1 & 8.2	FITC	MR5-2	BD Biosciences, Heidelberg, Germany
Vβ TCR 8.3	FITC	1B3.3	BD Biosciences, Heidelberg, Germany
Vβ TCR 9	FITC	MR10-2	BD Biosciences, Heidelberg, Germany
Vβ TCR 10^{b}	FITC	B21 .5	BD Biosciences, Heidelberg, Germany
Vβ TCR 11	FITC	RR3-15	BD Biosciences, Heidelberg, Germany

Vβ TCR 12	FITC	MR11-1	BD Biosciences, Heidelberg, Germany
Vβ TCR 13	FITC	MR12-3	BD Biosciences, Heidelberg, Germany
Vβ TCR 14	FITC	14-2	BD Biosciences, Heidelberg, Germany
Vβ TCR 17[a]	FITC	KJ23	BD Biosciences, Heidelberg, Germany

All the following antibodies are directed against human antigens and titrated for optimal staining intensity. They were used by Patrick Huppertz and Manuel Effenberger in experiments on human cells. The list was adapted from (Peter Patrick Huppertz 2016).

Antigen	**Fluorophore**	**Clone**	**Supplier**
CD3	BV650	UCHT1	eBioscience, San Diego, USA
CCR7	FITC	FAB197F	R&D Systems
CD8α	PE	3B5	Caltag/Invitrogen, Carlsbad, USA
CD19	ECD	J3-119	Beckman Coulter, Fullerton, USA
CD3 stimulating ab	/	OKT3	Beckman Coulter, Fullerton, USA
CD28 stimulating ab	/	L293	Beckman Coulter, Fullerton, USA
CD45	ECD	J.33	Beckman Coulter, Fullerton, USA
CD45	PE-Cy7	2D1	eBioscience, San Diego, USA
CD45	PB	T29/33	Dako, Carpinteria, USA
CD45	PO	HI30	EXBIO, Vestec, Czech Republic

4.1.2 Buffers and Media

Buffer / Medium	**Composition**	
Ammonium Chloride Tris	0.17M 0.3M	NH4Cl Tris-HCl, pH 7.5
D-biotin stock solution (10M)	100ml 244.31g Adjusted to pH 7	H_2O, pH 11 D-Biotin
DMEM+ cell culture medium	1x 10% (w/v) 0.001% (w/v) 0.1% (w/v) 0.025% (w/v) 0.002% (w/v) 0.002% (w/v)	DMEM FCS Gentamycin HEPES L-Glutamine Penicillin Streptomycin
FCM buffer	1x 0.5% (w/v) Adjusted to pH 7.45	PBS BSA
FPLC buffer	1L 50mM 20mM	H_2O, pH 8.0 NaCl Tris-HCl
Guanidine solution	100ml 3M 10mM 10mM	H_2O, pH 4.2 Guanidine-HCl NaAcetate NaEDTA
Refolding buffer	1L 0.5mM	H_2O, pH 8.0 Glutathione, oxidized

	5mM	Glutathione, reduced
	400mM	L-Arginin
	2mM	NaEDTA
	100mM	Tris-HCl
RP10+ cell culture medium	1x	RPMI 1640
	10% (w/v)	FCS
	0.001% (w/v)	Gentamycin
	0.1% (w/v)	HEPES
	0.025% (w/v)	L-Glutamine
	0.002% (w/v)	Penicillin
	0.002% (w/v)	Streptomycin

4.1.3 Chemicals and Reagents

Chemical / Reagent	Supplier
Alexa 488 maleimide	Fisher Scientific GmbH, Schwerte, Germany
Ammonium chloride	Sigma, Taufkirchen, Germany
β-Mercaptoethanol	Sigma, Taufkirchen, Germany
BC assay reagents	Interchim, Montluçon, France
Bovine serum albumin	Sigma, Taufkirchen, Germany
Cytofix/Cytoperm	BD Biosciences, Heidelberg, Germany
D-biotin	Sigma, Taufkirchen, Germany
Dimethyl Sulfoxide	Sigma, Taufkirchen, Germany
DMEM	GibcoBRL, Karlsruhe, Germany
Ethanol	Klinikum rechts der Isar, Munich, Germany
Ethidium Monoazide Bromide	Life Technologies, Carlsbad, USA
Fetal calf serum	Biochrom, Berlin, Germany
Gentamycin	GibcoBRL, Karlsruhe, Germany
Glutathione, oxidized	Sigma, Taufkirchen, Germany
Glutathione, reduced	Sigma, Taufkirchen, Germany
GolgiPlug	BD Biosciences, Heidelberg, Germany
Guanidine-HCl	Sigma, Taufkirchen, Germany
HEPES	GibcoBRL, Karlsruhe, Germany
Hydrochloric acid	Carl Roth, Karlsruhe, Germany
Ionomycin	Sigma, Taufkirchen, Germany
L-Glutamine	GibcoBRL, Karlsruhe, Germany
Leupeptin	Sigma, Taufkirchen, Germany
Pepstatin	Sigma, Taufkirchen, Germany
Peptides	peptides & elephants, Hennigsdorf, Germany
Perm Wash	BD Biosciences, Heidelberg, Germany
Phorbol-12-myristat-13-acetat	Sigma, Taufkirchen, Germany
Phosphate buffered saline	Biochrom, Berlin, Germany
Propidium iodide	Life Technologies, Carlsbad, USA

RPMI 1640	GibcoBRL, Karlsruhe, Germany
Strep-Tactin conjugates	IBA, Göttingen, Germany
Sodium chloride	Carl Roth, Karlsruhe, Germany
Sodium ethylenediaminetetraacetic acid	Sigma, Taufkirchen, Germany
Sodium hydroxide	Carl Roth, Karlsruhe, Germany
Tris hydrochloride	Carl Roth, Karlsruhe, Germany
Trypan blue solution	Sigma, Taufkirchen, Germany
Trypsin-EDTA (0.25%), phenol red	GibcoBRL, Karlsruhe, Germany

4.1.4 Equipment

Equipment	Model	Supplier
Biological Safety Cabinet	Herasafe	Heraeus, Hanau, Germany
Centrifuges	Multifuge 3 S-R	Heraeus, Hanau, Germany
	Varifuge 3.0RS	Heraeus, Hanau, Germany
	Sorvall RC 6 Plus	Thermo Scientific, Waltham, USA
k_{off}-rate Cooling Device		Qutools, Munich, Germany
Flow Cytometers	CyAn ADP	Beckman Coulter, Fullerton, USA
	CytoFLEX S	Beckman Coulter, Fullerton, USA
	MoFlo Legacy Cell Sorter	Beckman Coulter, Fullerton, USA
FPLC	ÄKTA Purifier 10	GE Healthcare, Solingen, Germany
Incubation Shaker	Minitron	Infors, Bottmingen, Germany
Neubauer Chamber	Neubauer Improved	Schubert, München, Germany
Photometer	BioPhotometer	Eppendorf, Hamburg, Germany
pH Meter	MultiCal pH 526	WTW, Weilheim, Germany
Precision Balance	CP124S	Sartorius, Göttingen, Germany
RTCA Analyzer	xCELLigence RTCA MP	OMNI Life Science, Bremen, Germany

4.1.5 pMHC molecules

Recombinant pMHC molecules are listed in the format ‘Heavy chain/light chain/peptide’.

Streptamers:

H-2k^{b} Strep-tagIII/mβ2m-cys67-Alexa488/OVA$_{257-264}$
H-2k^{b} Strep-tagIII/mβ2m-cys67-Alexa488/SAINFEKL
H-2k^{b} Strep-tagIII/mβ2m-cys67-Alexa488/SIYNFEKL
H-2k^{b} Strep-tagIII/mβ2m-cys67-Alexa488/SIIQFEKL
HLA-A*02:01 Strep-tagIII/β2m/YFV NS4B$_{212-222}$

Multimers:

H-2k^b/mβ2m/OVA$_{257-264}$
H-2k^b/mβ2m/SAINFEKL
H-2k^b/mβ2m/SIYNFEKL
H-2k^b/mβ2m/SIIQFEKL
HLA-A*02:01/β2m/YFV NS4B$_{212-222}$

4.1.6 Software

Software	Supplier
FlowJo (v10.0)	FlowJo, LLC, Ashland, USA
GraphPad Prism 7	GraphPad Software, San Diego, USA
Microsoft Office 2019	Microsoft Corporation, Redmond USA
Single Cell FlowJo Analysis	Philipp Lückemeier, MIH, München

4.2 Methods

4.2.1 Mice

6-8-week-old, female C57BL/6 inbred mice were purchased from Envigo (Gannat, France). OT-1 mice were bred in-house on a C57BL/6 background. “6–24-week-old female and male CD45.1 (B6.SJL-Ptprca Pepcb/BoyJ) mice, 6–14-week-old female and male CD90.1 (B6.PL-Thy1a/CyJ) and *Rag*$^{-/-}$ mice (Rag1tm1Mom or Rag2tm1.1Cgn; every experiment was performed exclusively with one of each) were originally obtained from the Jackson Laboratory. Different congenic marker backgrounds of CD45.1/.2 and CD90.1/.2 were derived from in-house breeding (Buchholz et al. 2013).“ (Schober et al. 2020b). All mice were kept under SPF conditions in the Institut für Medizinische Mikrobiologie, Immunologie und Hygiene in Munich, Germany. Except for retrogenic TCR experiments (mixed), female mice were used exclusively for experiments.

4.2.2 Infections

For infections, different strains of *Listeria monocytogenes* (*L.m.*, kindly provided by Dietmar Zehn, Freising, Germany) were used. These strains are described in (Zehn et al. 2009): “Recombinant *Listeria monocytogenes* strains were generated that stably express chicken Ovalbumin (AA$_{134–387}$) containing either the native ligand SIINFEKL$_{257–264}$ or the APL listed in Supp. Fig. 2 [In this case A2, Y3, and Q4, comment by the author]. The designation of the APL indicates the substituted amino acid and the position within the SIINFEKL epitope. A previously described cassette [(Pope et al. 2001)] encoding for the expression of secreted Ova was manipulated by site-directed mutagenesis to insert the APL. The cassettes were cloned into a vector (pPL2) and stable Listeria recombinants were made as described [(Lauer et al. 2002)]”. *L.m.* were kept in glycerol stocks. To prepare for infections, stocks were thawed and a 10µl aliquot added to the BHI medium. The solution was placed into an incubation shaker at 37°C and 90rpm. OD measurements were periodically performed until an $OD_{600} \geq 0.05$ was reached, at which point exponential growth was assumed. The concentration of colony-forming units (CFU) was calculated via the formula $c = OD_{600} \times 12 \times 10^8$ in CFU/ml. The solutions were diluted in serial 1:10 dilutions in sterile PBS to reach the desired concentration for infection. For primary infections, 100µl PBS containing 5×10^3 CFU were injected i.v. For secondary infections, 100µl PBS containing 2×10^5 CFU were injected i.v. >28 days after primary infection.

4.2.3 Generation of TCR retroviruses and T cell retrogenic mice

TCR retroviruses were produced by Simon Grassmann and Kilian Schober. “For retrovirus production, Platinum-E packaging cells were transfected with the retroviral vectors (mp71, a kind gift from W. Uckert) encoding for the respective SIINFEKL-specific TCRs via calcium phosphate precipitation. The supernatant of the Platinum-E cells was collected at 48 and 72 h after transfection and purified from the remaining cells by centrifugation at 1,500rpm at 4 °C for 7 min. The supernatant was stored at 4 °C and used within 4 weeks after collection. […] Bone marrow was collected from the tibia and femur of 8–20-week-old donor mice (congenic matrix (Buchholz et al. 2013), *Rag-1*$^{-/-}$ or *Rag-2*$^{-/-}$). After red blood cell lysis, the cells were brought into single-cell suspension and stained with anti-mouse Ly6A/E (Sca-1) and anti-mouse CD3/CD19 antibodies. Propidium iodide (PI) was used for live/dead discrimination. Sorted Sca-1-positive CD3/CD19, negative cells were incubated at 37 °C in cDMEM, supplemented with 20 ng ml^{-1} murine IL-3, 50 ng ml^{-1} murine IL-6, and 50 ng ml^{-1} murine stem cell factor (SCF), for 3–4 d in a tissue-culture-treated 48-well plate (250,000–300,000 cells per 400 ml). Retroviral transduction of the expanded stem cells with the respective TCR was achieved by spinoculation. In brief, 400 µl of the combined Platinum-E supernatants were centrifuged at 3,000*g* at 32 °C for 2 h in a tissue-culture-untreated 48-well plate coated with RetroNectin according to the manufacturer’s instructions. Afterward, 200 µl were discarded and 200 µl of stem cells were added to a 2× stimulation medium containing transduction enhancers (40 ng ml^{-1} mIL-3, 100 ng ml^{-1} mIL-6, 100 ng ml^{-1} SCF, 1:100 dilution Lentiboost Solution A, 1:100 dilution Lentiboost Solution B) in a final concentration of 300,000 cells per 400 µl per well. Cells were then spinoculated at 800*g* at 32 °C for 1.5 h. After 2 d in culture, the transduced stem cells were suspended in FCS at 500,000–1,000,000 cells per 100 µl and injected intravenously into irradiated C57BL/6 recipient mice (two times 4.5 Gy, with a resting period of 4 h).” (Schober et al. 2020b)

4.2.4 Cell Isolation and Preparation

Spleens were harvested from infected mice on day 8 after primary infection or day 6 after secondary infection, respectively. The organs were placed in a 100µm cell strainer sitting in a petri dish, homogenized with the plunger of a syringe, and taken up in 5ml of RP10+ cell culture medium. The cell suspension was transferred to a 15ml falcon tube. The cell strainer was rinsed with an additional 5ml of RP10+, which was also added to the falcon tube. After centrifugation for 7min at 1500rpm to pellet the cells, the supernatant was discarded, and the cells were resuspended in 5ml of ACT for 5 minutes at room temperature to lyse erythrocytes. To stop lysis, 5ml of RP10+ was added. The solution was centrifuged for another 7min at 1500rpm, and the cell pellet was resuspended in 10ml flow cytometry (FCM) buffer. A 10µl aliquot was diluted in a Trypan blue solution for live/dead discrimination and cell concentration was determined with the use of a Neubauer chamber.

4.2.5 Generation of pMHC molecules

“pMHCs were generated as previously described (Nauerth 2012). In brief, H-2k^{b} and HLA-A*02:01 molecules with either a biotinylation substrate sequence for nonreversible multimers or *Strep*-tag residues for reversible multimers were refolded with either human or murine β2-microglobulin and a peptide. All pMHCs carry an artificially introduced cysteine residue (murine pMHCs at position 67 of the murine mβ2m, human pMHCs at a glycine serine linker by the *Strep*-tag). Murine pMHCs were refolded with either the SIINFEKL, A2, Y3, or Q4 peptides. Human pMHCs were refolded with either the LLWNGPMAV (YFV, NS4B) or the NLVPMVATV (CMV, pp65) peptides (synthesized by and purchased from Peptides and Elephants). *Strep*-tagged pMHCs were then conjugated with activated Alexa Fluor 488-maleimide dye (Thermo Fisher Scientific) at the cysteine residues. pMHCs with the biotinylation substrate sequence were biotinylated with a biotin-protein ligase. The refolded pMHCs were purified by size exclusion chromatography and stored at −80°C.” (Lückemeier et al. 2022)

4.2.6 Cell washing

For buffer changes or to remove staining agents from a cell solution, cells were washed '2.5 times' with the desired buffer. The vessel containing the cells was filled up with the desired buffer and centrifuged at 1500rpm for 7min (if the vessel was a 15ml or 50ml falcon tube) or 3min (if the vessel was a 96well plate), respectively. The supernatant was discarded, and the cell pellet was resuspended in the desired buffer and centrifuged again with the specifications stated above. The latter step was repeated once more. Finally, the cell pellet was resuspended in the desired buffer in the desired volume.

4.2.7 Surface antigen and live/dead staining

After cell isolation and washing in FCM buffer, the solution was rested on ice for at least 30min before staining. All following steps were performed on ice and direct light was avoided as much as possible. For FCM analysis, the cell suspension was aliquoted into V-bottom 96 well microplates with $5x10^6$-$2x10^7$ cells per well. For cell sorting, larger aliquots of the cell solution -the exact volume of which depended on the estimated proportion of the target subpopulation- were transferred to 15ml Falcon tubes for staining. Small aliquots were taken for single color samples and unstained controls. If Streptamer and/or non-reversible multimer staining was performed, it was performed at this step (see next section). Cell concentration was adjusted to $5x10^6$ cells per 50µl of FCM buffer. For surface antigen staining, the respective antibodies were added at the optimal concentration for staining intensity, previously determined by titration (usually 1:50 – 1:200). Single color samples were stained with a single antibody conjugated to the same fluorophore used in the test sample stainings. Samples were incubated for at least 20min. Cells were subsequently washed in FCM buffer. PI was added at 1:100 for live/dead discrimination 2min before analysis or cell sorting.

4.2.8 Streptamer or non-reversible multimer staining

The following quantities are per $5x10^6$ cells to be stained and were scaled accordingly. For streptamer staining, 1µg of strep-tagged pMHC was added to '1 test volume' -as specified by the supplier- of a Strep-Tactin conjugate (Strep-Tactin APC if not otherwise specified). For non-reversible multimer staining 1µg of biotinylated pMHC was added to 0,625µg of a Streptavidin conjugate (Streptavidin PE if not otherwise specified). The staining reagents were incubated in 50µl FCM buffer in the dark on ice for at least 30 minutes. The cell solution was pelleted, the supernatant discarded, and the pellet resuspended in the respective staining solution and incubated in the dark on ice for at least 45min. Antibodies for surface staining were added to this solution after 25min incubation time at the earliest. Cells were subsequently washed in FCM buffer and analyzed.

4.2.9 Flow cytometric TCR-ligand k_{off}-rate assay

k_{off}-rate assays were adapted from the method previously described (Nauerth et al. 2016).

Assay preparations

A 2mM D-biotin solution was made by diluting 10µl of a 10M D-biotin stock solution in 50ml of FCM buffer (this dilute solution could be stored in darkness at 4°C for up to a month). Moreover, for analysis on CyAn ADP flow cytometers, which uses over-pressure for sample acquisition, custom FCM tubes had to be made to inject D-biotin without disrupting sample acquisition. These tubes were constructed by piercing an ordinary polypropylene FCM tube with a 20G canula. The entry site of the canula was sealed with silicone. A 3-way-valve was connected to the canula. The valve and canula were then primed with FCM buffer to remove air.

Adoptions were made to perform the assay on the CytoFLEX flow cytometer to eliminate leakages from the canula entry site and reduce components and preparation time. The CytoFLEX uses under-pressure to acquire samples and allows access to the cell suspension

from the FCM tube opening. Thus, D-biotin was injected through a butterfly needle which was hung in the solution and primed with D-biotin. A pipette tip covered the needle to avoid contamination and was exchanged before reusing the injection contraption for the next sample. The tip was submerged in the cell suspension to ensure rapid mixing of the injected fluid.

Performing the assay

Splenocytes were isolated, prepared, and washed as described above. Firstly, a streptamer staining with the indicated streptamer was performed, as described above. For surface antigen staining, CD8α-Pacific Blue (importantly clone 5H10, as clone 53-6.7 was shown to lengthen the dissociation half-life (Voit 2021)) and CD19-PE-CF594 antibodies were added after 25 minutes and co-incubated for at least 20 minutes. Secondly, cells were washed and stained with a non-reversible multimer staining of the same specificity as the streptamer to achieve a double multimer staining. However, incubation was stopped by cell washing after exactly 10 minutes to not displace the streptamer staining. This staining allowed for continuous tracking of the double multimer-positive population after initiation of streptamer dissociation and the subsequent signal loss of the strep-tagged pMHC and the Strep-Tactin conjugates by gating on the non-reversible multimer signal. Lastly, cells were washed, resuspended in 200µl of FCM buffer, filtered through a nylon mesh, and transferred into the custom FCM tubes. The tubes were placed in a Peltier element cooling device -to keep the temperature at 5.5°C throughout the analysis- and read in. After 30 seconds, 1ml of a 2mM D-biotin solution was injected without interrupting the sample flow to initiate the dissociation. Samples were analyzed for 15 minutes. At least two replicates per sample were analyzed.

Assay analysis

FCM files were analyzed with FlowJo. Gates were used to identify lymphocytes in the FSC-A/SSC plot and singlets in the pulse width/FSC-A plot. From there, live and $CD19^-$, $CD8^+$, non-reversible $multimer^+$ events were identified by their fluorescence profile. The channel values of the pMHC-Alexa Fluor 488 and Strep-Tactin conjugate signals of these events, as well as their time stamp, were exported into a .csv or .txt file. Time values on the CytoFLEX were stored in seconds from acquisition start, whereas time values on the CyAn ADP were stored in 16-bit values where the acquisition start was represented as 0 and the preset maximum acquisition time (routinely set to 15min) represented as 65535.
To manually analyze the dissociations and determine their half-life, the data were imported into MS Excel and formatted into a table with the channel values mentioned above as columns and each event as a separate row. For data acquired on the CyAn ADP, the time values were converted from their bit values to seconds with the rule of three: If the maximum acquisition time (routinely set to 15min=900s) was represented as 65535, a bit value of 43690 of an event meant that that event was acquired 600s from the start.
After processing, data were imported into GraphPad Prism 7 and plotted over time. To account for small variations in the exact time of injection of d-biotin around the 30s mark, the time point at which the Strep-Tactin signal exhibited a sharp drop was identified on the graph and equated to the detectable start of the dissociation (routinely around 37s). For murine TCR-ligand k_{off}-rate assays, the Y0 of the dissociation was set to the MFI of the pMHC channel values of the events acquired before the starting point. For human TCR-ligand k_{off}-rate assays, this estimate of the Y0 of the dissociation was prohibitive because of the quenching effect the pMHC staining often exhibited before the start of the dissociation. The dissociation's half-life was calculated using Prism's constrained one-phase exponential decay analysis fitted to the pMHC channel values acquired after the start of the dissociation.

Single Cell FlowJo Analysis

To facilitate rapid TCR-ligand k_{off}-rate analysis, a program was developed that processed the data outputs from FlowJo, performed conversions and preliminary calculations, automated the data input into GraphPad Prism for analysis, and extracted dissociation parameters like half-life and k_{off}-rate in a table format. The application was written in Visual Basic .NET and requires Microsoft Windows as an operating system.

The .csv or .txt files exported from FlowJo (see above) were loaded into the program and thereby converted into a table format equivalent to the process described in the section above. The start of the dissociation was automatically determined by using the time value of the event for which the starkest drop in the Strep-Tactin conjugate channel value throughout the dissociation was calculated. The events were plotted on an integrated graphing software with time on the x-axis and pMHC and Strep-Tactin signals overlayed on the y-axis with a red line demarking the start time on the x-axis. The user was able to adjust the automatically calculated start time. When the user was satisfied with the parameters, the application initiated the analysis by exporting the data into one .txt file per dissociation in a format optimized for import into GraphPad Prism. The application then created and ran a Prism script which imported and analyzed the data with the constrained one-phase exponential decay fit in Prism, equivalent to the manual analysis described in the section above. After the analysis was done, the script created a Prism file with graphs of all dissociations and exported and tabulated all analysis parameters in a result .txt file for easy extraction.

In silico k_{off}-rate analysis

"Weighted means of the H-2K^b/OVA$_{257-264}$-TCR k_{off}-rates in 5.3 were calculated using the population size (in events) as weights. 'Dissociation fit outputs' of sets of TCRs were generated by concatenating their dissociation data exported from FlowJo and analyzing them like a single TCR dissociation data file. The equation used for 'equation predicted $t_{1/2}$' is detailed in 5.3.2. It calculates a weighted average of the known one-phase exponential decays of all kinetics in the population, resulting in a multiphase decay curve. The same one-phase decay model was fitted to this curve to yield a single $t_{1/2}$ which was plotted as 'equation predicted $t_{1/2}$.' The weighting of HLA-A2/YFV NS4B$_{214-222}$ k_{off}-rates in [**Figure 5-28**] was achieved by adjusting the frequency parameter in the aforementioned equation (for example to 50%/50% in [**Figure 5-28**A]) to yield the 'equation predicted $t_{1/2}$.' To weight kinetics for the 'dissociation fit output', data from a given dissociation were inserted into the merged data file multiple times to mimic the acquisition of more events for that dissociation. For example, to weight a dissociation with 3000 events 1:1 with a dissociation with 1000 events, the data of the latter were appended three times to the FlowJo export of the former and analyzed as one dissociation." Adapted from (Lückemeier et al. 2022). However, because most exact weightings of dissociations would lead to an infeasibly large data file, a tolerance of <2% difference from the assigned frequency was allowed for each dissociation. For example, to weight a dissociation with 3000 events exactly 1:1 with a dissociation with 2001 events, the data of the former would have had to be appended 667 times and the data of the latter 1000 times (contributing 2001000 events each to a simulated dissociation file with twice the number of events). Analyzing the resulting enormous data file would have been infeasible. With a tolerance of <2% (so 48.1% to 51.9% frequency for each dissociation) the dissociation counting 3000 events would only have had to be appended 2 times and the dissociation with 2001 events only 3 times, leading to a manageable amount of data to analyze as one dissociation without losing too much precision in the prediction analyses.

4.2.10 Phenotype and TRBV staining

Splenocytes were isolated, prepared, and washed as described above. Cell suspensions were split into 15 samples per spleen and transferred to 96 well microplates. Cell concentration was adjusted to 5x10^6 cells per 50µl of FCM buffer. Samples were incubated with Fc-block at the concentration specified by the supplier and 0.1µg EMA for 20 minutes under light. Samples were washed and stained with the respective non-reversible multimers as described above. For surface antigen staining, antibodies CD8α-Pacific Blue, CD19-PE-CF594, CD44-APC, CD62L-APC-Cy7, CD27-PE-Cy7, and 1 of 15 FITC-conjugated antibodies against TCR Vβ-chains Vβ2, Vβ3, Vβ4, Vβ5.1/5.2, Vβ6, Vβ7, Vβ8.1/8.2, Vβ9, Vβ10b, Vβ11, Vβ12, Vβ13, Vβ14, Vβ17a were added, and incubation continued for 20 more minutes. Cells were subsequently washed in FCM buffer and analyzed.

4.2.11 Peptide stimulation and intracellular cytokine staining

Splenocytes were isolated and prepared as described above. However, cells were kept in an RP10+ cell culture medium. Cells were counted and 11 samples per spleen with $5x10^6$ cells per sample were aliquoted into a 96-well flat bottom plate. The cells were pelleted and resuspended in 190µl of RP10+ cell culture medium per sample. The samples were either stimulated with varying doses of the indicated peptides with final concentrations ranging from 10^{-6}M to 10^{-14}M, stimulated with PMA/Ionomycin for positive control, or just medium for negative control. For peptide stimulation, 1mg of lyophilized peptide was dissolved in 100µl of DMSO, resulting in a 10^{-2}M peptide solution. 1µl of this solution was further diluted in 499µl of RP10+ cell culture medium to form a stock solution. 10µl of the stock solution was added to 190µl of the first sample, which equaled a peptide concentration of 10^{-6}M. 20µl of the stock solution was diluted 1:10 with 180µl of RP10+ cell culture medium. 10µl of this new dilution was added to 190µl of the second sample, which equaled a peptide concentration of 10^{-7}M. This process was repeated 7 more times, resulting in a peptide concentration of 10^{-14}M in the ninth sample. The remaining 2 samples were stimulated with PMA (1:4000) and Ionomycin (1:250) for positive controls or filled up with 10µl of medium for negative controls, respectively. Samples were placed in an incubator at 37°C, with 5% CO_2, and 95% relative humidity for 5h hours. After 1h, 1µl of Golgi Plug was added to each well while keeping agitation to a minimum. After incubation, cells were washed, transferred to a 96 well V bottom plate, and incubated with Fc-block at the concentration specified by the supplier and 0.1µg EMA for 20 minutes under light. Cells were washed again and stained with CD8α-FITC and CD19-PE-CF594 antibodies for 20min. Samples were washed again, resuspended in 100µl of Cytofix/Cytoperm per well, and incubated for 20min to fix and permeabilize the cells. In the meantime, a wash buffer was prepared by diluting 10x Perm Wash 1:10 in ddH_20, as well as a master mix containing an anti-IFN-γ-APC antibody mixed in the wash buffer at 1:400. Samples were washed in the buffer, resuspended in the master mix, and incubated for 20 minutes. Finally, cells were washed 2x in 1xPerm Wash, 1x in FCM buffer, and resuspended in 1%PFA. Samples were then read in. For analysis, the log(agonist) vs. response model provided in Prism 7 was fitted to the percentages of IFN-γ^+ of $CD8^+$ of increasing peptide dose samples, and the resulting $logEC_{50}$ was reported as functional avidity.

4.2.12 Tumor cell line preparation

The OVA-expressing PancOVA cell line (kindly provided by Dr. Grassmann, München, Germany) is described in (Jacobs et al. 2011): “The Panc02 cell line (C57BL/6) is derived from a methylcholanthrene-induced pancreatic adenocarcinoma. Panc02 cells were transfected with the OVA plasmid (pAC-Neo-OVA, kindly provided by Prof. T. Brocker)”. The OVA-expressing MC38-OVA cell line (also kindly provided by Dr. Grassmann, München, Germany) is derived from C57BL/6 murine colon adenocarcinoma cells and was transduced with the OVA plasmid (pMIG/MSCV-IRES-eGFP-OVA, pMIG was a gift from William Hahn (Addgene plasmid # 9044; http://n2t.net/addgene:9044; RRID: Addgene_9044)).

The cell lines were kept in 10ml DMEM+ cell culture medium in angle-necked cell culture flasks in an incubator at 37°C, 5% CO_2, 95% relative humidity, and split 3 days before using them for an assay. After 3 days, the cell lines routinely reached confluence and were harvested in a biological safety cabinet by discarding the cell culture medium, rinsing the cell culture flask in 10ml PBS, discarding the PBS, and adding 1ml of Trypsin. After 3min of incubation, 10ml of RP10+ cell culture medium was added, the cell suspension forcefully pipetted up and down to break cell-cell bonds, transferred to a 15ml tube, and centrifuged at 1500rpm. 1ml of cell suspension was left in the flask, 9ml of DMEM+ cell culture medium added, and the flask placed back in the incubator to continue the cell line. Lastly, the cell pellet was resuspended in an RP10+ cell culture medium and cell concentration was determined in a Neubauer chamber.

4.2.13 xCELLigence in vitro tumor killing assay

The OVA-expressing PancOVA cell line was used for target cells. Cells were prepared as described above and resuspended in a calculated volume of RP10+ cell culture medium to reach a cell concentration of 10,000 cells per 100µl.

Special 96-well E-plates were filled with 100µl of RP10+ cell culture medium in each well and the space between wells was filled with ddH_2O to keep temperature fluctuation at a minimum. The plates were placed in the Real-Time Cell Analysis (RTCA) MP inside an incubator and zeroed. Next, 100µl of the PancOva cell suspension (≙10,000 cells) was pipetted into each well using the reverse pipetting technique to reduce volume fluctuations. The plates were subsequently left in a biological safety cabinet at room temperature without agitation for 30min to let the cells settle to the bottom of the plate before placing it back in the RTCA MP. The experiment was then started in the RTCA MP software.

The following day, splenocytes were isolated and prepared under sterile conditions 6 days after recall infection as described above. $10x10^7$ cells per spleen were resuspended in a sterile H-2K^b/OVA$_{257-264}$ streptamer solution, irrespective of the inducing *L.m.* strain, as described above. CD8α-Pacific Blue (clone 5H10-1) and CD19-PE-CF594 antibodies were used for surface antigen staining, as described above. Cells were washed and resuspended in 5ml sterile FCM buffer, filtered through a nylon mesh and 5µl of PI was added just before sorting.

Living, CD19$^-$, CD8$^+$, streptamer$^+$ cells were sorted into 1ml RP10+ cell culture medium and 20µl of the d-biotin stock solution was added to dissociate streptamers. Cells were pelleted and resuspended in a calculated volume of RP10+ cell culture medium to reach a cell concentration of 50,000 T cells per 170µl. The experiment on the RTCA MP was paused, the plate was taken out of the device, and placed in a biological safety cabinet. 170µl of the medium was carefully pipetted from every sample well. Either 170µl (≙50,000 T cells) or 85,5µl (≙25,000 T cells) of the sorted cell suspension were added to the PancOVA cells in duplicates or triplicates per sample condition. All wells were filled up to 200µl with RP10+ cell culture medium, including wells that received no T cells, serving as negative controls. E-Plates were left at room temperature for 30 minutes to let T cells set, as per supplier recommendation, creating a bump in cell indices after placing the plates back in the RTCA MP. Additions were carried out ca. 24 hours after initial seeding during which a doubling of PancOVA cell numbers was assumed. Cell indices were normalized to addition time points and killing capacity (cytolysis) quantified as the average difference in normalized cell index of sample wells (T cells added) to control wells (medium added) after 48 hours.

4.2.14 In vivo tumor killing assay

Splenocytes were sterilely isolated and prepared 8 days after primary infection, as well as the splenocytes of an uninfected 'feeder' mouse, as described above. Splenocytes of the feeder cells were pelleted, resuspended in 100µl of sterile FCS per 400,000 cells, and a 96 well V bottom filled up with 100µl of this solution per well. Cells of infected mice were counted and stained with an H-2K^b/OVA$_{257-264}$ sterile streptamer solution, irrespective of the inducing *L.m.* strain, as described above. CD8α-Pacific Blue and CD19-PE-CF594 antibodies were added for surface staining, as described above. Cells were washed and resuspended in 5ml sterile FCM buffer, filtered through a nylon mesh and 5µl of PI was added just before sorting. 2x 25,000 living, CD19$^-$, CD8$^+$, streptamer$^+$ cells per spleen were sorted into the prepared 96 well V bottom plate containing the feeder cells. Meanwhile, recipient mice were irradiated with 5Gy.

After all samples were sorted, 2µl of the d-biotin stock solution was added to each well to dissociate streptamers. Samples were pelleted and resuspended in 100µl of sterile PBS per well. 25,000 sorted cells were administered intraperitoneally per irradiated recipient mouse. Controls received saline solution after irradiation. The following day, the OVA-expressing MC38-OVA cell line was prepared as described above and resuspended in a calculated volume of sterile PBS to reach a cell concentration of $1x10^6$ cells per 200µl.

$1x10^6$ tumor cells per recipient mouse were injected subcutaneously into the flank. Recipients were surveilled every 1-3 days and sacrificed if the tumor reached a size of ≥15mm in any dimension. Alternatively, after a maximum of 50 days of not reaching critical tumor burden or if ulcers started to form, mice were sacrificed and censored in the analysis.

4.2.15 Preparation of human samples

“For PBMC preparation, donor blood was obtained from healthy volunteers. Written informed consent was obtained from the donors, and usage of the blood samples was approved according to national law by the local Institutional Review Board (Ethikkommission der Medizinischen Fakultät der Technischen Universität München). PBMCs were extracted from whole blood, pre–diluted 1:1 with sterile filtered 1x PBS (pH 7.4), by density gradient centrifugation for t = 20 min, T = 20°C, 2500 rpm on a layer of Ficoll (Biochrom). Separated PBMCs were washed in 50 ml pre–equilibrated RPMI 1640, centrifuged (t = 10 min, T = 4°C, 1500 rpm), and the resulting pellet re–suspended in 1 ml pre–equilibrated CTL medium (RPMI 1640 supplemented with 10 % heat inactivated FCS and 100 U/ml streptomycin, 100 U/ml penicillin, 100 U/ml gentamycin (SC+)). Cells were counted using a Neubauer hemocytometer and adjusted to the desired cell density. […] Cells for FCM analysis and sorting were washed twice with 4°C FCM buffer. Antibodies for cell surface staining were CD3–BV650, CD8–PE, CD45RA–PeCy7, CCR7–FITC, and CD19–ECD. Antigen–specific $CD8^+$ T cells were stained using non–reversible pHLA:Streptavidin […]. For live/dead discrimination, propidium iodide (PI) was used. In brief, a maximum of $1x10^8$ cells/ml were first incubated with CCR7–FITC for 15 min at 37°C. The following steps were carried out on ice with cold FCM buffer. Cells were stained with pHLA multimer–BV421 followed by pHLA multimer–APC, each for 30 min on ice in the dark under agitation. Afterward, CD3–BV650, CD8–PE, CD45RA–PeCy7, and CD19–ECD antibodies were added together, for 20 min on ice in the dark. Cells were sorted using MoFlo (Beckman Coulter) and samples were analyzed using a CyanP6 color flow cytometer.” Adapted from (Peter Patrick Huppertz 2016).

4.2.16 Feeder Cell Culture

“To generate allogenic feeder cells, PBMCs were irradiated (approx. 45 Gy.) and washed twice in warm RPMI 1640. Afterwards, irradiated cells were transferred into CTL medium containing 500units/ml IL-2 and 1µg/ml PHA. Cell density was adjusted to 10^6 cells/ml, which results in 50.000 feeder cells per 50µl that were transferred per well of a 384 deep well plate. At d7, wells were checked for potential accumulation of acid metabolic products, indicated by pH indicator phenol red within the Ctl medium that turns yellow as soon as the pH drops below 7.3. If the medium turned yellow, fresh Ctl medium supplemented with 500units/ml IL-2. If 90% confluence was reached, clones were passaged into 96 well plate to provide additional space for clones in order to avoid decreased expansion rate due to cell-cell inhibition. For this purpose, cells were suspended by pipetting up and down and cell solution was transferred to new plate. Afterwards wells were washed with medium to collect remaining cells.” Adapted from (Peter Patrick Huppertz 2016).

5. Results

5.1 TCR-ligand k_{off}-rates of murine ex vivo CD8$^+$ T-cell populations specific for OVA

While TCR-pMHC k_{off}-rates of monoclonal T-cell populations, such as OT-1 T cells, have been intensely studied, dissociation kinetics of polyclonal populations are relatively understudied. Previous works have merged monoclonal dissociations of T cells sorted from a single polyclonal population to approximate a population-wide measure of avidity (Nauerth et al. 2013; Allard et al. 2017). Measuring kinetics of T-cell populations on a flow cytometer without the need for cell sorting was described by Nauerth et al. utilizing a double multimer staining technique (Nauerth et al. 2016). With the help of that methodology, TCR-ligand k_{off}-rate measurements of human ex vivo T-cell populations were described for the first time in that publication. However, this has not yet been demonstrated for murine populations. The following experiments aimed to establish measurements of TCR-ligand k_{off}-rates of murine ex vivo antigen-specific CD8$^+$ T-cell populations. After establishing the methodology with a model monoclonal population, the goal was to expand it to polyclonal T-cell populations and study these physiological populations in more detail.

5.1.1 Ex vivo TCR-ligand k_{off}-rates via double multimer staining

Ovalbumin$_{257-264}$ (amino acid sequence = SIINFEKL, here called 'OVA') is an established model epitope in immunological research. Its immunogenicity makes it particularly well suited to induce antigen-specific CD8$^+$ T-cell populations. OT-1 T cells express a transgenic TCR specific for the epitope H-2K^b/OVA. OT-1 transgenic mice harbor a large monoclonal CD8$^+$ OT-1 T-cell population as well as CD8$^+$ T cells not expressing the OT-1 TCR, which are thus largely not specific for OVA. This provides an excellent model for measuring TCR-ligand k_{off}-rates of antigen-specific murine ex vivo CD8$^+$ T-cell populations among a background of unspecific T cells via double multimer staining.

To do so, splenocytes of 6-8 weeks old OT-1 transgenic mice were stained with a reversible and an irreversible OVA multimer, resulting in double-multimer staining of OVA-specific, CD8$^+$ T cells (**Figure 5-1**A, D). CD8α and CD19 mAb were added as surface antigen staining, and PI was added for live/dead discrimination. After baseline acquisition, d-biotin was added—without interrupting the analysis—to disrupt the reversible multimer and start the dissociation. The non-reversible multimer provided a steady signal to track antigen-specific T cells among non-specific cells, while the reversible Strep-Tactin-APC backbone rapidly dissociated from the cell surface (**Figure 5-1**B, C, E). The now monomeric, fluorescently labeled pMHCs dissociated from bound TCRs over time, enabling TCR-pMHC k_{off}-rate measurements directly ex vivo by fitting an exponential decay model to the signal decay (**Figure 5-1**F, comparable methodology to (Nauerth et al. 2016)).

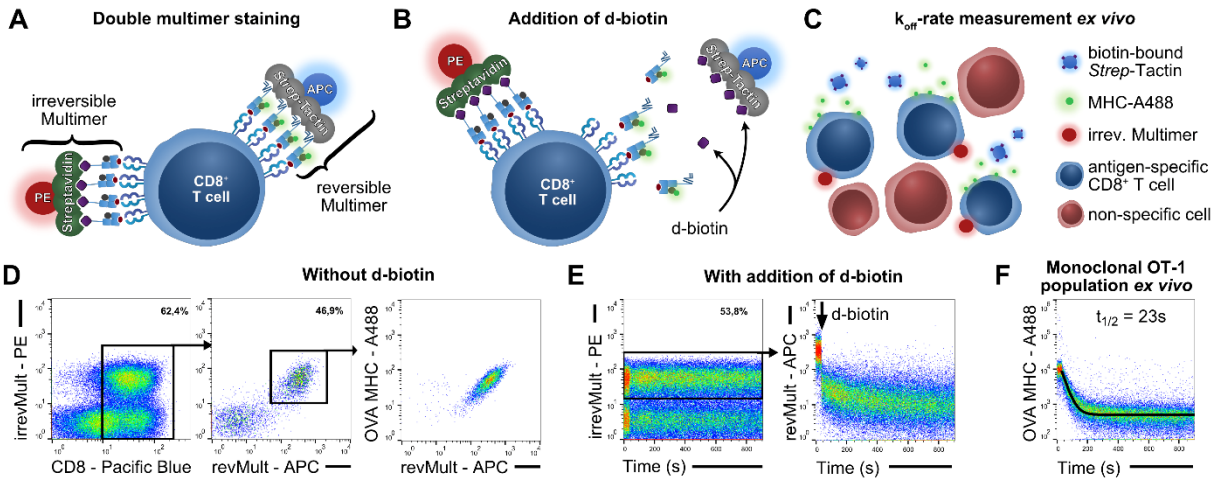

Figure 5-1. Measuring TCR-pMHC k_{off}-rates of OT-1 T-cell populations ex vivo via double multimer staining. A, B, C: Schematic illustration of k_{off}-rate measurements ex vivo. CD8 molecules are omitted for simplicity. **A**: Ex vivo samples get stained with biotinylated pMHC-Streptavidin multimers (irreversible Multimer) and strep-tagged pMHC-*Strep*-Tactin multimers (reversible Multimer). Antigen-specific CD8⁺ T cells bind both multimers. **B**: The addition of d-biotin facilitates rapid dissociation of the *Strep*-Tactin backbone and avidity-dependent dissociation of now monomeric pMHC molecules. **C**: Antigen-specific CD8⁺ T cells are distinguished from non-specific cells ex vivo without prior sorting and despite the signal loss of the reversible multimer via the irreversible multimer signal. **D, E**: Gating strategy for TCR-pMHC k_{off}-rate measurements. Splenocytes were stained with CD8 mAb, biotinylated H-2K^b/OVA$_{257-264}$ pMHC-Streptavidin multimers (irrevMult) and strep-tagged H-2K^b/OVA$_{257-264}$ pMHC (OVA MHC)-*Strep*-Tactin multimers (revMult). The purity of reversible multimer⁺ events among irreversible multimer⁺ events regularly exceeded 90%. Pregated on living, CD19⁻ lymphocytes. **E**: To track OVA-specific cells during dissociation, a gate was kept on irreversible multimer⁺ cells while the reversible multimer rapidly dissociated after the addition of d-biotin. **F**: Representative plot of ex vivo monomeric OVA MHC dissociations and pMHC-TCR k_{off}-rate measurements of a monoclonal OT-1 population pre-gated as described in (**D, E**). Adapted from (Lückemeier et al. 2022).

5.1.2 Induction and staining of OVA-specific CD8⁺ T-cell populations

After establishing ex vivo analyses of monoclonal populations, the next step was to apply the methodology to polyclonal T-cell populations from a physiological immune response. To induce those populations with specificity toward OVA, a strain of *Listeria monocytogenes* expressing OVA (*L.m.* OVA) was used to infect mice (**Figure 5-2**A). 8 days after the infection, mice were sacrificed, their splenocytes isolated and stained as described in the previous section. OVA multimer-binding populations were robustly identifiable and varied dissociation kinetics were acquired in all samples tested (**Figure 5-2**B, C). Using the same analysis as was previously used for human monoclonal dissociation kinetics, the data from these murine polyclonal dissociations were exported from FlowJo, imported into GraphPad Prism and an unconstrained one-phase exponential decay was fitted to it (**Figure 5-2**D).

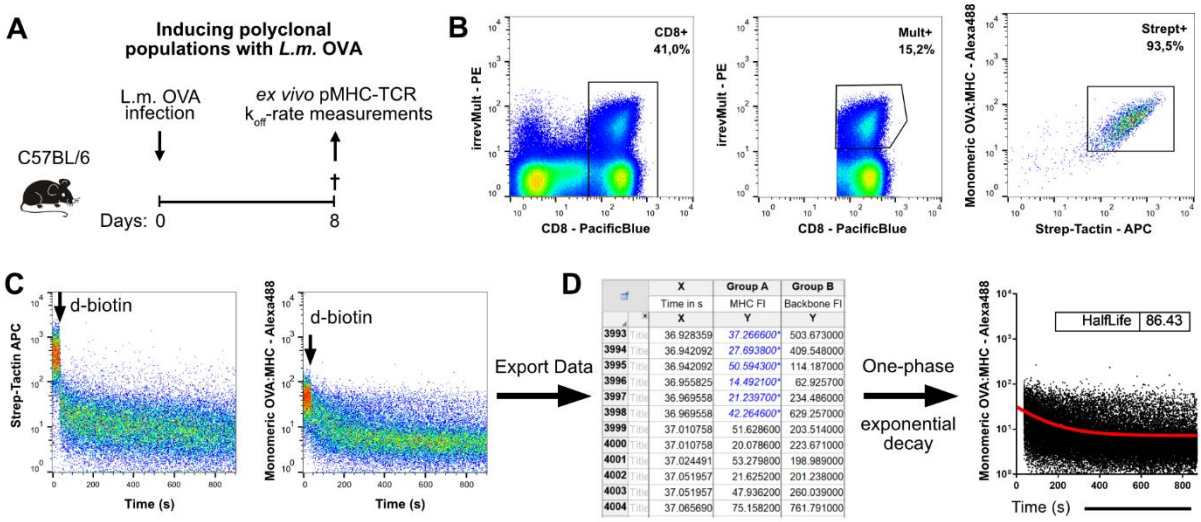

Figure 5-2. Inducing OVA-specific murine T-cell populations with *L.m.* OVA and measuring their TCR-pMHC k_{off}-rates ex vivo. A: Experimental design. Mice were infected with *L.m.* OVA, sacrificed on d8 p.i. and H-2K^b/OVA$_{257-264}$-TCR k_{off}-rate measurements of splenocytes were taken. **B**: Gating strategy for TCR-pMHC k_{off}-rate measurements of *L.m.* OVA-induced T-cell populations. Splenocytes were stained with CD8 and CD19 mAb, biotinylated H-2K^b/OVA$_{257-264}$ pMHC-Streptavidin multimers, and strep-tagged H-2K^b/OVA$_{257-264}$ pMHC (OVA MHC)-Strep-Tactin multimers. The purity of reversible multimer$^+$ events among irreversible multimer$^+$ events regularly exceeded 90%. Pregated on living, CD19$^-$ lymphocytes. **C**: Representative plot of ex vivo Strep-Tactin or monomeric OVA MHC dissociations, respectively, with the addition of d-biotin around 30s after the start of acquisition and pMHC-TCR k_{off}-rate measurements of an *L.m.* OVA-induced T-cell population pre-gated as described in (**B**). **D**: Schematic data analysis. Data from the OVA MHC dissociation described in (**C**) was exported from FlowJo, imported into GraphPad Prism and an unconstrained one-phase exponential decay was fitted to it.

5.1.3 Unconstrained vs. constrained one-phase exponential decay model for k_{off}-rate analyses

Most dissociations analyzed this way exhibited a good curve fitting. Some dissociations however had a rapid signal decay just seconds after the addition of d-biotin (**Figure 5-3**A). Using the model described above, the curve fitted to these data paradoxically showed a long dissociation half-life. The reason for this misfitting appeared to be that only the data acquired after the dissociation of the Strep-Tactin backbone was inserted into the model. Unaware of the initial staining intensity, the algorithm, therefore, tried to fit an exponential decay curve to an almost finished decay estimating a much lower initial staining intensity which resulted in evidently too long dissociation half-lives (**Figure 5-3**A).

The MFI measured in the seconds before d-biotin could provide the necessary information on the start parameters of the dissociation. The rationale was that, before the addition of d-biotin, the staining intensity of fluorescently labeled murine pMHC should approximate the staining intensity at the start of the dissociation, *i.e.*, directly after disruption of the reversible multimer through d-biotin. This contrasts with human dissociations where the pMHC-bound fluorophore is subject to quenching by the Strep-Tactin backbone, resulting in a low initial staining intensity with a marked increase shortly after the addition of d-biotin (Nauerth 2012). With murine reagents, however, such an increase (or dequenching) has never been observed. The reason for this could be that the distance of the fluorophore to the Strep-Tactin molecule is larger for murine recombinant pMHC, for which the fluorophore is bound to the mβ2m, compared to human recombinant pMHC, for which the fluorophore is bound to the Strep-tag (Nauerth 2012).

To improve the fit of the model, a constraint for the origin (Y-intercept or ‘Y0’ parameter) of the fitted decay curve was therefore set to be equal to the MFI measured in the seconds before d-biotin was added to the sample (**Figure 5-3** D).

An important detail to consider with this methodology is the travel time of the cells inside the tubing of the flow cytometer. Biologically, the TCR-ligand dissociation should start promptly after adding d-biotin to the sample tube, which was performed around 30s after starting sample acquisition. However, during analysis, the rapid drop in the Strep-Tactin signal was not observed until 7 seconds later, usually around 37 seconds after the start of the sample acquisition (**Figure 5-3**B). This is likely because cells that encountered the d-biotin need time to travel through the tubing of the flow cytometer for measurement at the laser line and photo multiplier tubes. A backlog of cells already inside the tubing of the flow cytometer at the time of addition of d-biotin to the sample tube did not encounter d-biotin, did not exhibit a dissociation, and therefore provided a steady pMHC - Strep-Tactin signal until several seconds later (**Figure 5-3**B, C). This lag time was determined to be around 7 seconds for all flow cytometers used in this project at medium to high acquisition speeds. Importantly, this meant that the first 7 seconds of the dissociations were not observable with this setup and that the first data measured after this lag time did not correspond to the first, but the seventh second of the biological dissociation, as evidenced in a sudden, small downward displacement of the dissociation curves (**Figure 5-3**B).

Thus, for the Y0-constrained one-phase exponential decay analysis, the curve was constrained to start with a Y0 equal to the MFI measured in the seconds before d-biotin was added, followed by 7 seconds of no data, followed by the dissociation data acquired starting 7 seconds after the addition of d-biotin. This provided visibly better fitting decay curves, especially for rapid TCR-ligand dissociations (**Figure 5-3**D). To test how this methodology compared to the unconstrained analysis in the monoclonal setting, five OT-1 dissociations were analyzed with both methods. The constrained method consistently yielded a slightly, but significantly lower $t_{1/2}$ (**Figure 5-3**E). One contributing factor to this difference could be 'dangling' pMHC molecules unbound by TCRs at the moment of disruption of the reversible multimer. They would contribute to the MFI before the addition of d-biotin, but not participate in the TCR-ligand dissociation and therefore skew the curve towards a faster dissociation with the constrained method. Collectively, the relatively small effect on the $t_{1/2}$ was weighed against the superior curve fit, and the Y0-constrained one-phase exponential decay analysis was chosen as the preferred method to analyze murine polyclonal TCR-ligand k_{off}-rates in this project. All murine $t_{1/2}$ displayed from this point on were obtained from this constrained analysis.

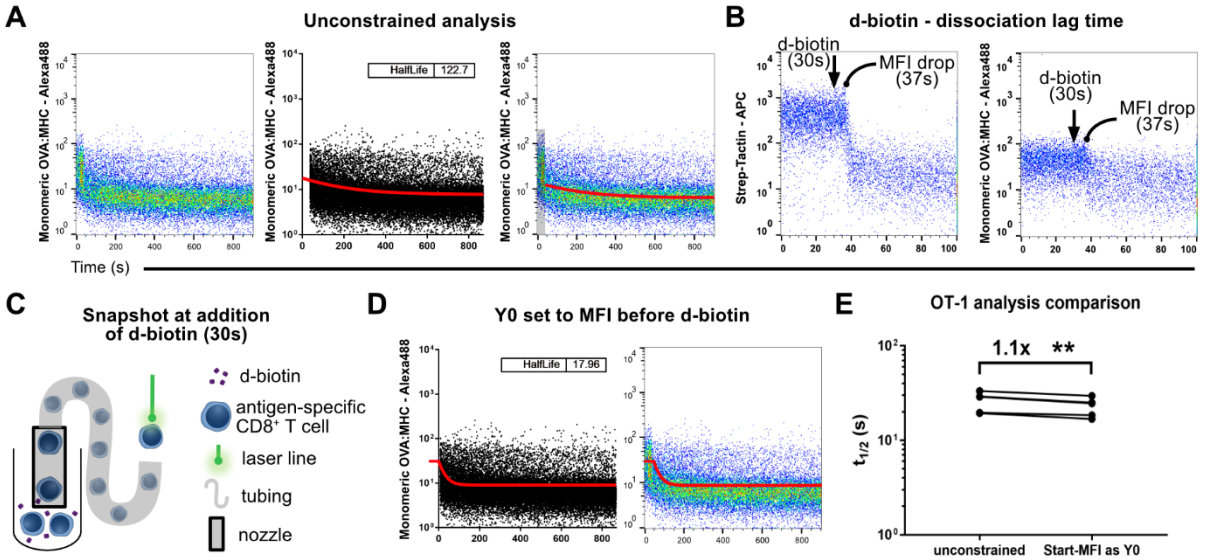

Figure 5-3. A Y0-constrained one-phase exponential decay model provides superior curve fits especially for rapid murine TCR-ligand dissociations. A: Representative plot and analysis of rapid monomeric OVA MHC dissociation measurements of *L.m.* OVA-induced T-cell populations. Splenocytes were stained with CD8, CD19 mAb, irreversible OVA multimers, and reversible OVA multimers. Pregated on living, $CD19^-$, $CD8^+$, $irrevMult^+$ lymphocytes. The middle panel shows the output of the GraphPad Prism unconstrained one-phase exponential decay fit of the dissociation data. The right panel shows an overlay of the fitted curve and the FCM plot. The transparent grey bar highlights that the

underlying data was not analyzed by the unconstrained model. **B**: Zoom in on the Strep-Tactin and OVA MHC dissociations of the population displayed in (**A**). d-biotin was added around 30s after the start of acquisition while a first, rapid drop in both dissociations occurred around 37s. **C**: Schematic of the postulated state of the flow cytometer shortly after the addition of d-biotin. Cells in the sample tube encounter d-biotin and exhibit disruption of the reversible multimer (omitted for simplicity), while cells already in the tubing do not. This leads to a lag time between the addition of d-biotin and the measurement of the first cells which encountered d-biotin. **D**: Y0-constrained analysis of the dissociation shown in (A). The Y0 of the exponential decay model fitted to the dissociation was set to the MFI of the events acquired before the addition of d-biotin. See section 4.1.3 for details. **E**: Comparison of unconstrained vs. Y0-constrained analysis of five OT-1 dissociations. Each dot represents a dissociation (n = 5 from 1 experiment). There was a 1.1-fold difference in the mean of the groups. Paired t-test was performed between the unconstrained and Y0-constrained group. p-values ** < 0.01.

5.1.4 Induction and staining of OVA-specific recall populations

Previous studies have reported an increase in avidity after a secondary immunization with the same epitope (Busch und Pamer 1999; Savage et al. 1999). This phenomenon has been termed 'avidity maturation' and has been endorsed as an important contributing factor to immunity to infections. To explore global k_{off}-rates of recall populations and find whether there were observable differences in avidity with the setup described above, mice were reinfected with *L.m.* OVA after >4 weeks of convalescence from a primary infection with the same pathogen (**Figure 5-4**A). Mice were sacrificed 6 days after secondary infection, the spleens prepared, and TCR-ligand k_{off}-rate assays performed as described above. Multimer-binding populations of recall populations, too, were robustly identifiable, and varied dissociation kinetics were acquired in all samples tested (**Figure 5-4**B, C).

Compared to dissociations acquired on d8 after primary infection, $t_{1/2}$ of recall populations exhibited a similar range of values with a non-significant increase in the average half-life of the latter (**Figure 5-4**D). This is in line with 'avidity maturation' of polyclonal T-cell populations upon recall responses (Busch und Pamer 1999; Savage et al. 1999), although in this experimental setting the extent of avidity maturation was only moderate.

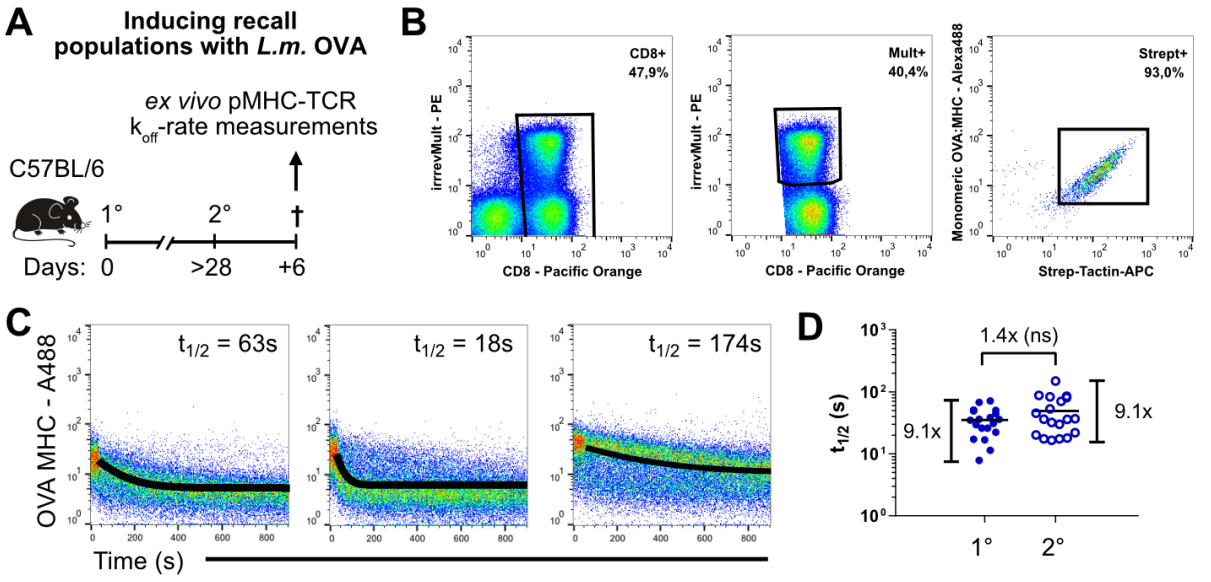

Figure 5-4. Inducing OVA-specific murine recall T-cell populations with *L.m.* OVA and measuring their TCR-pMHC k_{off}-rates ex vivo. A: Experimental design. Mice were infected with *L.m.* OVA, convalesced for over 4 weeks, and received a recall infection with *L.m.* OVA thereafter. On d6 after recall infection, H-2K^b/OVA$_{257-264}$-TCR k_{off}-rate measurements of splenocytes were performed. **B**: Gating strategy for TCR-pMHC k_{off}-rate measurements of *L.m.* OVA-induced recall T-cell populations. Splenocytes were stained with CD8, biotinylated H-2K^b/OVA$_{257-264}$ pMHC-Streptavidin multimers, and strep-tagged H-2K^b/OVA$_{257-264}$ pMHC (OVA MHC)-Strep-Tactin multimers. The purity of reversible multimer$^+$ events among irreversible multimer$^+$ events regularly exceeded 90%. Pregated on living,

CD19$^-$ lymphocytes. **C**: Representative monomeric OVA MHC dissociations and pMHC-TCR k_{off}-rate measurements of splenocytes described in (**A**). **D**: Summary of $t_{1/2}$ of pMHC-TCR k_{off}-rate measurements of CD8$^+$ OVA multimer$^+$ splenocytes 8 days after the primary (1°) and 6 days after recall infection (2°) with *L.m.* OVA. Each dot represents a mouse (n = 19 each from >10 independent experiments). Bars indicate means. There was a 1.4-fold increase in the average $t_{1/2}$ from 1° to 2° and 9.1-fold ranges between the lowest and highest $t_{1/2}$ in both infection settings. An unpaired t-test was performed between 1° and 2°. ns = not significant (p-value = 0.12). (**A, D**) adapted from (Lückemeier et al. 2022).

5.1.5 Confirmation of polyclonality via TCR-Vβ-chain staining

Polyclonality of the assessed populations was central to this project. To corroborate the polyclonal nature of the infection-induced populations, their T-cell receptor beta variable region (TRBV) repertoires were evaluated via TCR-Vβ-chain staining. The populations were isolated as described above and were split into 15 samples, stained with CD8, CD19, and CD44, as well as 1 of 15 Vβ-chain antibodies, and stained with a non-reversible OVA$_{257-264}$ multimer. CD44 was used to confirm that almost all multimer-binding cells were activated (*i.e.*, CD44^{hi}, **Figure 5-5**A). Interindividual multimer$^+$ populations exhibited great differences in TRBV frequencies without the dominance of a single TRBV chain in any given population (**Figure 5-5**B, C). This reflected a certain variance between individuals and demonstrated the polyclonality of the induced OVA MHC-binding CD8$^+$ T-cell populations.

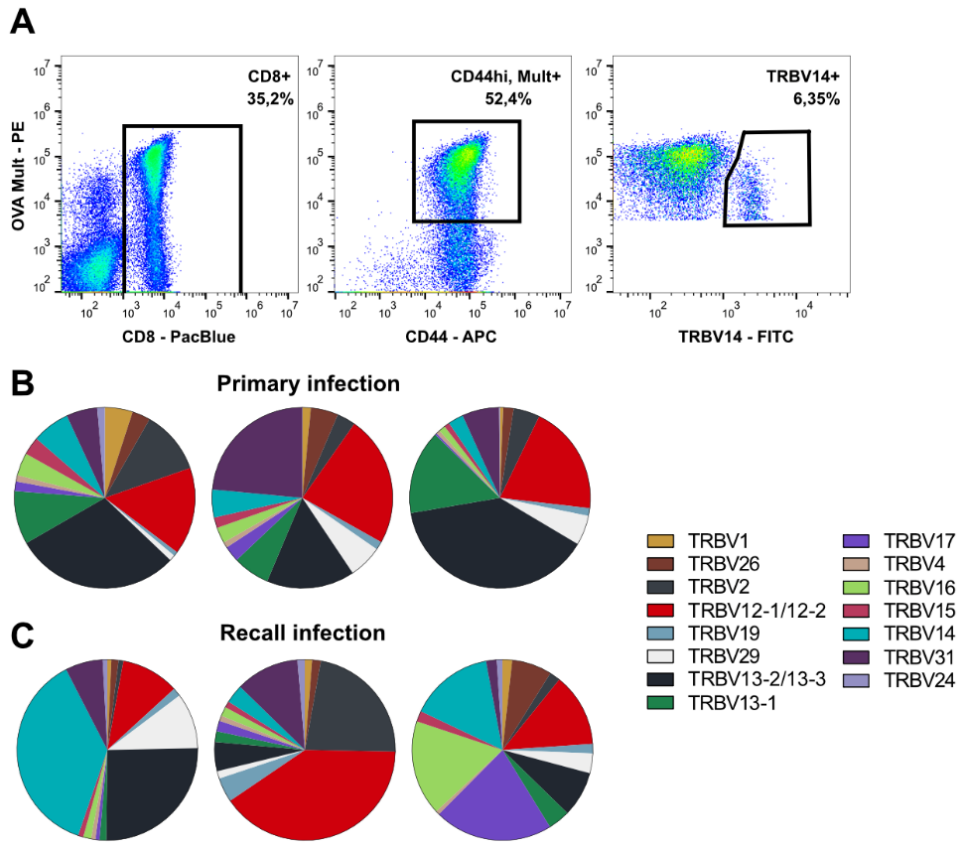

Figure 5-5. TRBV repertoire of CD8$^+$, non-reversible OVA$_{257-264}$ multimer$^+$ cells on d8 p.i. or d6 post recall infection with *L.m.* OVA. A: Gating strategy for TRBV repertoire measurements of *L.m.* OVA-induced T-cell populations. Splenocytes were stained with CD8, CD19, CD44, and 1 of 15 Vβ-chain antibodies, as well as biotinylated H-2K^b/OVA$_{257-264}$ pMHC-Streptavidin multimers (OVA Mult). Pregated on living, CD19$^-$ lymphocytes. **B, C**: Representative TRBV repertoires measured by flow cytometry showing polyclonality of CD8$^+$ OVA multimer$^+$ splenocytes 8 days p.i. (**B**) and 6 days after recall infection (**C**) with *L.m.* OVA. Each pie chart shows the repertoire of one mouse. Charts representative of 2-3 independent experiments with n = 2-3 mice each. (**B, C**) Adapted from (Lückemeier et al. 2022).

5.2 Automating the analysis of TCR-ligand k_{off}-rates with a custom software solution

The analysis of TCR-ligand k_{off}-rate assays requires exporting, structuring, and formatting dissociation data from the flow cytometry analysis software FlowJo and importing it into the graphing software GraphPad Prism. Once imported, pre-dissociation values need to be excluded, exponential decay models fitted to the data, and fitting results exported into a results file. With the constraint analysis described in the previous section, even more steps need to be performed, including calculating the initial MFI, adding the constraint, and identifying and shifting all time values by the pre-d-biotin acquisition time (see methods section for more details). The analyses then need to be visualized as graphs and the half-lives tabulated for grouped analysis. Depending on the number of events per dissociation, analyzing just 5-8 dissociations with 2-3 repetitions each required a full day's work with continuous intervention by a trained individual. This time requirement was prohibitive for the large-scale TCR-ligand k_{off}-rate experiments planned for this thesis. Thus, a custom software was programmed by me to automate all steps mentioned above. With the software 'Single Cell FlowJo Analysis', the dissociation data exported from FlowJo are formatted, visualized, and analyzed by providing a script for GraphPad Prism. The basic functionality of the software and data analysis steps are described in the section below.

5.2.1 Workflow

After gating the experimental data, the channel values of the MHC, Strep-Tactin, and time channel are exported from FlowJo and saved in .csv or .txt files as comma-separated values. Upon opening 'Single Cell FlowJo Analysis' and clicking 'Browse…', the user gets prompted for files of that format. The files can be loaded in bulk, upon which they are formatted into data tables and visualized as graphs (**Figure 5-6**A). The program then recognizes the timepoint at which d-biotin has been added through the stark MFI drop in the Strep-Tactin channel. In detail, the timepoint is identified by sorting the channel data chronologically, dividing them into three sections, and comparing the difference in MFI. The two sections with the biggest MFI difference are assumed to contain the stark MFI drop caused by the d-biotin. These two sections are kept, concatenated, again divided into three sections, and their MFI difference compared. This process repeats recursively until only three data points remain, the midmost of which is assumed to be the first cell that encountered d-biotin. This algorithm robustly marked data values in the correct time interval (time at the addition of d-biotin plus estimated travel time, data not shown). The calculated time point is then marked by a red line on the graph (**Figure 5-6**A). The user can manually correct the position of this line. This feature helped to speed up and standardize the analysis of TCR-ligand k_{off}-rate assays and to reduce inter-user variability.

When the user is satisfied with the data format, they can press 'Calculate Off-rates', after which they can choose the calculation settings (**Figure 5-6**B). They can choose to analyze the data with an unconstrained or a constrained one-phase exponential decay fit (as outlined in 4.1.3). When the user clicks start, the application exports the formatted data into GraphPad Prism-compliant .txt files, creates a custom Prism script, and runs it. The script imports these .txt files, fits the chosen one-phase exponential decay model to the data, and writes the fit parameters into a result .txt file. From there, the parameters can be conveniently pasted and summarized (**Figure 5-6**D). The application also provides a Prism file with the imported data, finished analyses and customized graphs of the dissociations for the user to examine and utilize, *e.g.*, in publications (**Figure 5-6**C).

In summary, the custom software 'Single Cell FlowJo Analysis' reduced inter-user variability, produced easy-to-process tables and graphs, and sped the analysis of TCR-ligand k_{off}-rate up manyfold, enabling the large-scale experimental setups of this thesis.

A

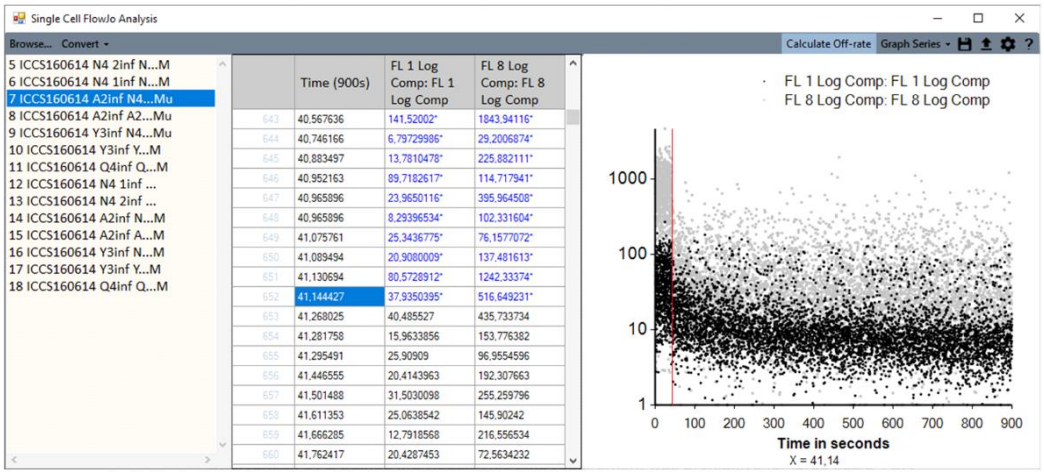

B

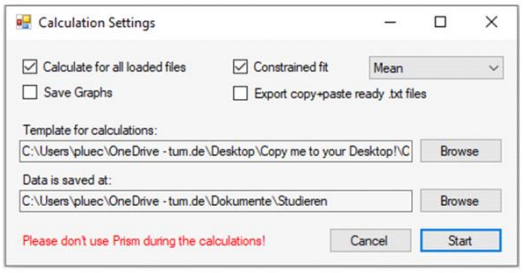

C

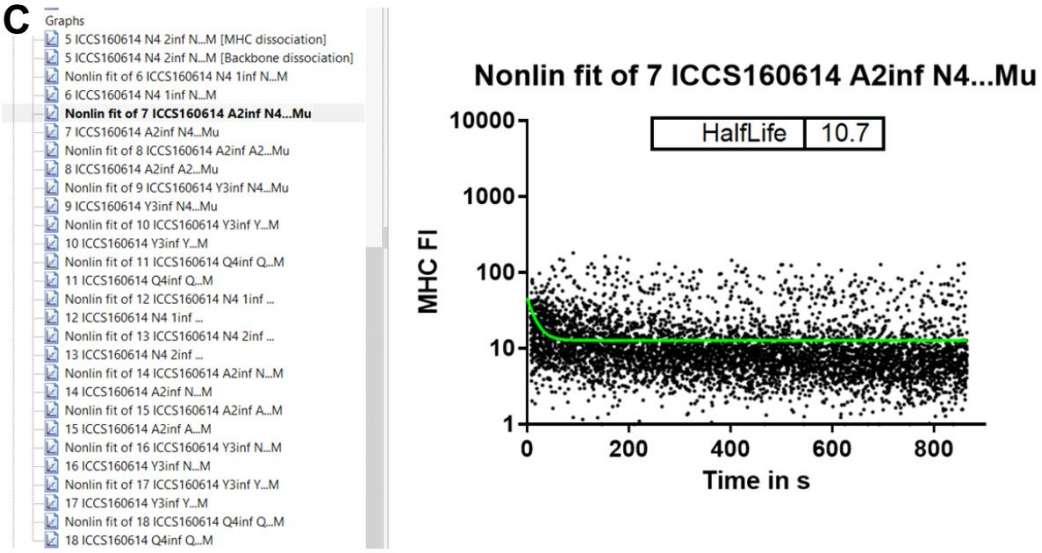

D

	A	B	C	D	E	F
1	Dissociation - One phase exponential decay	Best-fit values:	Y0	NS	K	HalfLife
2	5 ICCS160614 N4 2inf N...M		= 45.68	11.98	0.07583	9.141
3	6 ICCS160614 N4 1inf N...M		= 48.07	15.23	0.057	12.16
4	7 ICCS160614 A2inf N4...Mu		= 46.3	12.78	0.0648	10.7
5	8 ICCS160614 A2inf A2...Mu		= 49.4	15.74	0.02901	23.89
6	9 ICCS160614 Y3inf N4...Mu		= 36.38	10.92	0.1079	6.422
7	10 ICCS160614 Y3inf Y...M		= 33.47	11.55	0.06318	10.97
8	11 ICCS160614 Q4inf Q...M		= 39.62	13.52	0.03256	21.29
9	12 ICCS160614 N4 1inf ...		= 42.77	16.28	0.05171	13.41
10	13 ICCS160614 N4 2inf ...		= 39.51	12.27	0.06941	9.986
11	14 ICCS160614 A2inf N...M		= 40.91	13.13	0.0377	18.39
12	15 ICCS160614 A2inf A...M		= 44.58	15.17	0.02111	32.84
13	16 ICCS160614 Y3inf N...M		= 34.48	11.68	0.04576	15.15
14	17 ICCS160614 Y3inf Y...M		= 30.84	12.34	0.05969	11.61
15	18 ICCS160614 Q4inf Q...M		= 37.79	14.36	0.02401	28.87

Figure 5-6. Workflow of TCR-ligand k_{off}-rate using 'Single Cell FlowJo Analysis'. A: User interface of the software after loading files exported from FlowJo. Files can be loaded by clicking 'Browse…'. The

application automatically graphs the dissociation data and identifies a timepoint at which the addition of d-biotin becomes apparent (red line). The user can analyze the samples by clicking 'Calculate Off-rate'. This prompts the calculation settings (B). **B**: Calculation settings. The user can choose to analyze all loaded files at once, the fitting model (unconstrained vs. constrained with the initial MFI as Y0), whether they want to save .jpg files of the resulting graphs, and whether they want to create Prism-conform .txt files of the data. **C**: View of the Prism result file created by the application. **D**: View of the .txt result file tabulating all fitting results, as created by the application.

5.3 Global k_{off}-rate as a parameter to merge subclonal avidities

The aim of the measurements of polyclonal populations was to acquire a TCR-ligand k_{off}-rate which reflected an average across the entire antigen-specific $CD8^+$ T-cell population, a parameter thereafter called 'global k_{off}-rate'.

It was uncertain whether the 'one-phase exponential decay' model used to analyze monoclonal dissociations could accurately reflect the avidity of polyclonal dissociations with many different kinetics. Therefore, it was important to elucidate how subclonal avidities merge into the global k_{off}-rate, whether different avidity levels would influence it to different extents, and how the frequencies of the subclonal populations affect it. Moreover, previously described phenomena like pMHC-rebinding and binding competition between T cells of different avidity (Martin-Blanco et al. 2018) during acquisition might confound global k_{off}-rates and needed to be investigated.

5.3.1 Combining monoclonal TCR-ligand k_{off}-rates from a murine TCR library for H-2K^b/OVA$_{257–264}$ in silico

To address the abovementioned questions in a setting that eliminates the possibility of such confounders, monoclonal dissociations were combined in silico. To do so, a previously established murine TCR library for H-2K^b/OVA$_{257–264}$ with diverse k_{off}-rates was used (**Figure 5-7**A) (Schober et al. 2020b). All TCR-ligand k_{off}-rates assays in this section 4.3 were performed by Sebastian Jarosch and Anna Purcarea.

Two dissociations of similar size (*i.e.*, f_{TCR16} = 0.416 and $f_{TCR16\text{-}30}$ = 0.584, where f_{TCR16} + $f_{TCR16\text{-}30}$ = 1), but rather different $t_{1/2}$, were selected and overlayed by concatenating their .fcs files using the FlowJo concatenate function (**Figure 5-7**B, C). This post-acquisition merging of the data simulated a dissociation of a biclonal T-cell population consisting of two clones of different avidity. The abovementioned 'one-phase exponential decay' model was fitted to this data as it had been done to the infection-induced polyclonal OVA-specific murine T-cell populations. Noticeably, the fitted curve ran between the two dissociation kinetics and had a $t_{1/2}$ almost identical to their arithmetic mean (**Figure 5-7**C). Formalizing this finding into a model equation, the 'global half-life' $t_{1/2_g}$ of the biclonal population was approximated by the arithmetic mean of the $t_{1/2}$ of the original dissociations a and b weighted by their frequency f within the resulting biclonal dissociation:

4.1. $$t_{1/2_g} \approx f_a * t_{1/2_a} + f_b * t_{1/2_b}$$

where

4.2. $$f_a + f_b = 1$$

To test whether this model was generalizable, all dissociations detailed in **Figure 5-7**A and **Figure 5-7**B were overlayed in the same manner as in **Figure 5-7**C and 'one-phase exponential decay' models fitted to them. The resulting $t_{1/2_g}$ correlated well with the arithmetic means of the $t_{1/2}$ of the two constituent dissociations (**Figure 5-7**D) corroborating the model equations.

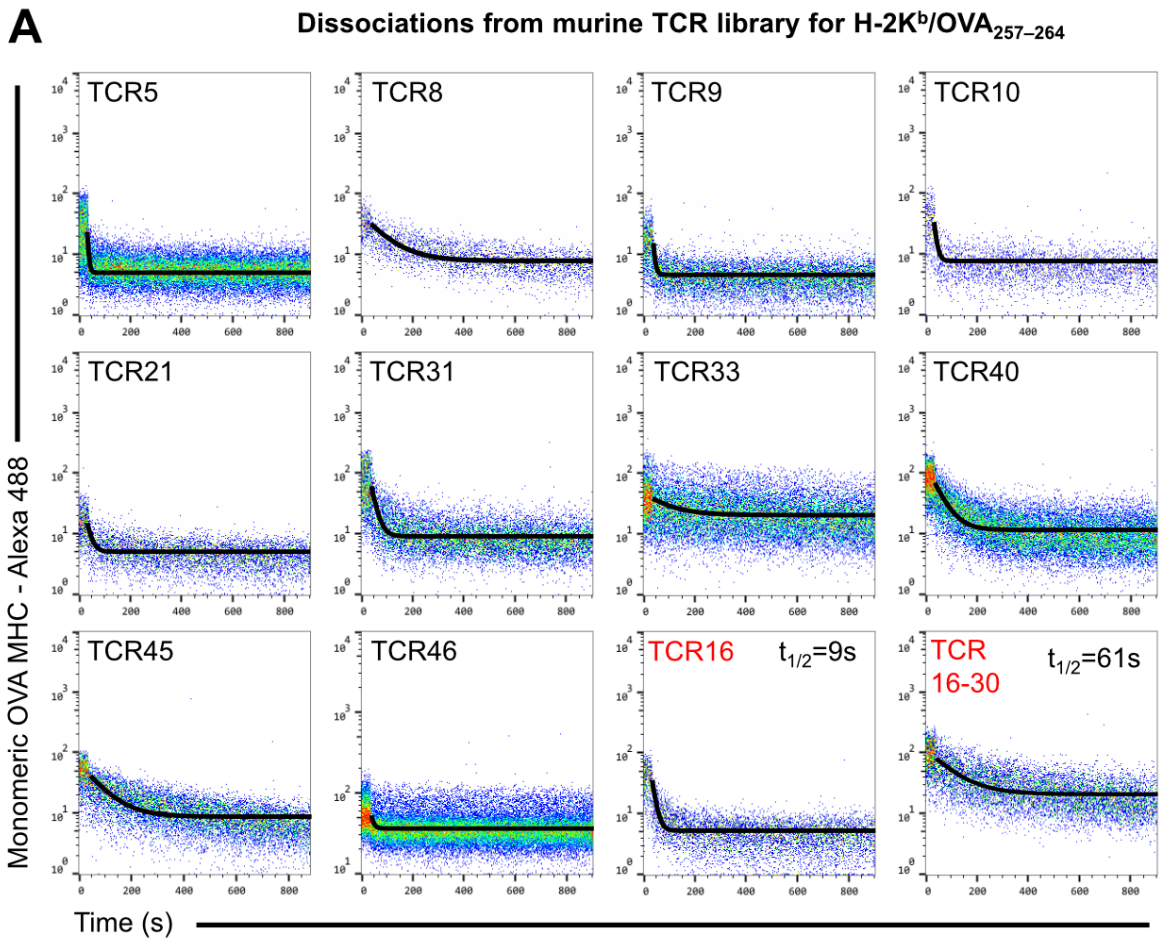

B

TCR clone	$t_{1/2}$ (s)	events
28	4	1216
8	60	3855
10	6	4030
21	11	6826
16	9	7504
16-30	61	10538
45	51	12617
9	4	12980
31	13	14414
33	61	22491
40	29	25829
5	3	35495
46	6	48620

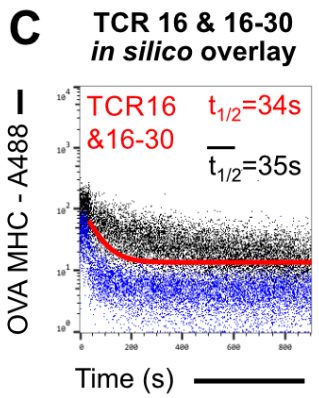

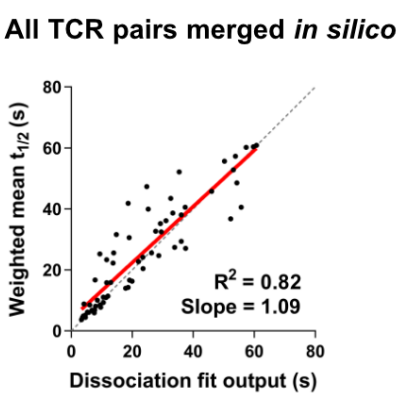

Figure 5-7. Murine global k_{off}-rates merging subclonal avidities in silico. A: Representative monomeric OVA MHC dissociations from a TCR library of murine T cells retrogenically expressing TCRs specific for H-2K^b/OVA$_{257–264}$. The TCR library is described in detail in (Schober et al. 2020b). TCR-ligand k_{off}-rates assays were performed by Sebastian Jarosch. **B:** Detailed overview of $t_{1/2}$ and size of the OVA MHC dissociations shown in (**A**) and used in (**C, D**). **C:** Overlay and exponential decay fit of the dissociations of two TCRs from separate measurements merged in silico. The $t_{1/2}$ obtained from the fit is shown in red while the mathematical average $t_{1/2}$ is shown in black. **D:** All possible pairs of the shown dissociations of the TCRs were formed and merged in silico. Exponential decays were fitted to those merged dissociations and correlated with the weighted mean of their measured $t_{1/2}$. Red solid lines represent linear regressions. Grey dashed line is a graph of f(x) = x. (**A, C, D**) adapted from (Lückemeier et al. 2022).

5.3.2 Predicting global k_{off}-rates of biclonal T-cell populations in silico from MFI-corrected, size-weighted dissociation parameters

Expanding on this finding, a more intricate formula predicting the $t_{1/2_g}$ was to be devised which considers all parameters of the 'one-phase exponential decay' model of GraphPad Prism. This 'one-phase exponential decay' model is specified as follows:

4.3. $$Y(t) = (S - E) * \left(\frac{1}{2}\right)^{\frac{t}{t_{1/2}}} + E$$

Where t is the time, $t_{1/2}$ is the dissociation half-life, S is the MFI of the pMHC at the start of the dissociation, and E is the MFI at the end of the dissociation.

First, in analogy to 4.1., to predict the dissociation curve $Y(t)_g$ of a biclonal T-cell population, the curves of the two constituent clones a and b were weighted by their frequency f and added together to form a new curve $Y(t)_n$:

4.4. $$Y(t)_g \sim Y(t)_n = f_a * Y(t)_a + f_b * Y(t)_b$$

Expanding the term on the left then gives:

4.5. $$Y(t)_g = \left(S_g - E_g\right) * \left(\frac{1}{2}\right)^{\frac{t}{t_{1/2g}}} + E_g$$

Which is approximated (∼) by the expanded term on the right:

4.6. $$Y(t)_n = f_a * \left[(S_a - E_a) * \left(\frac{1}{2}\right)^{\frac{t}{t_{1/2a}}} + E_a\right] + f_b * \left[(S_b - E_b) * \left(\frac{1}{2}\right)^{\frac{t}{t_{1/2b}}} + E_b\right]$$

When all the parameters of two constituent clones a and b were fed into 4.6. and a 'one-phase exponential decay' model was fitted to the resulting curve $Y(t)_n$, the $t_{1/2}$ this process yielded predicted the global $t_{1/2}$ of the overlayed biclonal dissociation of these clones even better than the equation in 4.1. (**Figure 5-8**). Therefore, the equations in 4.4. to 4.6. represented the size-weighted arithmetic mean of the $t_{1/2}$ of the two dissociations with a correction for differences in their MFIs.

The predictability of the global $t_{1/2}$ from the parameters of the constituent clones suggested that the 'one-phase exponential decay' model was suitable to assess the TCR structural avidity of polyclonal dissociations. Moreover, it showed that the global $t_{1/2}$ linearly merges subclonal avidities with high fidelity and without a bias for high, medium, or low subclonal avidity (**Figure 5-8**).

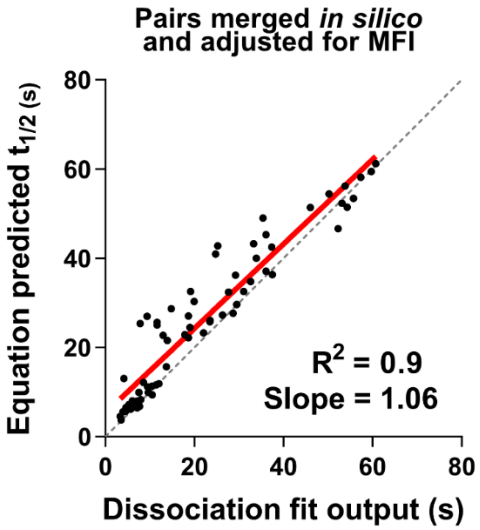

Figure 5-8. MFI-corrected, size-weighted means predicting global k_{off}-rates of biclonal T-cell populations in silico: All possible pairs of the dissociations shown in **Figure 5-7** were formed and merged in silico. 'One-phase exponential decay' curves were fitted to those merged dissociations and the resulting global $t_{1/2}$ correlated with the $t_{1/2}$ predicted by equations 4.4. to 4.6. Red solid lines represent linear regressions. Grey dashed lines are graphs of f(x) = x. Adapted from (Lückemeier et al. 2022).

5.3.3 Predicting global k_{off}-rates of biclonal T-cell populations from subclonal parameters ex vivo

To test whether this in silico finding also holds true for ex vivo biclonal T-cell populations, a subset of the TCRs from the TCR library for H-2K^b/OVA$_{257-264}$ were retrogenically expressed in mice with distinct congenic markers (CD90.1/CD90.2 or CD45.1/CD45.2) to distinguish them even when pooled in one sample. Two T-cell populations at a time expressing distinct TCRs were stained for TCR-ligand k_{off}-rates assays as previously described but were also stained for congenic markers during surface antigen staining. Both samples were subsequently pooled and their H-2K^b/OVA$_{257-264}$-TCR k_{off}-rates were measured (**Figure 5-9**A). Firstly, the global $t_{1/2}$ of the biclonal population was determined with standard gating and analysis. Next, a gate was placed on the stained congenic markers to isolate the dissociation kinetics of the two monoclonal T-cell populations and determine their $t_{1/2}$ separately (**Figure 5-9**A). The monoclonal dissociations in the pooled sample of TCR16-30 and TCR31 exhibited similar sizes and start/end MFIs and the arithmetic mean of the $t_{1/2}$ was close to the global $t_{1/2}$ of the biclonal dissociation (**Figure 5-9**A), similar to the in silico overlay experiments (**Figure 5-7**C).

To further corroborate the in-silico results, a total of 15 dissociations of paired TCRs from the TCR library were acquired as described above. Here, too, the $t_{1/2}$ that were predicted by the more complex equations described in 4.4. to 4.6. from the parameters of the constituent clones overlapped strongly with the global $t_{1/2}$ measured from the biclonal dissociations (**Figure 5-9**B). The astonishing overlap exclude phenomena like pMHC-rebinding and binding competition between T cells of different avidity.

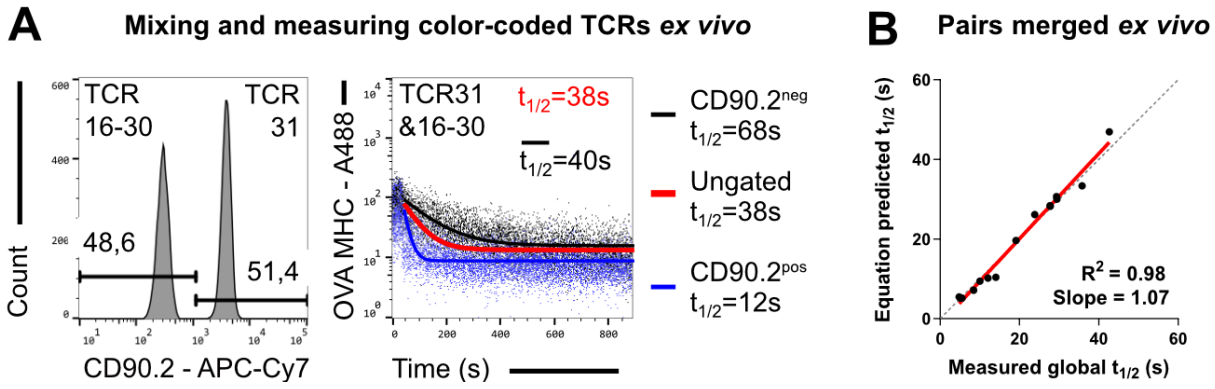

Figure 5-9. Mixing congenically marked retrogenic monoclonal T-cell populations and exploring global k_{off}-rates merging subclonal avidities ex vivo. A: Exemplary plots of color coding, pooling, and simultaneously measuring H-2K^b/OVA$_{257-264}$-TCR k_{off}-rates of two T-cell populations each retrogenically expressing one of the TCRs shown in **Figure 5-7**. The $t_{1/2}$ obtained from the fit is shown in red while the arithmetically average $t_{1/2}$ is shown in black. For color codes, T cells were either stained with antibodies against congenic markers or not. Dissociation data of the mixed and single dissociations were extracted by gates on the respective color code. **B**: Measured global $t_{1/2}$ of the dissociations of pairs of the TCRs shown in **Figure 5-7** were correlated to predictions of global $t_{1/2}$ made with the equations 4.4. to 4.6 using the parameters of the singular dissociations as input. n = 15 dissociations of TCR pairs from six independent experiments. Red solid lines represent linear regressions. Grey dashed lines are graphs of f(x) = x. Adapted from (Lückemeier et al. 2022).

These findings suggest that the global $t_{1/2}$ reflect an average measure of avidity across the entire measurable antigen-specific CD8$^+$ T-cell population by merging subclonal avidities in a linear and unbiased manner.

5.4 Induction, characterization, and avidity of OVA-APL-specific murine polyclonal CD8$^+$ T-cell populations

To study whether differences in global k_{off}-rates could predict differences in functionality, a model which could robustly induce polyclonal antigen-specific CD8$^+$ T-cell populations with tiered global k_{off}-rates towards a model epitope was needed.

Altered peptide ligands (APL) are peptides with a small substitute in the amino acid sequence compared to the original peptide ligand. Here, particular APLs of the OT-1-TCR ligand SIINFEKL (OVA$_{257-264}$, thereafter called 'OVA') were used to try to induce T-cell populations with cross-reactivity, but lower avidity towards OVA.

The following experiments aim at establishing OVA and its APLs as model epitopes for studying differences in avidity.

5.4.1 Induction and staining of APL-specific CD8$^+$ T-cell populations

The altered peptide ligands of SIINFEKL, SAINFEKL (A2), SIYNFEKL (Y3), and SIIQFEKL (Q4) were shown to be able to stimulate OT-1 T cells in decreasing order (from left to right) (Zehn et al. 2009). Because of this ability, the hypothesis was formulated that in immune responses, these APLs would select for TCRs which would also recognize the very similar SIINFEKL peptide, but with a lower structural avidity than an infection involving SIINFEKL itself would.

To accurately detect and characterize APL-specific T cells, a biotinylated and a strep-tagged recombinant peptide:MHC protein per APL was generated and used for multimer stainings and k_{off}-rate assays.

In order to induce antigen-specific T-cell populations, 6-8-week-old female C57BL/6 mice were infected with *L.m.* recombinantly expressing OVA or an APL. Mice were sacrificed on d8 p.i.

and splenocytes were stained with a non-reversible OVA or APL multimer, respectively, as well as CD8, CD44, and CD19 mAbs. CD44 was added as an activation marker to ensure that multimer$^+$ cells represented mostly infection-induced T-cell populations. Indeed, virtually all multimer$^+$ events were CD44^{hi} (**Figure 5-10**A). All APLs were immunogenic and robustly induced T-cell populations large enough to stain a sizable portion of the CD8$^+$ cells (**Figure 5-10**B).

Although the *L.m.* APL infections induced populations with significantly different frequencies of cognate multimer$^+$ cells, all were consistently detectable (**Figure 5-10**B). Thus, the newly generated APL MHC reagents were able to robustly detect antigen-specific CD8$^+$ T-cell populations induced by *L.m.* APL infections with frequencies similar to or higher than *L.m.* OVA-induced populations.

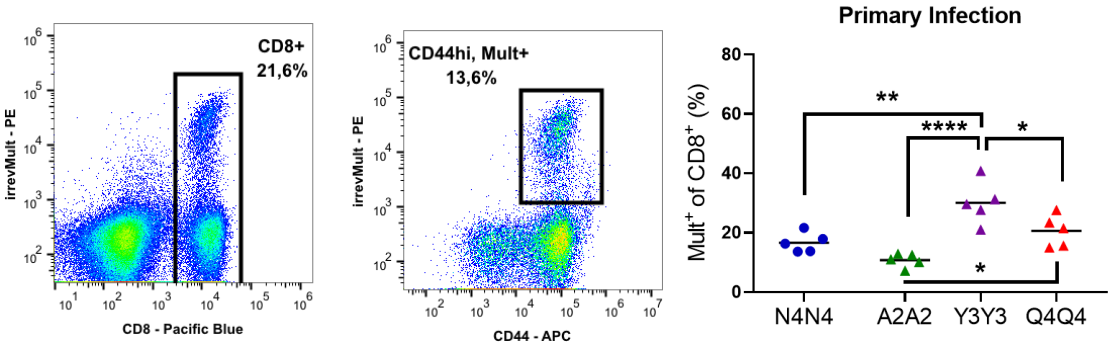

Figure 5-10. Frequency of non-reversible multimer$^+$ cells of CD8$^+$ cells after infection with *L.m.* strains. A: Gating strategy for quantification of APL irrevMult$^+$ cells. Representative graph of APL irrevMult$^+$ cells (*L.m.* A2-induced and stained with A2 MHC, abbreviated 'A2A2'). Splenocytes were stained with CD8, CD19 (DUMP channel) and CD44 mAb, and biotinylated H-2K^b/APL pMHC-Streptavidin multimers (irreversible multimers). The purity of CD44^{hi} events among irreversible multimer$^+$ events regularly exceeded 95%. **B**: Frequencies of cognate APL Mult$^+$ cells of CD8$^+$ cells. OVA MHC-stained samples of *L.m.* OVA-induced populations are shown for comparison. Each dot represents a mouse. n = 5 per group from 3 independent experiments. Bars indicate means. Ordinary one-way ANOVA followed by Tukey test were performed on all groups. p-values: * < 0.05, ** < 0.01, **** < 0.0001. All other comparisons were not significant.

5.4.2 Cognate pMHC-TCR dissociations of CD8$^+$ T cells after *L.m.* APL infection

After the establishment of the infection model, the next step was to measure the TCR-ligand k_{off}-rates of the induced populations. Structural avidity towards the inducing APL was assessed first.

Splenocytes of *L.m.* OVA or *L.m.* APL infected mice were stained with a reversible and an irreversible cognate pMHC multimer, as well as CD8α and CD19 mAbs, resulting in double-multimer staining of cognate antigen-specific, CD8$^+$ T cells. (**Figure 5-11**, leftmost 3 columns). TCR-ligand k_{off}-rate assays could robustly be performed on all *L.m.*-induced populations, showing that all refolded pMHC reagents were robustly able to produce distinct double multimer stainings with rapid backbone dissociations and pMHC kinetics following the addition of d-biotin (**Figure 5-11**, rightmost 2 columns).

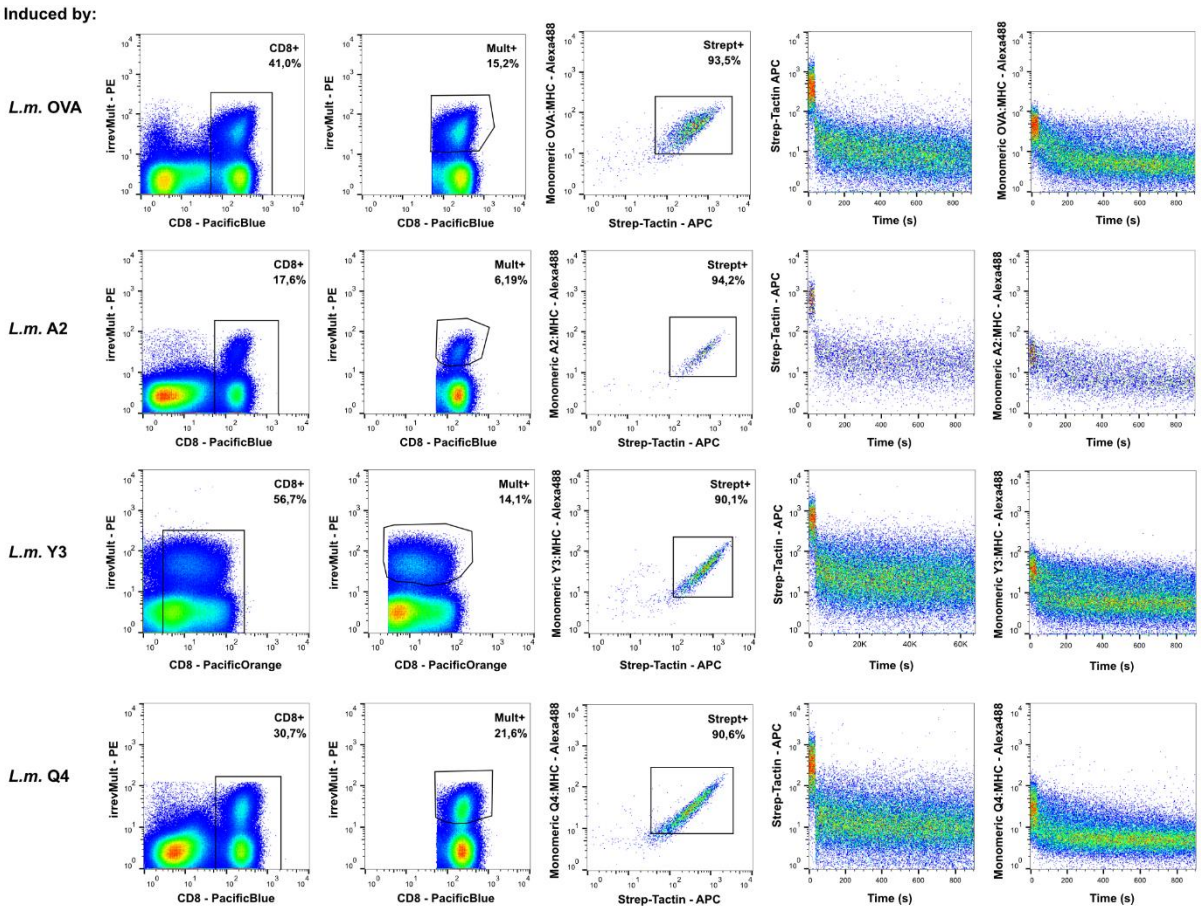

Figure 5-11. APL MHC-TCR dissociation kinetics of *L.m.* APL-induced T-cell populations ex vivo with newly generated APL MHC staining reagents. Representative pMHC-TCR dissociation experiments with cognate pMHC double multimer staining on d8 p.i. To acquire the dissociation plots on the right, a gate was kept on CD8$^+$, irreversible Multimer$^+$ events. In the plots in the middle, only the events acquired before the addition of d-biotin are depicted (by gating on the first 30s) to evaluate the frequency of double multimer$^+$ events. Gated on living CD19$^-$ lymphocytes. The inducing Listeria strain is indicated row-wise left of the panels.

Interestingly, the average global k_{off}-rates of the *L.m.* APL-induced T-cell populations did not differ significantly from that of the *L.m.* OVA-induced populations when measured with their cognate pMHC reagents (**Figure 5-12**), implying that the global structural avidity of these populations towards their cognate epitope was similar.

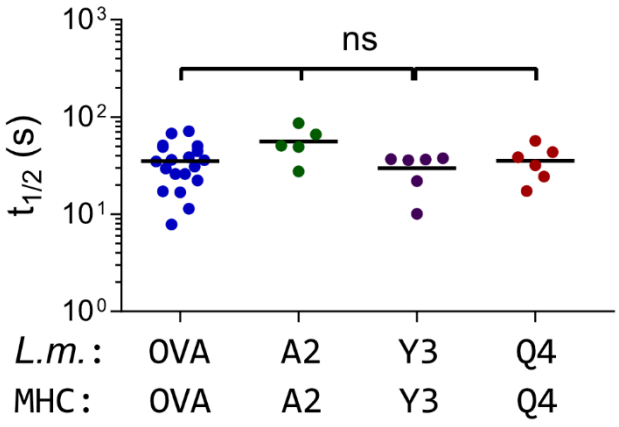

Figure 5-12. Summary of cognate pMHC-TCR k_{off}-rate measurements on d8 p.i. The inducing *Listeria* strain is indicated in the upper, and the pMHC used for pMHC-TCR k_{off}-rate measurements in the lower row. n = 5–19 from >10 independent experiments. Each dot represents a mouse. Bars indicate

means. Ordinary one-way ANOVAs followed by Tukey tests were performed. ns, not significant. Adapted from (Lückemeier et al. 2022).

5.4.3 TCR - OVA MHC k_{off}-rates of *L.m.* APL-induced CD8$^+$ T-cell populations

The next step was to assess whether the APLs would indeed select for TCRs which would also recognize the OVA epitope and whether they would exhibit a lower avidity towards OVA compared to those of *L.m.* OVA-induced populations. To test this, the *L.m.* APL-induced CD8$^+$ T-cell populations were subjected to TCR - OVA MHC k_{off}-rates.

Samples were prepared and TCR-ligand k_{off}-rate assays were performed as described above, but this time exclusively with OVA MHC reagents for all samples.

Dissociation kinetics could be acquired in all infection settings, with the notable exception of *L.m.* Q4-induced populations, which exhibited H-2K^b/OVA$_{257-264}$-TCR dissociations at such low frequencies and so fast that an accurate measurement of the global k_{off}-rate was not possible (**Figure 5-13**A). Global $t_{1/2}$ values of the *L.m.* A2-induced populations were very similar to those of *L.m.* OVA-induced populations, but those of *L.m.* Y3-induced populations were significantly lower (**Figure 5-13**B). Remarkably, the average global $t_{1/2}$ of the *L.m.* APL-induced T-cell populations was robustly tiered by the inducing APL, reminiscent of the APL's ability to stimulate the OT-1 TCR (**Figure 5-13**B).

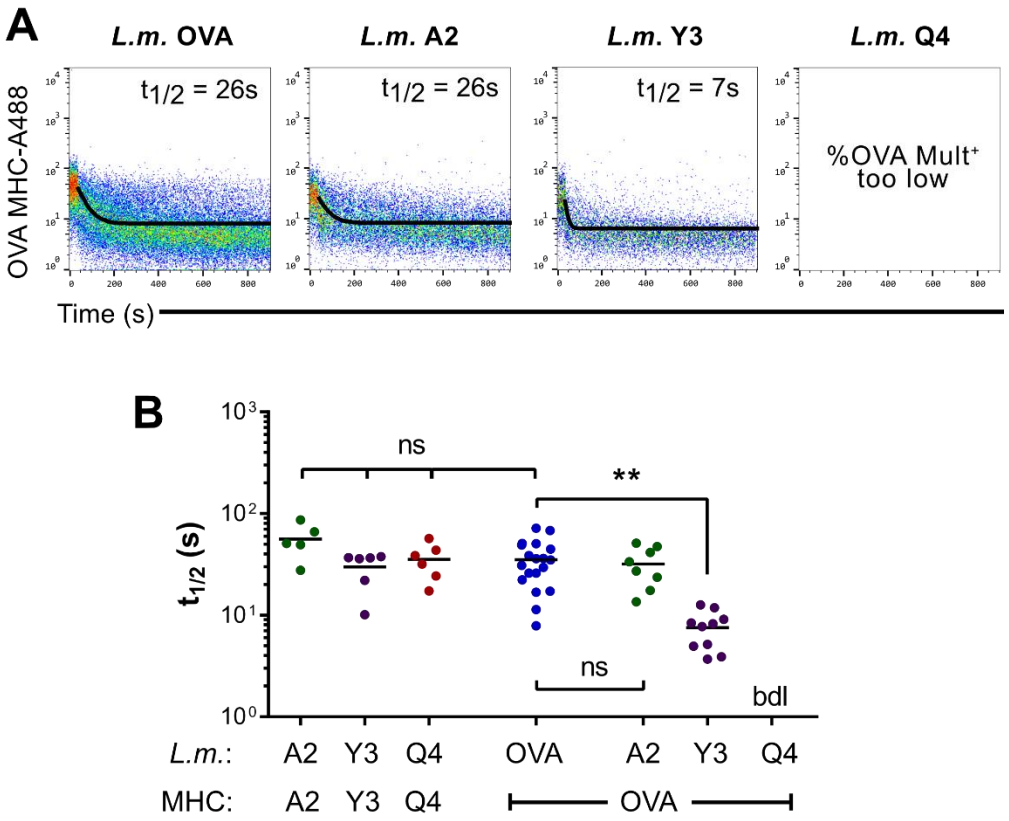

Figure 5-13. OVA MHC-TCR k_{off}-rates of *L.m.* APL-induced T-cell populations ex vivo. A: Representative H-2K^b/OVA$_{257-264}$ - TCR k_{off}-rate measurements on d8 p.i. The inducing *Listeria* strain is indicated column-wise above the panels. Gated on living, CD19$^-$, CD8$^+$, irrevMult$^+$ lymphocytes. *L.m.* Q4 infections induced T-cell populations with insufficient frequencies of H-2K^b/OVA$_{257-264}$ multimer-binding cells. **B**: Summary of pMHC-TCR k_{off}-rate measurements on d8 p.i. The $t_{1/2}$ from cognate pMHC-TCR k_{off}-rate assays summarized in **Figure 5-12** are displayed on the left for comparison. The inducing *Listeria* strain is indicated in the upper, and the pMHC used for pMHC-TCR k_{off}-rate measurements in the lower row. n = 5–19 from >10 independent experiments. Each dot represents a mouse. Bars indicate means. Ordinary one-way ANOVAs followed by Tukey tests were performed on the leftmost and

rightmost four groups of each graph. **p-value < 0.01. ns, not significant; bdl, below detection limit. Adapted from (Lückemeier et al. 2022).

5.4.4 TCR-ligand k_{off}-rates after homologous secondary infection

To test the changes in structural avidity in a recall infection setting, a secondary *L.m.* infection was performed. Mice were infected with the same *L.m.* strain used in the primary infection after at least 4 weeks of convalescence. On day 6 after infection, mice were sacrificed and splenocytes were prepared and stained as described above.

pMHC-TCR dissociation kinetics could be acquired for all infection/pMHC settings, except for *L.m.* Q4-induced populations which still did not exhibit high enough frequencies of OVA MHC-binding cells upon secondary infection to acquire accurate global $t_{1/2}$ (**Figure 5-14**A).

The average global $t_{1/2}$ of the recall populations followed a similar pattern as the populations on day 8 post infection with cognate pMHC-TCR dissociations not differing significantly between groups while the tiered order of the average global $t_{1/2}$ of OVA MHC-TCR dissociations was preserved (**Figure 5-14**B).

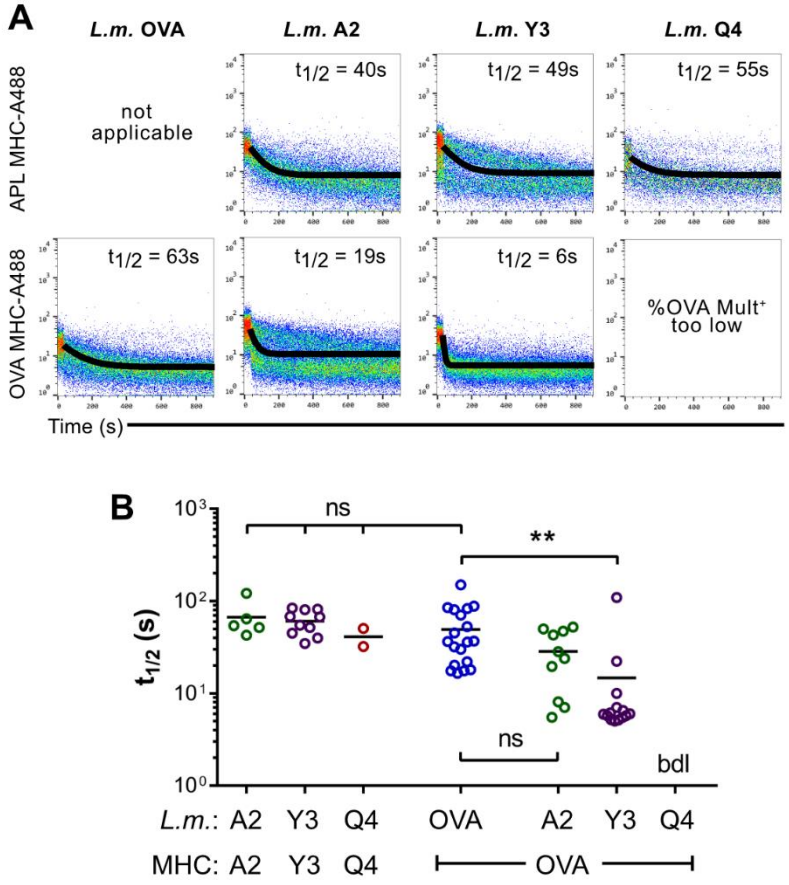

Figure 5-14. TCR-ligand k_{off}-rates after homologous secondary infection. A: Representative pMHC-TCR k_{off}-rate measurements with cognate H-2K^b/APL (upper rows) or with H-2K^b/OVA$_{257-264}$ (lower rows) on d6 after homologous secondary infection. The inducing *Listeria* strain is indicated column-wise above the panels. Gated on living, CD19$^-$, CD8$^+$, irrevMult$^+$ lymphocytes. *L.m*. Q4 infections induced T-cell populations with insufficient frequencies of H-2K^b/OVA$_{257-264}$ multimer-binding cells. **B**: Summary of pMHC-TCR k_{off}-rate measurements on d6 after recall infection. The inducing *Listeria* strain is indicated in the upper, and the pMHC used for pMHC-TCR k_{off}-rate measurements in the lower row. n = 2–19 from >10 independent experiments. Each dot represents a mouse. Bars indicate means. Ordinary one-way ANOVAs followed by Tukey tests were performed on the leftmost and rightmost three groups of the graph. **p-value < 0.01. ns, not significant; bdl, below detection limit. Adapted from (Lückemeier et al. 2022).

Like the *L.m.* OVA-induced populations, *L.m.* APL-induced T-cell populations exhibited a slight but mostly non-significant increase in average global $t_{1/2}$ towards the cognate epitope from primary to secondary infection, akin to 'avidity maturation' (Busch und Pamer 1999; Savage et al. 1999) (**Figure 5-15**).

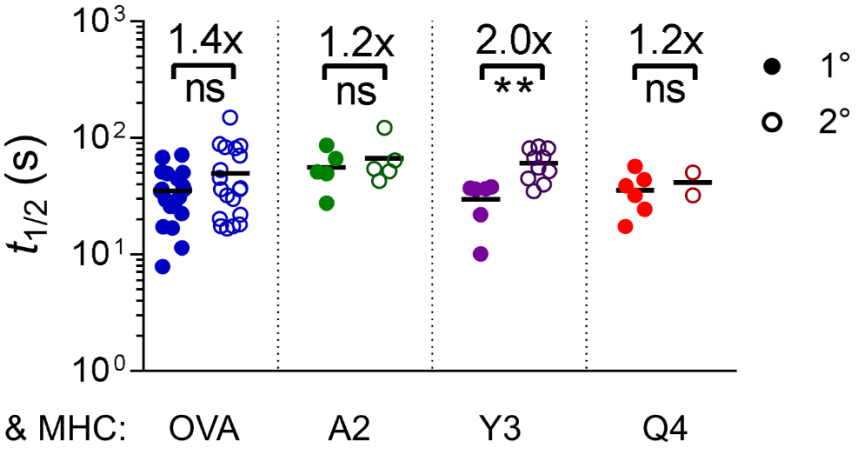

Figure 5-15. Global $t_{1/2}$ towards cognate epitope of *L.m.*-induced populations after primary vs. secondary infections. A: Summary of pMHC-TCR k_{off}-rate measurements on d8 p.i. (1°) and 6 days after recall infection (2°). The inducing Listeria strain and pMHC used for pMHC-TCR k_{off}-rate measurements are indicated below. n = 2-19 from >10 independent experiments. Each dot represents a mouse. Bars indicate means. Fold changes are indicated. Multiple unpaired *t*-tests were performed on the respective 1° vs. 2° groups. ** = *p*-value < 0.01. ns, not significant. Adapted from (Lückemeier et al. 2022).

5.4.5 Binding of OVA multimer vs. cognate multimer in *L.m.* APL-induced CD8$^+$ T-cell populations

To further investigate the OVA multimer-binding subpopulation of the *L.m.* APL-induced populations, frequencies of OVA Mult$^+$ vs. cognate Mult$^+$ cells were compared within these populations.

Samples were stained as described in 4.4.1, but this time exclusively with OVA MHC reagents. All *L.m.* APL-induced populations showed robustly measurable OVA Mult$^+$ subpopulations, which were almost exclusively CD44^{hi}, which indicated that they, too, were activated by the infection with the *L.m.* APL (**Figure 5-16**A).

To evaluate frequencies of cognate multimer vs. OVA multimer binding, *L.m.* APL-induced populations were split before staining, and one sample was stained with cognate multimer and the other stained with OVA multimer as described above. Frequencies of OVA Mult$^+$ cells of CD8$^+$ cells were generally lower than those of cognate APL Mult$^+$ cells of CD8$^+$ cells (**Figure 5-16**B). The variability of the ratio of frequencies of OVA Mult$^+$ cells over cognate APL Mult$^+$ cells was surprisingly low within the *L.m.* APL infection settings (**Figure 5-16**C) hinting at a robust induction of subpopulations with cross-reactivity towards OVA despite interindividual differences in the TCR repertoires between mice.

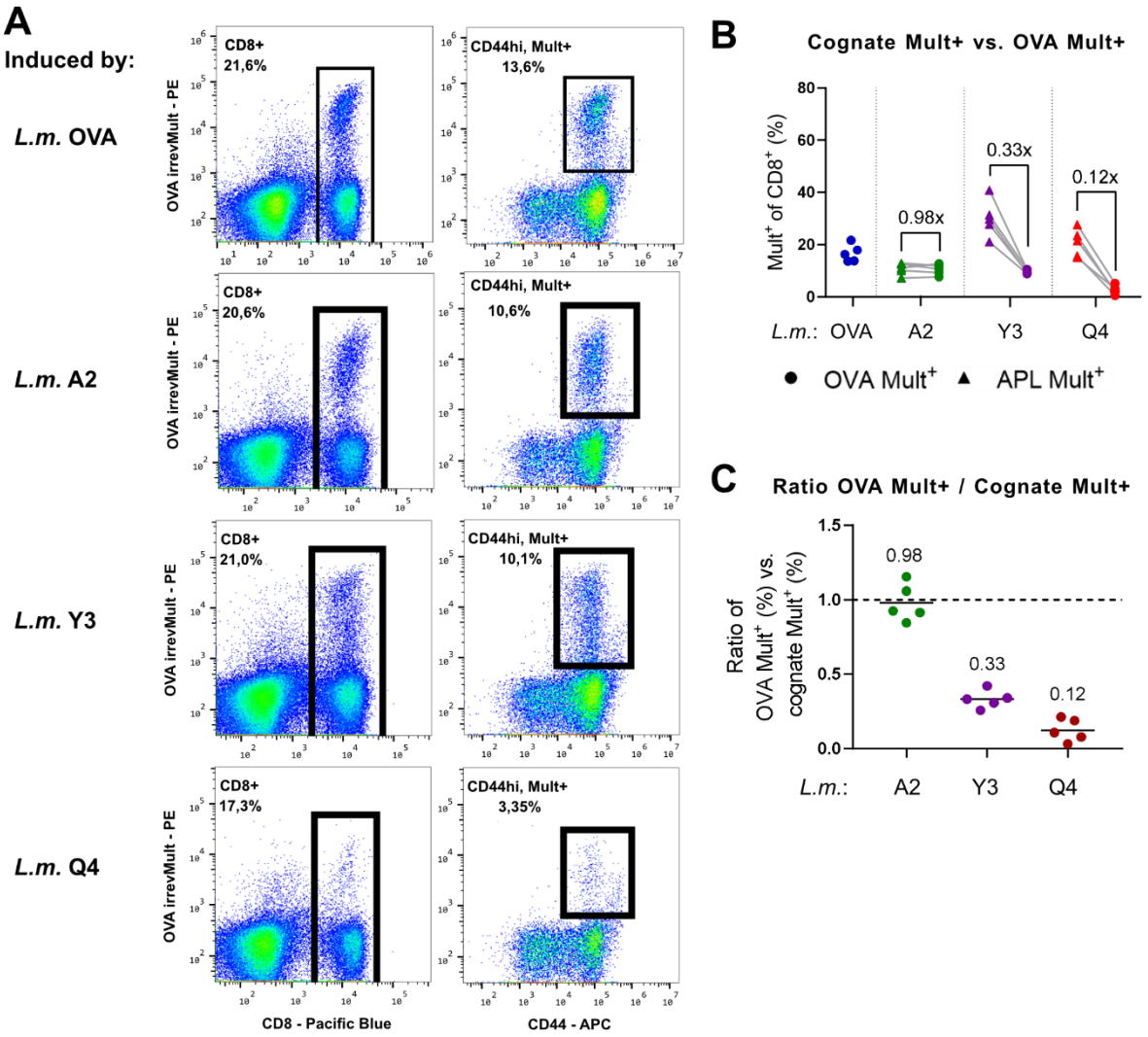

Figure 5-16. OVA multimer vs. cognate multimer binding of *L.m.* APL-induced CD8⁺ T-cell populations. A: Gating strategy for quantification of OVA Mult⁺ cells from each *L.m.* infection setting. Splenocytes were stained with CD8, CD19 (DUMP channel), and CD44 mAb, and biotinylated H-2K^{b}/OVA$_{257-264}$ - Streptavidin multimers (Mult). Gated on living CD19^{-} lymphocytes. The inducing Listeria strain is indicated row-wise left of the panels. The purity of CD44^{hi} events among Mult⁺ events regularly exceeded 95%. **B**: Frequencies of APL Mult⁺ (as described in **Figure 5-10**) vs. OVA Mult⁺ cells of CD8⁺ cells within the same populations. Splenocytes were split and stained with APL Mult or OVA Mult, respectively. *L.m.* OVA-induced populations are shown for comparison. Each dot represents a mouse. n = 5 per group from 3 independent experiments. Bars indicate means. **C**: Ratios of the percentages shown in (B). Bars indicate means. Mean ratios are indicated above. (**B, C**) adapted from (Lückemeier et al. 2022).

In recall populations, frequencies of Mult⁺ cells among CD8⁺ cells were markedly higher than those in the induced populations on day 8 p.i. in all infection/staining settings (compare **Figure 5-16**B and **Figure 5-17**A). *L.m.* Q4-induced recall populations were not included, because they did not exhibit high enough frequencies of OVA Mult⁺ cells for accurate quantification in preliminary stainings. The ratios of the means of OVA Mult⁺ and APL Mult⁺ frequencies within the *L.m.* group were slightly higher than on day 8 p.i., hinting at a higher rate of T cells cross-reactive towards the OVA epitope (compare **Figure 5-16**C and **Figure 5-17**B). Again, these ratios were very robust within APL groups (**Figure 5-17**B).

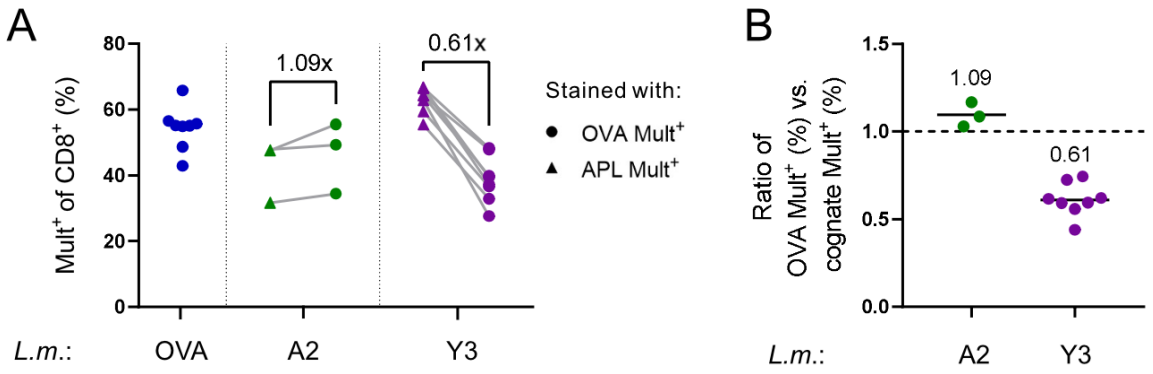

Figure 5-17. Cognate multimer and OVA multimer binding of *L.m.* APL-induced CD8⁺ T-cell populations after recall infection. A: Frequencies of OVA Mult⁺ vs. APL Mult⁺ of CD8⁺ within the same populations. Splenocytes were split and stained with CD8α mAb and APL multimer or OVA multimer, respectively, 6 days after recall infection with the *L.m.* strain indicated below. The ratio of the means of OVA Mult⁺ and APL Mult⁺ frequencies within each *L.m.* group is indicated above. Each dot represents a mouse. n = 2-8 from 6 independent experiments. *L.m.* OVA-induced populations are shown for comparison. **B**: Ratios of the percentages shown in (A). Bars indicate means. Mean ratios are indicated above. Adapted from (Lückemeier et al. 2022).

5.4.6 Cross-reactivity of *L.m.* APL-induced CD8⁺ T-cell populations

Further investigations into the cross-reactivity of *L.m.* APL-induced populations required a more complex experimental setup. While splitting and staining these populations with APL Mult or OVA Mult gave an impression of the sizes of the antigen-specific subpopulations, it did not prove that they overlap (*i.e.*, that they are cross-reactive). Double staining of the same sample with both multimers would likely not have yielded an accurate measure of the frequency of cross-reactive T cells, because the cognate multimer would presumably displace OVA multimers leading to a skewed assessment.

Thus, the *L.m.* APL-induced populations were first stained with a reversible cognate multimer, sorted for Mult⁺ cells, and restained with OVA multimers to quantify the frequency of T cells binding both multimers. Mice were sacrificed on day 8 p.i. and spleens were prepared as described above. After staining with reversible cognate multimer and CD8α and CD19 mAb, Mult⁺ and Mult^{neg} cells were sorted separately and treated with d-biotin to disrupt multimer staining to eliminate competition for TCR binding (**Figure 5-18**A). Samples were washed, stained with H-2K^{b}/OVA$_{257-264}$ - Streptavidin multimers, and read in. The frequency of OVA multimer-binding cells in the cognate Mult⁺-sorted group was similar to the ratios observed in **Figure 5-16**C in all APL groups (**Figure 5-18**B). Moreover, only a negligible percentage of the cognate Mult^{neg}-sorted cells bound the OVA multimer (**Figure 5-18**C), suggesting that almost no cells from this pool are part of the OVA multimer-binding subpopulation.

These data indicated that infections with *L.m.* APL-induced T-cell populations with robust cross-reactivity towards OVA and that the OVA multimer-binding subpopulations were almost exclusively cross-reactive.

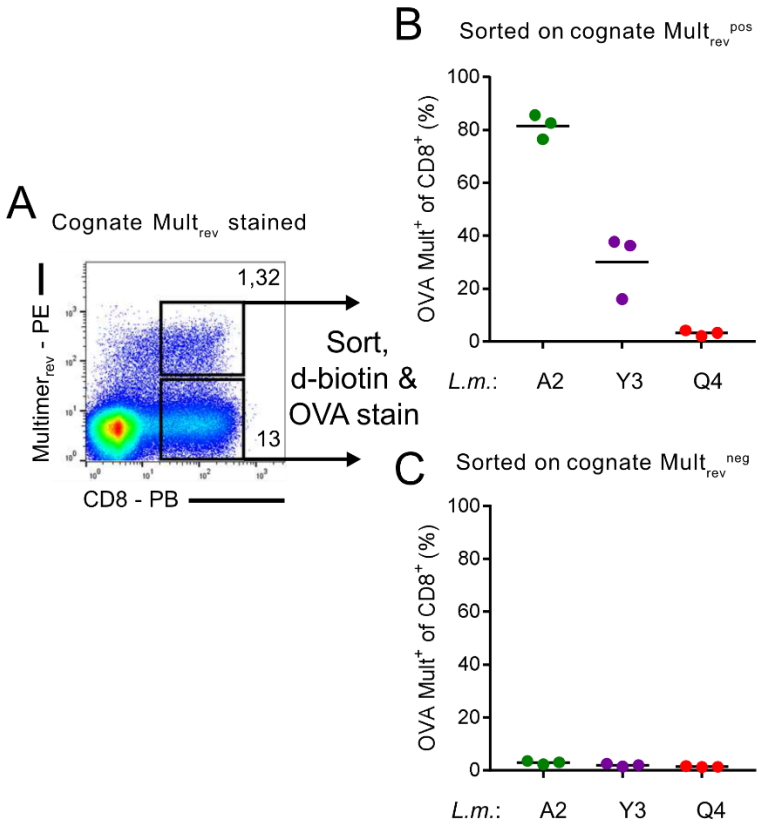

Figure 5-18. Cross-reactivity of *L.m.* APL-induced CD8$^+$ T-cell populations. A: Sorting scheme. 8 days p.i. with an *L.m.* APL strain, splenocytes were stained with CD8α mAb and cognate APL MHC reversible multimers. CD8$^+$, reversible Mult$^+$ (**B**), or reversible multimer^{neg} (**C**) were sorted, treated with d-biotin, washed, and restained with OVA multimer. Each dot represents a mouse. n = 3 per group from 1 experiment. Adapted from (Lückemeier et al. 2022).

5.4.7 Polyclonality of *L.m.* APL-induced, multimer-binding T-cell populations

Next, the polyclonality of the antigen-specific CD8$^+$ T-cell populations of the *L.m.* APL infection model was assessed.

TCR-Vβ-chain staining of cognate multimer and OVA multimer-binding CD8$^+$ cells was performed to evaluate their TRBV repertoires. Mice were sacrificed 8 days after primary infection or 6 days after recall infection, respectively, and spleens were prepared as described above. Splenocytes were split into 15 samples per mouse, stained with CD8α, CD19, and CD44, as well as 1 of 15 Vβ-chain antibodies, and stained with non-reversible cognate or OVA multimer, respectively. *L.m.* Q4-induced recall populations were not included, because they did not exhibit high enough frequencies of OVA Mult$^+$ cells.

TRBV frequencies were very heterogeneous between and within groups (**Figure 5-19**A, B). All groups showed TRBV frequencies without absolute majorities after primary infection whereas populations after secondary infection tended to have larger shares of a single TRBV class (**Figure 5-19**A, B). This was also reflected in the trend towards a lower Simpson index of diversity after secondary infection and is in line with the previously discussed ‘avidity maturation’ (Busch und Pamer 1999; Savage et al. 1999)(**Figure 5-19**B, C). However, all of the examined multimer-binding populations showed recruitment of multiple TRBV chains and none were deemed oligo- or even monoclonal.

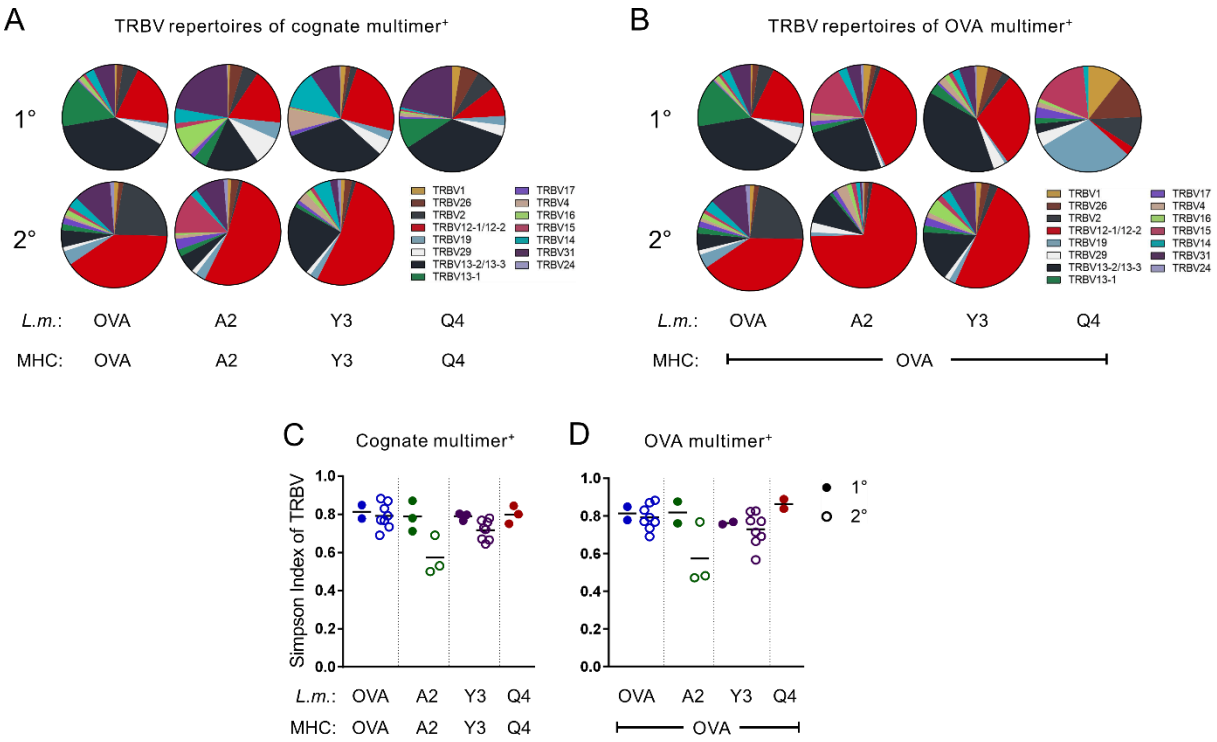

Figure 5-19. TRBV repertoires and diversity indices of *L.m.*-induced, OVA multimer and cognate multimer-binding T-cell populations. A, B: Representative TRBV repertoires of CD8⁺ cognate multimer⁺ (A) or OVA multimer⁺ (B) splenocytes 8 days p.i. (upper row) and 6 days after recall infection (lower row) with *L.m.* OVA or *L.m.* APL, as indicated below. Each pie chart shows the repertoire of one mouse. **C, D**: Simpson diversity index of TRBV repertoire stainings measured by flow cytometry showing polyclonality of CD8⁺ cognate multimer⁺ (C) or OVA multimer⁺ (D) splenocytes 8 days p.i. (1°) and 6 days after recall infection (2°). The inducing Listeria strain is indicated in the upper, and the MHC used for multimer staining in the lower row. n = 2-8 from 6 independent experiments. Adapted from (Lückemeier et al. 2022).

5.5 Correlation of functional avidity and global k_{off}-rates

The OVA/APL infection model established above could robustly induce polyclonal antigen-specific CD8⁺ T-cell populations with tiered avidity towards the OVA epitope. TCR avidity was shown to be associated with the functional avidity of T-cell populations (Allard et al. 2017; Nauerth et al. 2013; Hombrink et al. 2013).

Functional avidity is commonly described as a measure of peptide sensitivity. The dose at which the half-maximal T-cell effector function is reached is called EC_{50} and lends itself to comparing the mean functional avidity of both monoclonal and polyclonal T-cell populations.

The next set of experiments aimed to study whether global k_{off}-rates of polyclonal T-cell populations could predict differences in their functionality avidity towards OVA in vitro.

5.5.1 Peptide sensitivity towards APL and OVA antigen

To determine the functional avidity for the T-cell populations characterized in the previous section, mice were infected with *L.m.* OVA or *L.m.* APL and were sacrificed 8 days after primary infection or 6 days after recall infection, respectively. Spleens were prepared as described above and splenocytes split into 12 samples per spleen: 11 for peptide titration and 1 for parallel pMHC-TCR k_{off}-rate measurements. The latter were performed as previously described. For peptide titration, splenocytes were stimulated by adding increasing concentrations of SIINFEKL ('OVA') or an APL, respectively. Positive/negative controls were stimulated with PMA and Ionomycin or just medium, respectively. After the addition of peptide,

samples were placed in an incubator for 5h, while Golgi plug was added after 1h. Afterwards, cells were stained with CD8α, CD19, and IFN-γ mAbs and read in. The frequency of IFN-γ$^+$ among CD8$^+$ cells was detectable for all infection settings with all peptides used (**Figure 5-20**A, B). A log(agonist) vs. response model was fitted to these frequencies and the resulting logEC_{50} was reported as functional avidity (**Figure 5-20**C, D). The fitting of the sigmoidal curves was good in all experiments and the order of the frequencies of IFN-γ$^+$ of CD8$^+$ cells at the maximal dose was generally congruent with the order of the frequencies of Mult$^+$ of CD8$^+$ of all groups, speaking for the validity of the results (compare **Figure 5-20**C, D and **Figure 5-10**).

The resulting logEC_{50} values did not differ significantly between groups when they were stimulated with their cognate peptide (**Figure 5-20**E, F, left side). This indicated that all groups had a similar potential to react to peptide stimulation and that no *Listeria* strain induced CD8$^+$ T-cell populations with an inherently lower functional avidity. However, when the logEC_{50} values of peptide stimulation with the OVA peptide were compared, the groups showed the same tiering as observed with the global k_{off}-rates towards OVA (**Figure 5-20**E, F, right side. Compare to **Figure 5-13** and **Figure 5-14**).

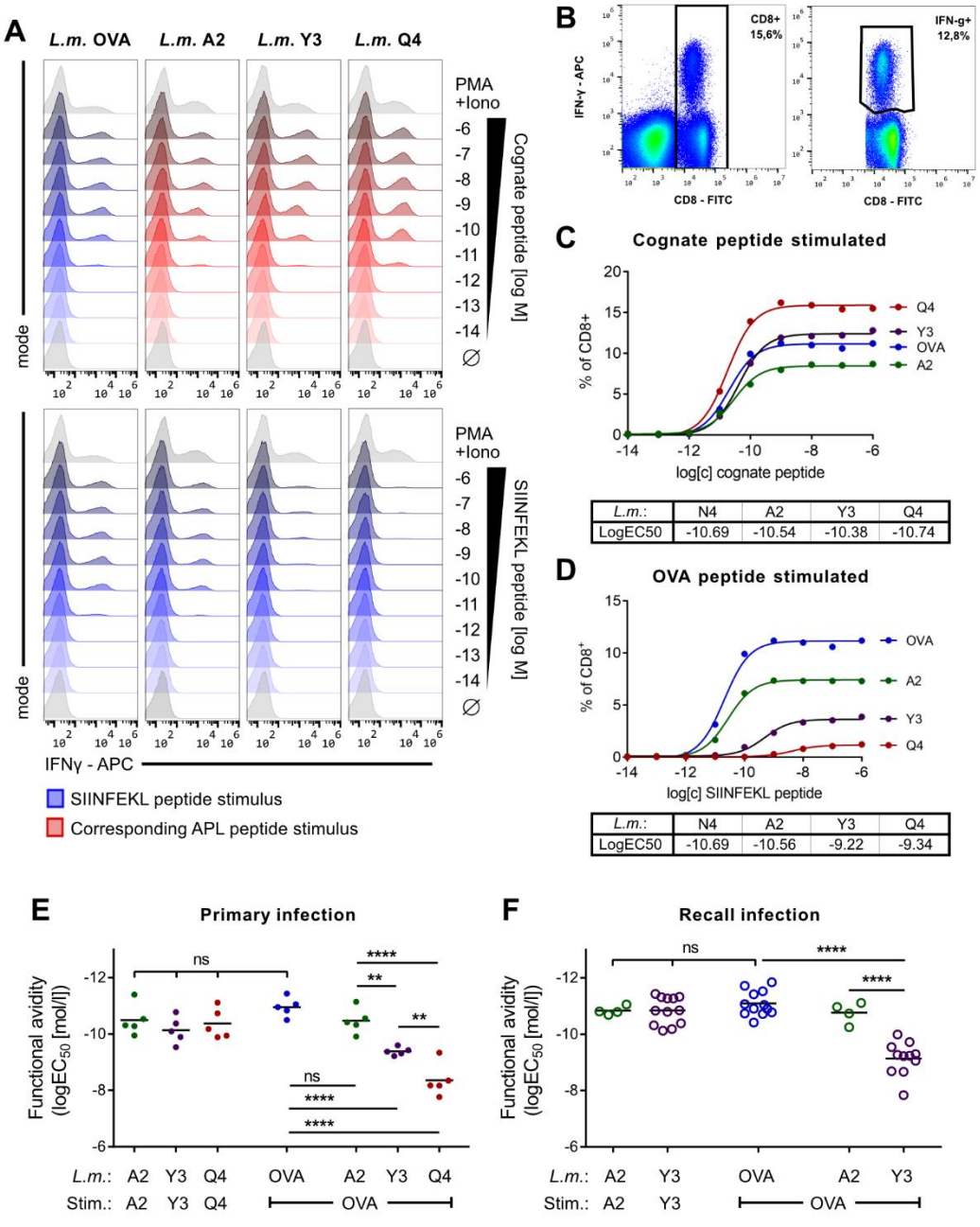

Figure 5-20. Peptide sensitivity to OVA or APL peptide of *L.m.*-induced CD8$^+$ populations in vitro. **A**: Representative plots of frequency of IFN-γ$^+$ among CD8$^+$ cells upon stimulation with increasing amounts of the corresponding APL (upper rows) or the SIINFEKL (lower rows) peptide, PMA + Ionomycin, or no peptide (Ø) on d8 p.i. The inducing *Listeria* strain is indicated column-wise above the panels. Samples of *L.m*. OVA-induced populations are shown in upper and lower rows for better comparison. **B**: Gating strategy for quantification of IFN-γ$^+$ among CD8$^+$ cells after peptide stimulation. Gated on living lymphocytes. **C, D**: Representative analysis of peptide titration of the samples shown in (A). Prism 7's log(agonist) vs. response model was fitted to the percentages of IFN-γ$^+$ of CD8$^+$ of increasing peptide dose samples and the resulting logEC_{50} was reported as functional avidity. **E, F**: Quantification of log EC_{50}s of IFN-γ release upon peptide stimulation (functional avidity) on d8 p.i. (E) or d6 after recall infection (F). The inducing *Listeria* strain is indicated in the upper, and the peptide used as the stimulus in the lower row. n = 4–12 from eight independent experiments. Each dot represents the spleen of a mouse. Bars indicate means. Ordinary one-way ANOVAs followed by Tukey tests were performed on the leftmost and rightmost four (E) or three (F) groups of each graph. *p*-values: ** < 0.01, **** < 0.0001. ns, not significant. (A, E, F) adapted from (Lückemeier et al. 2022).

5.5.2 Phenotypic composition of antigen-specific CD8$^+$ T-cell populations

The observed difference between groups in functional avidity seemed to be associated with their structural avidity towards the epitope. However, potential factors that could confound these differences -in particular the phenotypic composition of the populations- had to be excluded.

To do so, mice were infected with *L.m.* OVA or *L.m.* APL and were sacrificed 8 days after primary infection or 6 days after recall infection, respectively. Splenocytes were prepared as described previously and surface antigen staining was performed with CD8α, CD19, CD44, CD62L, and CD27 mAbs. Samples were then split and either stained with OVA multimer or their cognate APL multimer, respectively. The phenotypic composition of CD8$^+$, Mult$^+$, and CD44^{hi} cells was determined by the expression of CD62L and CD27. Subsets were defined as follows: Effector T cells (T_{EC}) CD62L$^-$, CD27$^-$; Effector memory T cells (T_{EM}) CD62L$^-$, CD27$^+$; Central memory T cells (T_{CM}) CD62L$^+$, CD27$^+$ (**Figure 5-21**A).

The frequencies of the different T-cell subsets were quite robust within groups and very similar between groups in all infection settings (**Figure 5-21**B). Next, the frequencies of naïve T cells among the multimer-binding CD8$^+$ T cells were determined. Naïve T cells were defined as CD44^{lo}, CD62L$^+$ (**Figure 5-21**C). Naïve T cells made up only a small fraction in the low single-digit percentages of all multimer-binding CD8$^+$ T cells in all infection and staining settings. (**Figure 5-21**D, E).

Therefore, the differences in functional avidity observed between groups could not be explained by differences in their phenotypic compositions.

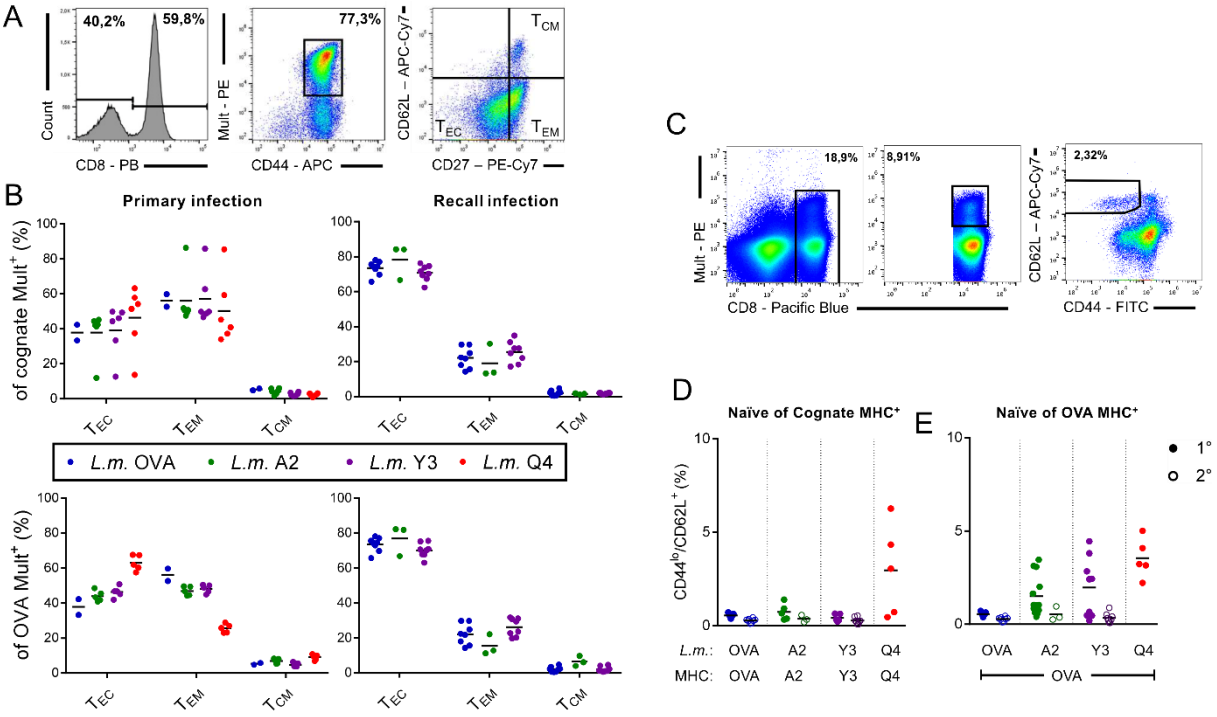

Figure 5-21. Phenotypic composition of multimer$^+$ CD8$^+$ T-cell populations after *Listeria* infection. **A**: Gating strategy to determine T-cell subset frequencies. Pregated on CD19$^-$ living lymphocytes. A recall population is shown. **B**: Summary of immunophenotyping of cognate multimer$^+$ (upper row) or OVA multimer$^+$ (lower row) populations either 8 days after primary infection (left column) or 6 days after recall infection (right column). n = 2-8 from 7 independent experiments **C**: Gating strategy to determine naïve T-cell frequencies. Pregated on CD19$^-$ living lymphocytes, in this case of a primary infection population **D, E**: Frequencies of naïve among MHC-binding T cells. The inducing Listeria strain is indicated in the upper, and the pMHC used for stainings in the lower row. n = 3-8 (D) or n = 3-13 (E) from 7 independent experiments. In all graphs, each dot represents a mouse. Bars indicate means. Adapted from (Lückemeier et al. 2022).

5.5.3 Correlation between functional avidity and global k_{off}-rates

To assess the link between functional avidity and global k_{off}-rates in more detail, the logEC_{50} values of the antigen-specific CD8$^+$ T-cell populations were plotted against their global k_{off}-rates which were acquired in parallel and with the corresponding epitope (*e.g.,* TCR-pMHC k_{off}-rate assay performed with OVA MHC when peptide stimulation was performed with OVA peptide).

The functional avidity (*i.e.*, logEC_{50} values) of these populations correlated well with their global k_{off}-rates in both the primary and the recall infection setting (**Figure 5-22**A, B). These data included a wide variety of homologous and heterologous combinations of the infection/stimulation epitopes (**Figure 5-22**C, D). Of note, *L.m.* OVA-induced populations were also measured against APL epitopes and followed the pattern of the other *Listeria*/epitope combinations (**Figure 5-22**C, D). This served as a control that the *L.m.* APL/OVA epitope combination did not produce an aberrant trend.

In summary, this data suggested a strong positive association between the global k_{off}-rates and the functional avidity of antigen-specific CD8$^+$ T-cell populations.

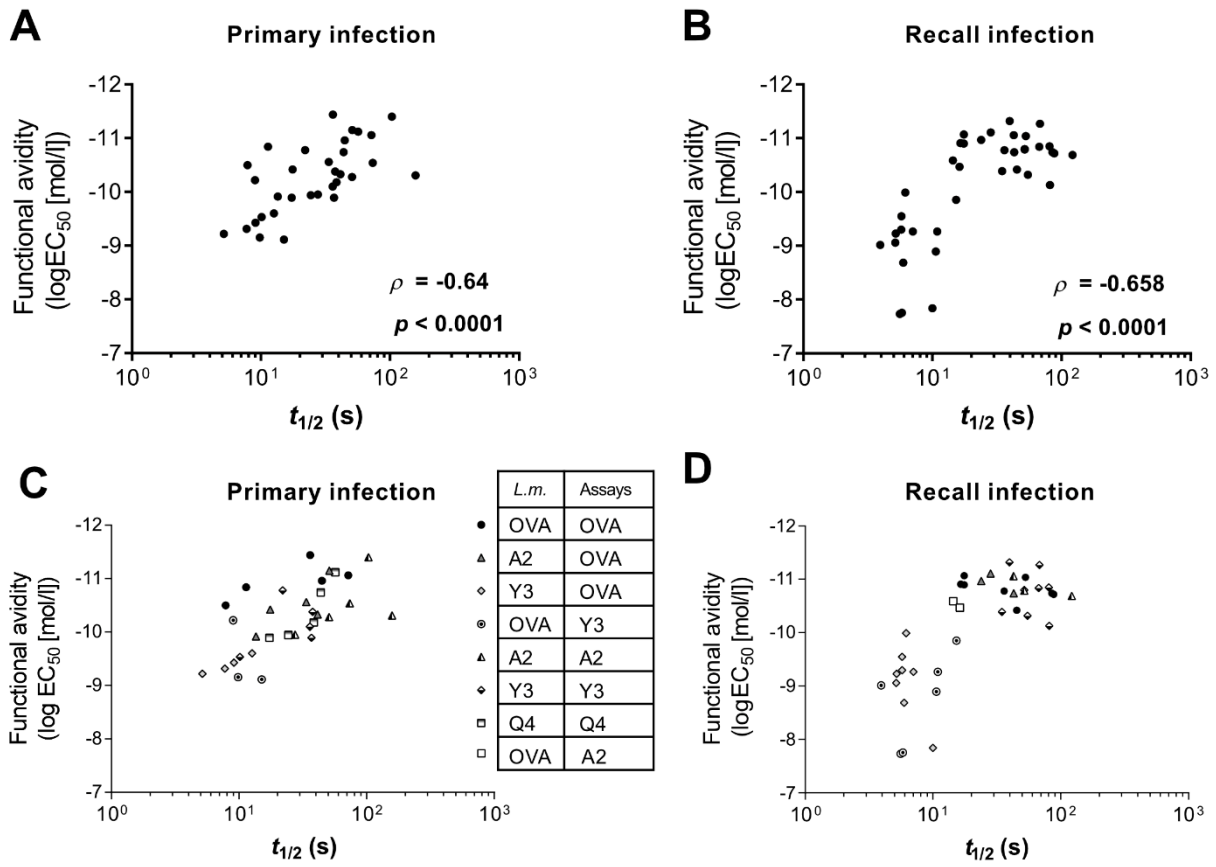

Figure 5-22. Correlation between functional avidity and global $t_{1/2}$ towards the corresponding epitope. A, B, C, D: Correlation of simultaneous pMHC-TCR k_{off}-rate and peptide sensitivity measurements where corresponding epitopes were used in both assays on d8 p.i. (A, C) or d6 after recall infection (B, D). n = 32–38. Each dot represents a mouse. Spearman correlation. **C, D**: Detailed view of (A, B). Inducing *L.m.* strain and pMHCs used in TCR-pMHC k_{off}-rate measurements, or stimulating peptides used in peptide titration assays, respectively, are indicated in the middle. Adapted from (Lückemeier et al. 2022).

5.6 Association of global k_{off}-rates and in vitro and in vivo tumor killing capacity of antigen-specific CD8$^+$ T-cell populations

Previous works have demonstrated an association between TCR avidity of monoclonal T-cell populations and their ability to control tumor growth in vivo (Allard et al. 2017). However, this has not been comprehensively shown for polyclonal T-cell populations, because of the difficulty to assess their full avidity spectrum.

The aim of the next set of experiments was therefore to study whether global k_{off}-rates of polyclonal T-cell populations were associated with their in vitro and in vivo tumor killing capacity.

5.6.1 In vitro killing capacity

The xCELLigence assay allows for real-time cell analysis and assessment of tumor killing by T cells via a reduction in impedance (expressed as ‘cell index’) created by living tumor cells (**Figure 5-23**).

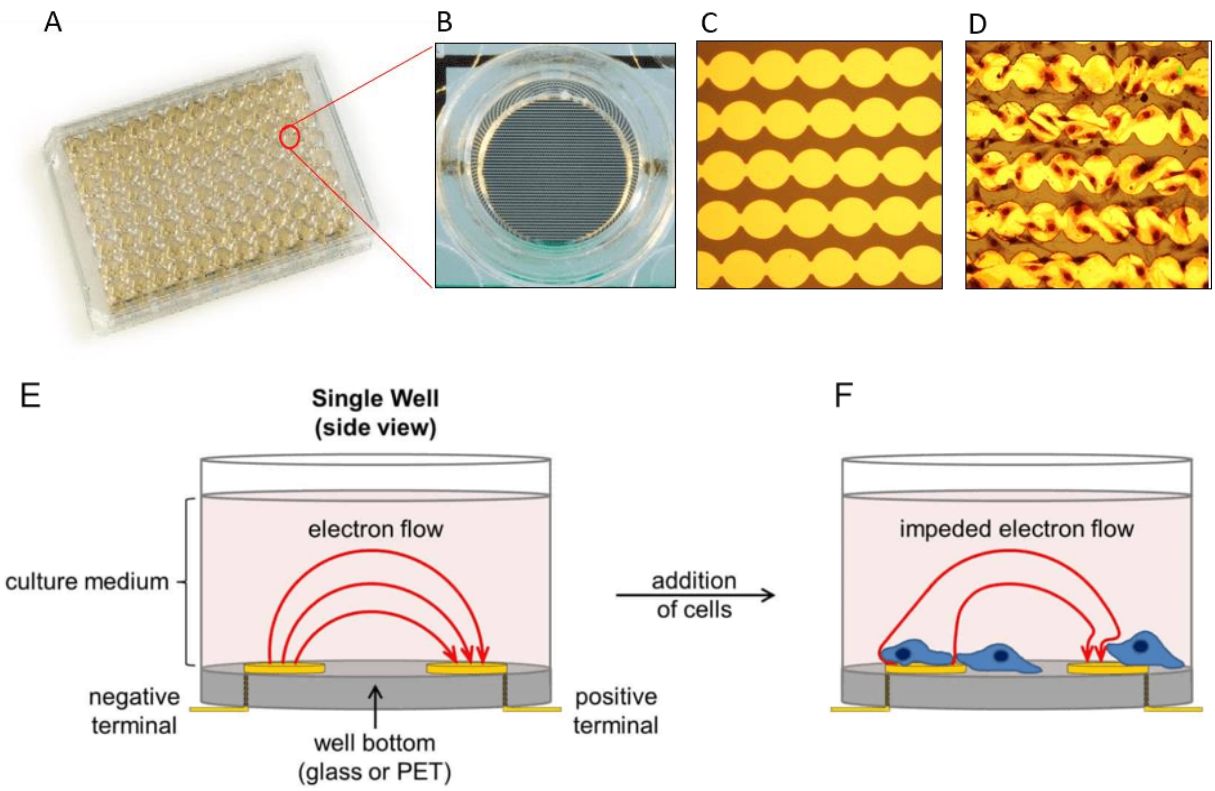

Figure 5-23. „E-Plate® with gold microelectrodes fused to the bottom surface of the wells. A) Image of a 96-well E-Plate®. B) Enlargement of one single well in a 96-well E-Plate®. C) Zoomed-in photograph of gold microelectrodes on the E-Plate® well bottom. D) Unstained human cells, growing on microelectrodes. E, F): Schematic image of electron flow in a single well of an E-Plate. E) Electron flow from one biosensor to the other through culture media only. F) Impeded electron flow from one biosensor to the other due to cells attached/growing on gold microelectrodes." Adapted from (OLS OMNI Life Science GmbH) with express permission by OLS - OMNI Life Science GmbH & Co KG.

The OVA-expressing tumor cell line PancOVA was used for target cells. The cells were seeded out in a 96-well E-plate and placed in an RTCA MP instrument. The following day, splenocytes from mice which have received a secondary infection with *L.m.* OVA, *L.m.* A2, or *L.m.* Y3 6 days earlier were isolated and prepared as described above. Irrespective of the inducing *L.m.* strain, splenocytes were stained with H-2K^b/OVA$_{257-264}$ streptamer solution, as well as CD8α and CD19 mAbs. Secondary infections with *L.m.* Q4 produced insufficient frequencies of H-2K^b/OVA$_{257-264}$ streptamer$^+$ cells for these experiments. To control for variable frequencies of OVA-specific T cells in the different *Listeria* infection settings, a fixed amount of living, CD19$^-$, CD8$^+$, streptamer$^+$ cells were sorted from each group (**Figure 5-24**A). D-biotin was then added to the sorted cells to dissociate streptamers. The sorted cells were added to the PancOVA cells in fixed effector to target ratios (E:T). Control wells received medium only. E-Plates were left at room temperature for 30 minutes to let T cells set, as per supplier recommendation, creating a bump in cell indices after placing the plates back in the RTCA MP (**Figure 5-24**B). Cell indices were normalized to addition time points and killing capacity (cytolysis) was quantified as the average difference in normalized cell index of sample wells (T cells added) to control wells (medium added) after 48 hours (**Figure 5-24**B).

At both E:T ratios, the OVA streptamer-sorted T cells from the *L.m.* OVA and *L.m.* A2 groups showed very similar cytolytic capacity (**Figure 5-24**C). However, the cells from the *L.m.* Y3 group showed a significantly reduced killing capacity (**Figure 5-24**C). This mirrored the previously observed trend for the structural and functional avidity of these groups (compare **Figure 5-24**C to **Figure 5-20**F and **Figure 5-14**B).

To assess the link between killing capacity and global k_{off}-rates in more detail, the cytolysis of each population was plotted against the global $t_{1/2}$ towards OVA acquired from aliquots of the

samples before they were sorted. There was a strong positive correlation between the killing capacity and global $t_{1/2,}$ echoing the results from the peptide sensitivity assay (compare **Figure 5-24**D and **Figure 5-22**B).

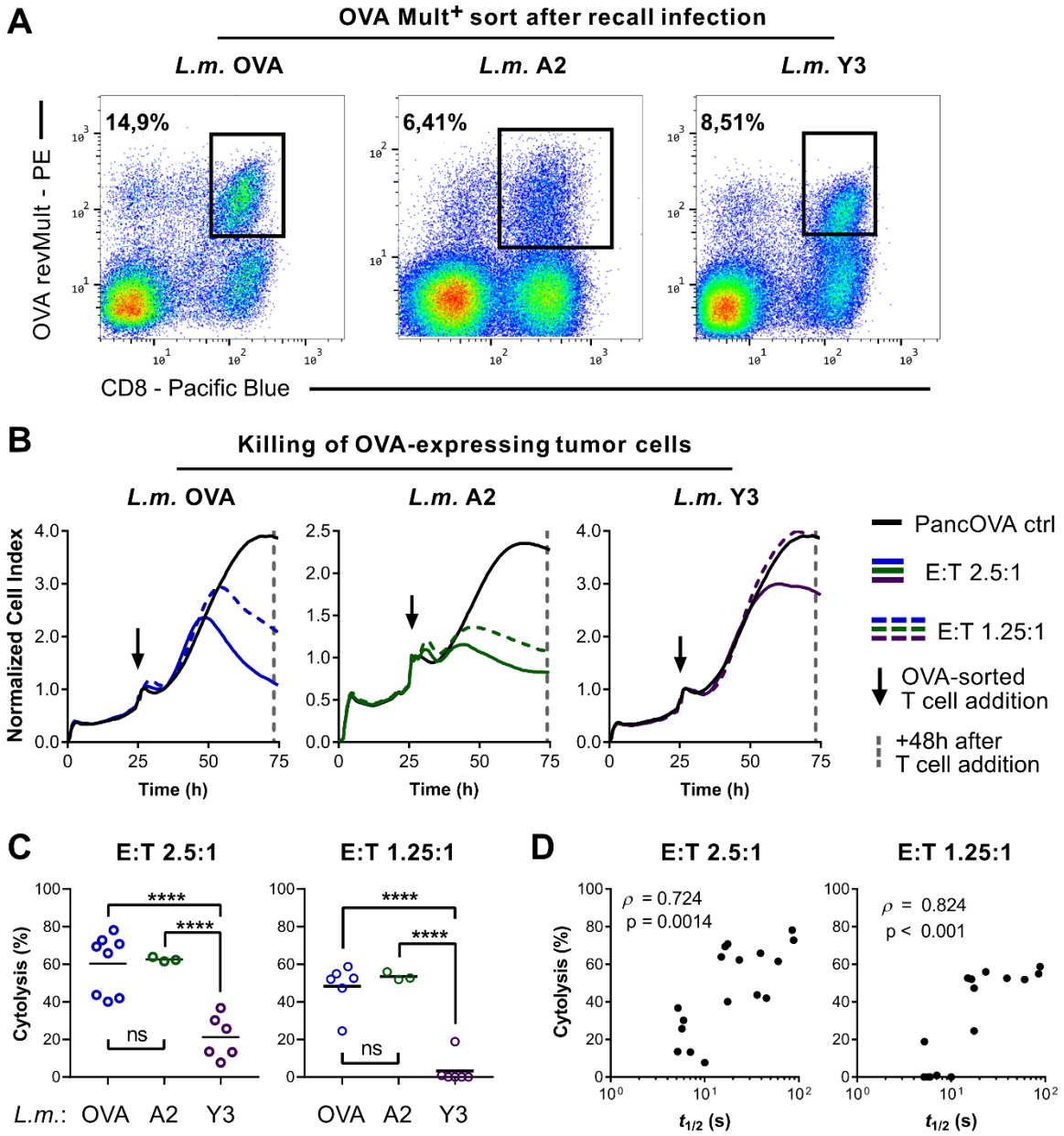

Figure 5-24. In vitro killing by OVA streptamer-sorted and *L.m.* OVA or *L.m.* APL-induced CD8⁺ T-cell populations correlated with their global $t_{1/2}$ towards OVA. A: Representative plots of fluorescence-associated cell sorting of CD8⁺, reversible OVA multimer⁺ populations for tumor killing assays on d6 after recall infection. Streptamer staining was reversed with d-biotin before T-cell transfer. Inducing *Listeria* strains are indicated above the plots. **B**: Representative plots of real-time tumor killing assays. OVA-expressing tumor cells (PancOVA) were grown for 24h before either the populations described in (A) or medium alone was added (indicated by arrows) in different effector to target ratios (E:T). Cell indices were normalized to those time points, and the difference between wells with and without T cells 48 h later measured as cytolysis in %. Lines represent the means of at least three wells. **C**: Quantification of cytolysis at different E:T. Inducing *Listeria* strains are indicated below graphs. n = 3–8 from four independent experiments. Each dot represents a mouse. Bars indicate means. Statistics: Ordinary one-way ANOVAs followed by Tukey tests. ****p-value < 0.0001. ns, not significant. **D**: Correlation of simultaneous pMHC-TCR k_{off}-rate and cytolysis measurements at different E:T (upper and lower panel) on d6 after recall infection. n = 15–17 per E:T ratio. Each dot represents a mouse. Spearman correlation. Adapted from (Lückemeier et al. 2022).

5.6.2 In vivo tumor protection

In order to translate the results from the in vitro tumor killing experiments to a murine in vivo setting, the OVA-expressing MC38-OVA tumor cell line was used as an in vivo tumor model.

Recipient mice were irradiated with 5Gy one day before the transfer of tumor cells because most non-irradiated mice rejected the tumor cells (data not shown). On the day of transfer (d0), MC38-OVA tumor cells were prepared as described above and injected subcutaneously into the flank of the recipients. Recipients were surveilled regularly for a maximum of 50 days and sacrificed if the tumor reached a critical size or formed ulcers.

To test the protection from these tumors by OVA-specific T cells, splenocytes of mice infected with *L.m.* OVA, *L.m.* A2, or *L.m.* Y3 were isolated 8 days after primary infection. Splenocytes from all groups were stained with H-2K^b/OVA$_{257-264}$ streptamers, as well as CD8α, and CD19 antibodies. A fixed amount of living, CD19$^-$, CD8$^+$, streptamer$^+$ cells was sorted from each group, and d-biotin was added to dissociate streptamers. The sorted cells were then transferred intraperitoneally into the irradiated recipient mice one day before the transfer of tumor cells (**Figure 5-25**A).

Mice who received OVA-specific T cells from *L.m.* OVA- or *L.m.* A2-induced populations showed longer median survival than those who received OVA-specific T cells from *L.m.* Y3-induced populations or just saline solution (**Figure 5-25**B). There was a significant all-curve difference between the survival curves, but the effect and number of recipients were not large enough to identify a significant difference between specific curves (**Figure 5-25**B).

Taken together with the xCELLigence experiments, these data showed that the infection-induced polyclonal T-cell populations with higher TCR-ligand global $t_{1/2}$ towards OVA conferred superior protection against OVA-expressing tumor cells in vitro and in vivo.

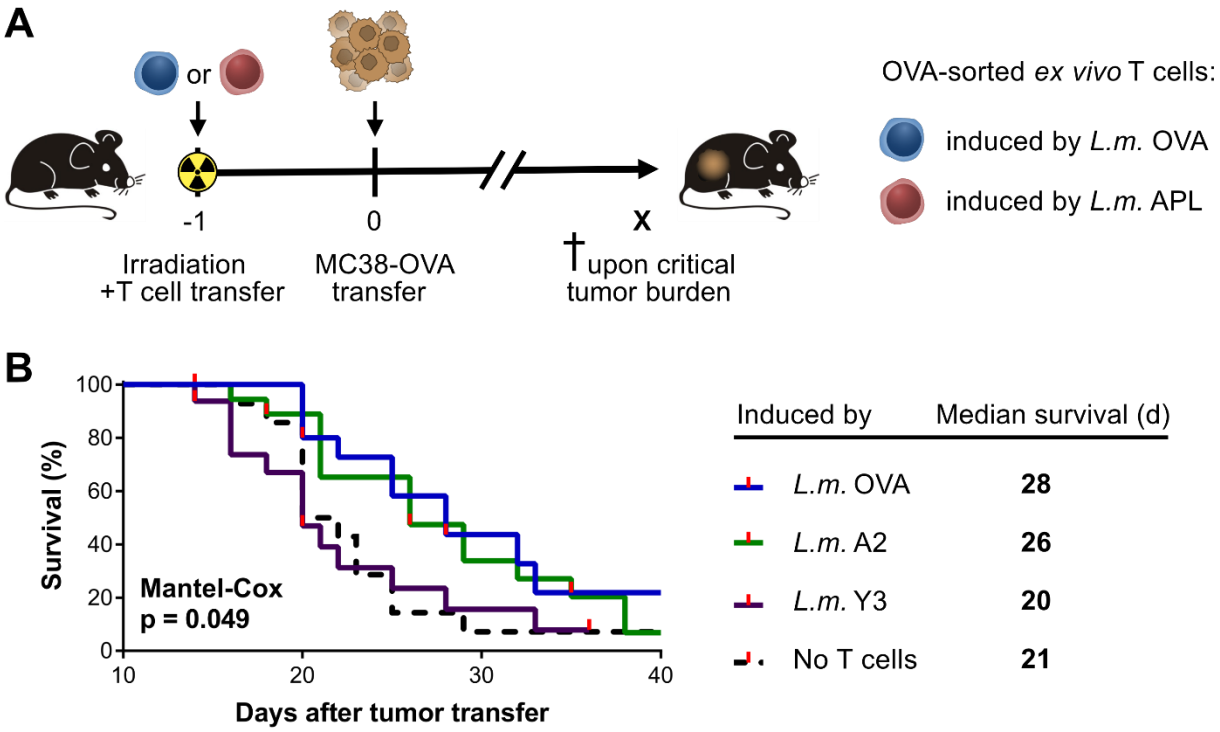

Figure 5-25. In vivo tumor protection by OVA streptamer-sorted and *L.m.* OVA or *L.m.* APL-induced CD8$^+$ T-cell populations. A: Experimental design. CD8$^+$, reversible OVA multimer$^+$ populations were sorted from splenocytes on d8 p.i. with either *L.m.* OVA or *L.m.* APL. Recipient mice were irradiated, and sorted populations transferred 1 day before OVA-expressing tumor cells (MC38-OVA) were injected into the flank. Mice were monitored and sacrificed upon critical tumor

burden. **B**: Left: Kaplan–Meier survival plot of mice specified in (A). Recipients were grouped by *Listeria* strains that induced the sorted populations they received. Right: Legend and table of median survival in days after MC38-OVA transfer. n = 15–19 per group. Mantel-Cox log rank test for the all-curve difference. Adapted from (Lückemeier et al. 2022).

5.7 Global k_{off}-rates in humans and predictability from subclonal TCR-ligand k_{off}-rates

The data presented thus far have been gathered in the murine setting. The next set of experiments was conducted to test whether global k_{off}-rates of polyclonal T-cell populations could also be measured in the human setting. In particular, the influence of constituent monoclonal T-cell populations on the emerging global k_{off}-rates was examined.

The staining, sort, expansion, and TCR-ligand k_{off}-rate assays, but not the analyses, were performed by Patrick Huppertz and Manuel Effenberger.

5.7.1 Sort and single cell expansion of YFV-specific T-cell clones

In analogy to the murine TCR library detailed in 5.3, monoclonal populations with distinct TCR-ligand dissociations were needed to perform the abovementioned analyses. Yellow fever virus vaccine (YFV)-induced CD8$^+$ memory T cells were used as a model population because they were shown to persist in circulation over years and to rapidly expand in culture conditions (Fuertes Marraco et al. 2015). PBMCs from a blood sample of a YFV-vaccinated donor were stained with two HLA-A2/YFV NS4B$_{214-222}$ - multimers (with differently labeled streptavidin backbones) and CD3, CD8, CCR7, and CD45RA mAbs for surface antigen staining. To select for stem cell memory T cells (T_{scm}) with a high proliferative capacity, PI$^-$, CD19$^-$, CD3$^+$, CD8$^+$, CCR7$^+$, CD45RA$^+$, double HLA-A2/YFV NS4B$_{214-222}$ multimer$^+$ cells were sorted, and single cells expanded in a feeder cell culture with irradiated feeder PBMC and IL-2 supplementation (**Figure 5-26**A). Cells were checked for growth on d9 after the sort (**Figure 5-26**B).

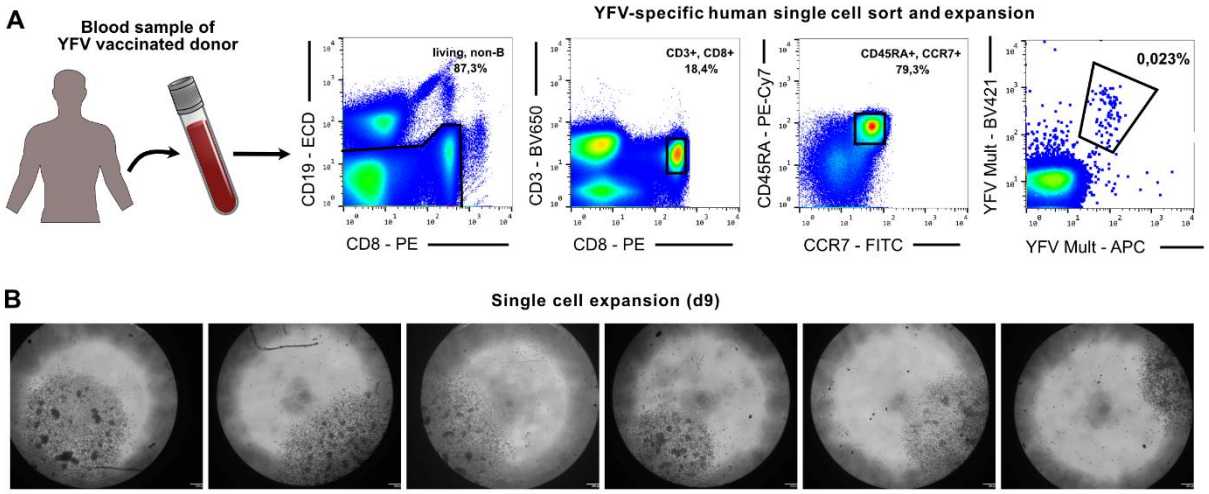

Figure 5-26. Sort and expansion of YFV-specific T cells with a T_{scm} phenotype. A: PBMCs of a yellow fewer virus (YFV) vaccinated human donor were isolated from a blood sample and stained. PI$^-$, CD19$^-$, CD3$^+$, CD8$^+$, CCR7$^+$, CD45RA$^+$, double HLA-A2/YFV NS4B$_{214-222}$ multimer$^+$ (YFV-specific) single cells were sorted into a microtiter plate and expanded in a feeder cell culture. **B**: Representative pictures on d9 after sort of single cell-expanded colonies derived from the cells described in (A).

5.7.2 TCR-ligand k_{off}-rates of T-cell populations from pooled T-cell clones

Next, 16 of the expanded single cell-derived T-cell clones were harvested on d11 after the sort to perform a k_{off}-rate assay. To examine the relationship between global k_{off}-rates and the constituent monoclonal k_{off}-rates, the clones were labeled with a unique color code. This allowed the pooling of the samples to mimic a polyclonal population and reduce technical confounders during the read-in while also allowing identification and k_{off}-rate measurement of each constituent monoclonal population via their color code.

Therefore, samples were stained with HLA-A2/YFV NS4B$_{214-222}$ streptamer solution, CD8α mAb, as well as a unique combination of CD45 antibody-fluorophore conjugates (**Figure 5-27**A). Exactly 16 populations were selected because the established combination of four different CD45 antibody-fluorophore conjugates allowed for the unique labeling of a maximum of 16 samples when pooled. The CD45 color code was shown to not significantly alter the k_{off}-rate (Peter Patrick Huppertz 2016).

The dissociation of the pooled populations showed a kinetic which was reminiscent of that of the murine antigen-specific population (compare **Figure 5-27**A to **Figure 5-14**A) indicating that polyclonal T-cell populations could also be measured in the human setting using the same methodology. In contrast to the murine setting, however, as detailed in 5.1.3, the $t_{1/2}$ for this dissociation was calculated using an *un*constrained one-phase exponential decay, because of de-quenching effects of the streptamer.

Of the 16 samples, four had to be excluded: Three populations were too small (<500 events) for accurate quantification of the $t_{1/2,}$ and one population showed two distinct kinetics, hinting at contamination of the monoclonal T-cell population with at least one other clone (data not shown). The remaining 12 populations were identified via their color code and their $t_{1/2}$ was calculated with an unconstrained one-phase exponential decay (**Figure 5-27**A, B). The single cell-expanded populations showed a wide range of sizes and avidities (**Figure 5-27**C).

In a first step, to investigate the connection between global k_{off}-rates and the constituent monoclonal k_{off}-rates, a unifying gate was put on the color codes of clone b and clone k (**Figure 5-27**D). These clones were chosen because they were very similar in size, yet quite different in their $t_{1/2}$ (**Figure 5-27**D, E). The resulting biclonal population exhibited a measured global $t_{1/2}$ of 145s (**Figure 5-27**E). This closely approximated the arithmetic mean of the $t_{1/2}$ of the two populations, 148s. This result echoed the findings for murine global $t_{1/2}$ shown in **Figure 5-7**, indicating that human global $t_{1/2}$ merge in a similar manner as murine global $t_{1/2}$.

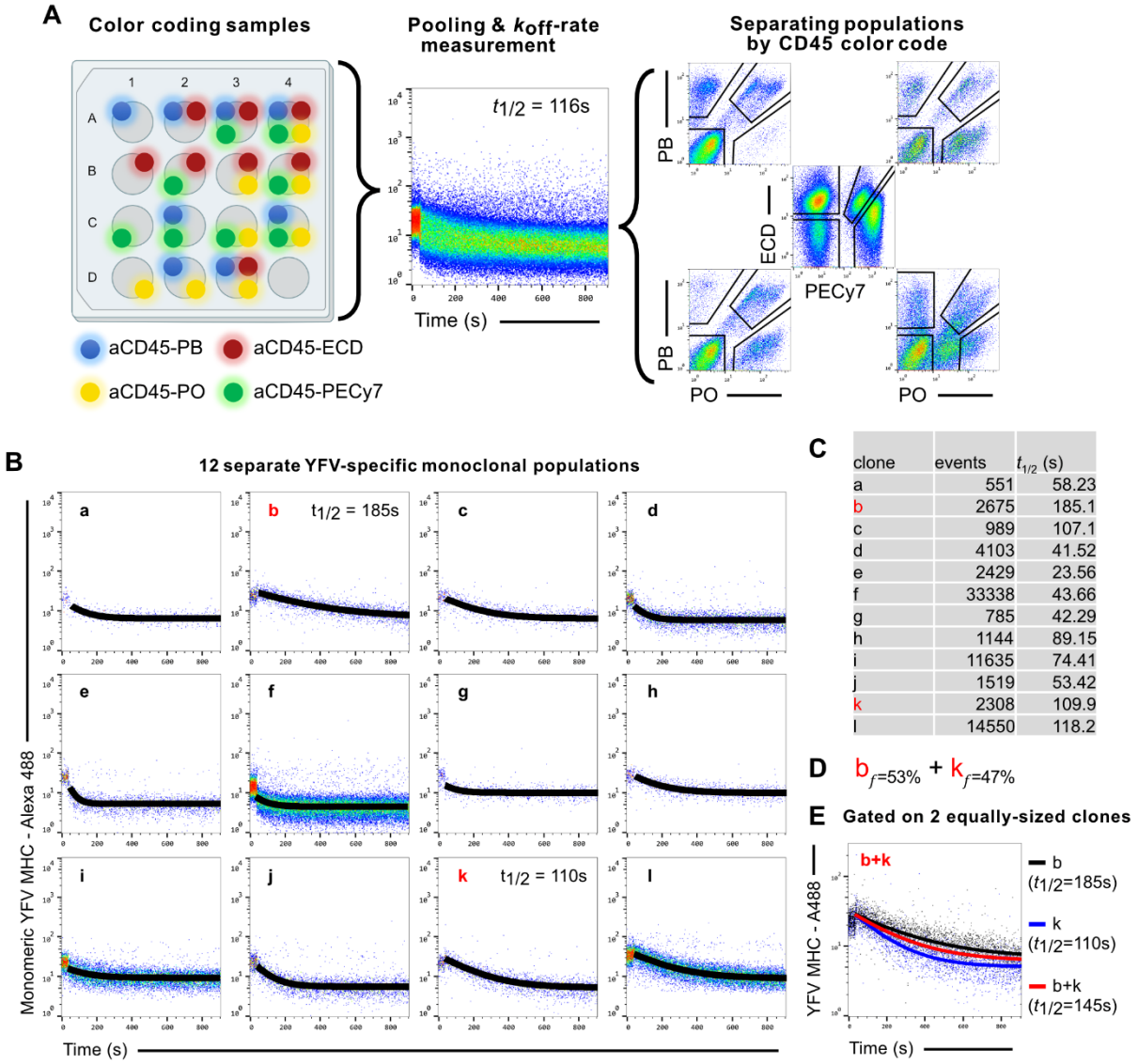

Figure 5-27. **Pooled TCR-ligand k_{off}-rates of multiple color-coded monoclonal T-cell populations from human YFV-specific single cell expanded T-cell clones. A**: Expanded populations originating from the single cells described in (**Figure 5-26**) were restained at day 11 with CD8 mAb and reversible YFV multimers and each population stained with a unique combination of CD45 mAb-fluorophore conjugates. All populations were mixed and read in as one sample to eliminate sample-to-sample variation. During analysis, the clones were identified via fluorophore combination, and their pHLA-TCR k_{off}-rates were calculated. **B**: pHLA-TCR k_{off}-rates of 12 separate YFV-specific monoclonal populations obtained as described in (A) and (B). **C**: Identifier, size (as determined by flow cytometry) and $t_{1/2}$ of all YFV-specific, single cell expanded clones described in (B). **D**: Frequencies of clones b and k in the mixed population b+k described in (E). **E**: Exponential decay fits of the approximately equally sized clones b and k in addition to that of both clones merged into one population 'b+k'. Adapted from (Lückemeier et al. 2022).

5.7.3 In silico prediction of global k_{off}-rates from subclonal dissociation parameters

Expanding on this finding, the more detailed equation described in 4.4 was used to explore whether it could predict the global k_{off}-rate of human biclonal populations using the dissociations in **Figure 5-27**.

Firstly, the dissociation parameters (MFIs and k_{off}-rates) of two monoclonal populations shown in **Figure 5-27** were inserted into the equation described in 4.4, and the frequency parameters

were set to 50% to adjust their sizes 1:1. The resulting global $t_{1/2}$ was called 'equation predicted $t_{1/2}$'.

Secondly, the .fcs data of these monoclonal populations were concatenated. This was equivalent to simply gating on both populations and exporting that data for analysis, but crucially allowed for adjusting the size of both populations: Differences in size were balanced out by iteratively adding the .fcs data of the smaller clone multiple times until the difference in the number of events was <5% (for more details see 4.2.9). After adjustment, the global $t_{1/2}$ of this biclonal dissociation was measured using the unconstrained one-phase decay as per usual. The resulting global $t_{1/2}$ was called 'dissociation fit output'.

The equation accurately predicted the measured global $t_{1/2}$ of these human biclonal populations (**Figure 5-28**A). This matched the findings for murine dissociations (see **Figure 5-9**) and corroborated that global k_{off}-rates accurately and linearly merge subclonal k_{off}-rates according to their size in both the human and the murine setting.

To assess the fidelity with which the global k_{off}-rates of polyclonal populations could be predicted from the dissociation parameters and sizes of the constituent T-cell clones, all 12 dissociations of the monoclonal populations described in **Figure 5-27** were mixed at varying size-weights with frequencies ranging from a minimum of 5% to a maximum of 50% (**Figure 5-28**B). This simulated polyclonal populations with different frequencies of high-, medium-, and low-avidity T-cell clones. 1000 mixed, *i.e.* polyclonal, populations with randomly generated frequencies of the constituent clones were created and the dissociation fit output and equation predicted global $t_{1/2}$ of each mixed population determined as described above: The .fcs data of all 12 monoclonal dissociations were concatenated and the assigned frequency of a given clone achieved by iteratively pasting its .fcs data into the mixed populations' .fcs file with the help of a programmed script until the frequency was within <2%-points of its assigned frequency (for more details see 4.2.9). The resulting .fcs files were analyzed as per usual, their global k_{off}-rates measured, and the resulting $t_{1/2}$ reported as 'dissociation fit output'. Next, the dissociation parameters (MFIs and k_{off}-rate) of all monoclonal populations were inserted into the equation described in 4.4, and the frequency f parameters were set to the frequencies assigned to each clone. The resulting global $t_{1/2}$ was reported as 'equation predicted $t_{1/2}$'.

The predicted global $t_{1/2}$ closely approximated the 'measured' global $t_{1/2}$ (**Figure 5-28**B). This indicated that the global $t_{1/2}$ of polyclonal T-cell populations could be predicted with high precision from the dissociation parameters and frequencies of their constituent clones in humans.

This finding might enable TCR avidity-tailoring of polyclonal T-cell therapeutics by compiling T-cell clones with known TCR-ligand k_{off}-rates at predetermined frequencies.

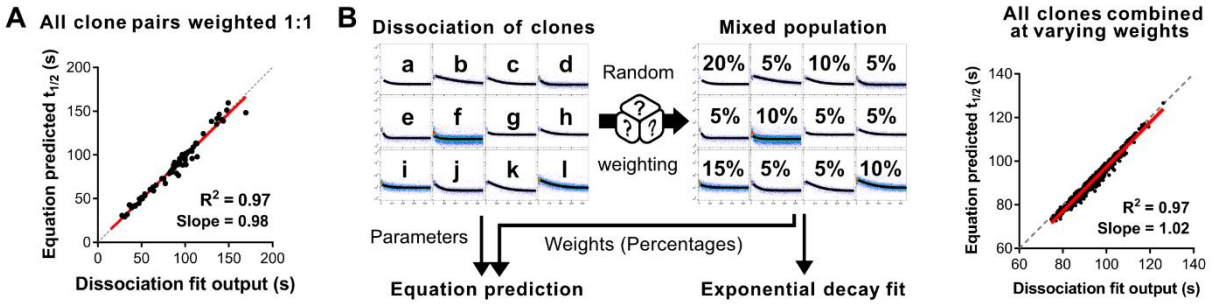

Figure 5-28. In silico prediction of global k_{off}-rates from subclonal dissociation parameters. A, B: Correlation between the $t_{1/2}$ fitted to the merged dissociations and the $t_{1/2}$ predicted from the dissociation parameters of the constituent monoclonal dissociations. **A**: Two clones merged at a time after adjusting their sizes 1:1. **B**: All 12 clones merged at varying weights. Left panel: schematic. The clones were assigned random weights of as little as 5% and as much as 50% and mixed into polyclonal populations. Right panel: Depiction of 1000 randomly chosen polyclonal populations. Each black dot represents one polyclonal population. Red solid lines represent linear regressions. Grey dashed lines are graphs of f(x) = x. One independent experiment is depicted. Adapted from (Lückemeier et al. 2022).

6. Discussion

T-cell therapy has shown remarkable clinical success in fighting cancer and viral infections. An important factor for the functionality of T cells that could inform the design of T-cell therapeutics is the structural avidity of the T-cell receptor. While the relevance of TCR avidity has been shown in multiple studies, they overwhelmingly relied on monoclonal T-cell populations like cell lines, TCR transgenic populations, or single cell-sorted and expanded T cells. Although they enable some inferences to be made about polyclonal populations, a clear demonstration of these results for polyclonal populations is lacking. However, most T-cell therapeutics employed in the clinic like donor lymphocyte infusions, tumor infiltrating lymphocytes, and virus-antigen-specific T cells consist of polyclonal populations.

A major obstacle to surveying the TCR avidity of polyclonal T-cell populations is of technical nature. Most assays measuring TCR-ligand avidity can only do so on a per TCR basis. This makes a comprehensive analysis of the TCR structural avidity of polyclonal T-cell populations prohibitive and introduces selection bias. Therefore, this thesis aimed to explore the link between the TCR avidity of polyclonal populations and their functionality.

This work expands on the flow cytometric TCR-ligand k_{off}-rate assay utilizing reversible pMHC streptamers to measure the TCR avidity of polyclonal antigen-specific $CD8^+$ T-cell populations. The acquired parameter termed global k_{off}-rate was herein shown to reflect an average measure of avidity across the entire population by merging subclonal avidities in a linear and unbiased manner. A novel APL-based *L.m.* infection model was established to induce murine T-cell populations with stably tiered global k_{off}-rates towards the OVA model epitope. Of note, these populations did not differ significantly in phenotypic composition. Moreover, APL-induced, OVA-specific populations were mostly cross-reactive. These populations revealed a robust positive correlation between global k_{off}-rates and functional avidity towards the OVA and APL epitopes. Moreover, the ability to kill OVA-expressing tumors in vitro was similarly positively correlated with the global k_{off}-rates. To test the relevance of TCR avidity of polyclonal populations for adoptive T-cell transfer, OVA-specific T cells from APL-induced and OVA-induced immune responses were transferred into mice harboring OVA-expressing tumors. Indeed, these mice showed longer survival when they had received T cells from infection settings inducing higher-avidity T-cell responses. Furthermore, the methodology was translated to human $CD8^+$ T cells. A deeper investigation of the composition of global k_{off}-rates revealed that it could be predicted with high fidelity from monoclonal TCR-ligand k_{off}-rates of the constituent T-cell clones. This insight might be valuable for tailoring the avidity of polyclonal T-cell therapeutics by deliberately mixing T-cell clones with known TCR-ligand k_{off}-rates.

6.1 Streptamer-based TCR-ligand k_{off}-rate assay of antigen-specific polyclonal $CD8^+$ T-cell populations

There are many established assays that measure TCR-ligand k_{off}-rates (Allard et al. 2017; Gannon et al. 2015; Huang et al. 2010; Huppa et al. 2010). However, most of them require extensive sample preparation and cannot analyze multiple differing TCRs at a time. A notable exception is the analysis of pMHC multimer staining intensity over time, which is easily applicable to polyclonal populations even ex vivo. Notwithstanding, because of multimeric binding, it is not suitable for the analysis of monomeric TCR-pMHC interactions and usually requires blocking agents to prevent rebinding, which in turn influence dissociation kinetics depending on their concentration. Moreover, some studies demonstrated a correlation between this pMHC multimer k_{off}-rate and functionality, but many do not (Wilde et al. 2012; Tian et al. 2007; Laugel et al. 2007). Therefore, pMHC multimer k_{off}-rate assays are an unreliable parameter to assess the avidity of polyclonal T-cell populations, and other assays to do so are lacking.

Previous works utilizing the streptamer-based microscopic TCR-ligand k_{off}-rate assay have demonstrated a correlation between the k_{off}-rate yielded by it and functional parameters in

monoclonal populations (Nauerth et al. 2013; Knall 2007). The compatibility between the microscopic version and the flow cytometric version was previously shown (Nauerth et al. 2016). The flow cytometric version also allows for the analysis of antigen-specific $CD8^+$ T cells among unspecific cells via double multimer staining (Nauerth et al. 2016). Expanding on this methodology, murine antigen-specific populations were measured in this work, allowing for a quantification of the TCR-ligand k_{off}-rate of polyclonal populations directly ex vivo (**Figure 5-1**, **Figure 5-2**).

6.1.1 Technical limitations

The assay operates through the (double) multimer staining of T cells. Therefore, it is restricted to the assessment of T cells stainable with both irreversible and reversible pMHC multimers. Despite high rates of congruence between the multimer$^+$ events (**Figure 5-2**D) and frequencies of streptamer$^+$ events among irreversible multimer$^+$ events being routinely above 90% (**Figure 5-11**), a small fraction of ostensibly antigen-specific T cells which can bind just one type of multimer remains elusive for this assay. What's more, T cells which do not bind multimers at all can still be antigen-specific and meaningfully participate in immune responses (Rius et al. 2018), but are not analyzable by this method. Most of these T cells are presumed to have TCRs with low structural avidity. Their absence in the analyzed dissociations would lead to a slight overestimation of the level of structural avidity of the entire antigen-specific T-cell population by the assay used herein.

Novel insights into molecular and mechanical features have added new dimensions to the TCR-pMHC interaction: Canonical vs. non-canonical topology (Zareie et al. 2021) and the formation of slip bonds vs. catch bonds (Sibener et al. 2018) irrespective of TCR affinity and avidity. They have been implicated to impact proximal TCR signaling and thus could explain exceptions of high-avidity TCRs performing poorly in T-cell activation. These factors could therefore limit the predictive power of TCR-ligand k_{off}-rate assays.

While pMHC binding is largely dependent on TCR affinity, other binding partners -most importantly CD4 and CD8- also contribute to the interaction. The extent to which the Streptamer-based TCR-ligand k_{off}-rate assay can incorporate these parameters is described below.

Influence of CD8

CD8 is a co-receptor that binds the heavy chain of MHC I molecules and stabilizes TCR – pMHC binding (Garcia et al. 1996; Luescher et al. 1995). The streptamer-based TCR-ligand k_{off}-rate assay does indeed measure the strength of all influences on pMHC retention on the cell surface and can thus not quantify the influence of each binding component individually. However, the influence of CD8 on the TCR-ligand k_{off}-rate has previously been studied specifically for this assay. In TCR re-expression experiments utilizing cell lines lacking CD8 or primary $CD4^+$ T cells without CD8 expression, k_{off}-rates were generally moderately faster than observed in cells that express CD8 (Weißbrich 2015). Moreover, many transgenically re-expressed TCRs showed multimer staining independent of CD8 expression hinting at a small influence of CD8 on TCR-ligand k_{off}-rates (Effenberger 2020).

Assessing TCR-ligand k_{off}-rates of $CD4^+$ T cells

Employing the streptamer-based TCR-ligand k_{off}-rate assay to assess the TCR avidity of $CD4^+$ T cells has not been possible to date. An important reason is that staining of $CD4^+$ T cells with pMHCII multimers is much more difficult compared to pMHCI multimers (Wooldridge et al. 2009). This is in part due to a generally lower affinity between pMHCII molecules and TCRs (Cole et al. 2007), hardly any contribution of CD4 to the stabilization of the TCR-ligand interaction (Jönsson et al. 2016; Hamad et al. 1998; Crawford et al. 1998), and higher complexity in the generation of recombinant pMHCII molecules due to lower yields and stability compared to their pMHCI counterparts. Important technological advances will have to be made

to overcome these hurdles and enable TCR-ligand k_{off}-rate measurements of $CD4^+$ T cells with a pMHCII streptamer-based assay. This work was therefore limited to $CD8^+$ T-cell populations.

Challenges with very fast TCR-ligand dissociations

Despite being reproducible for many inter-individual antigen-specific $CD8^+$ T-cell populations, it quickly became clear in this work that TCR-ligand dissociations of the flow-cytometric streptamer-based k_{off}-rate assay with a particularly fast decline in pMHC MFI were challenging to analyze. The exclusion of all data before a sharp drop in Strep-Tactin MFI (marking the rapid dissociation of the Strep-Tactin backbone after the addition of d-biotin) occasionally excluded the majority of a (very fast) dissociation which had already occurred when the non-excluded data started. Fitting a curve to the remaining, mostly flat dissociation kinetic paradoxically led to very long and unrepresentative $t_{1/2}$ values (**Figure 5-3**). In order to remedy this misclassification, the one-phase exponential decay fitting method was constrained, and the start value was set to the staining intensity of the pMHC before the addition of d-biotin (**Figure 5-3**).

While this methodology conceptually harnesses the information of the initial staining intensity (which should indeed represent the starting point of the dissociation) and should improve curve fitting, it only holds true in case that all pMHCs of the streptamer are bound to TCRs and are subject to the TCR-ligand interaction. Otherwise, unbound pMHC should rapidly dissociate from the cells after the addition of d-biotin leading to a sharp drop in pMHC MFI and a measured k_{off}-rate which is faster than the true k_{off}-rate of the TCR-ligand interaction.

Complicating this issue further, an initial sharp drop in pMHC MFI is to be expected either way by virtue of the lag time between injection of d-biotin into the sample and analysis of the first cells which encountered d-biotin by the flow cytometer: The cells which have encountered d-biotin immediately undergo pMHC dissociation even in the tubing of the flow cytometer and the first of these cells to be analyzed will have already undergone several seconds worth of TCR-ligand dissociation during travel. Indeed, a sharp drop in pMHC MFI was found on the FCM plot several seconds after the addition of d-biotin (**Figure 5-3**).

This lag time does imply a limit of accurate quantification by the *un*constrained analysis method for very fast dissociations ($t_{1/2}$ of <7 seconds) which are (almost) completed by the end of the travel time. This could be especially impactful for dissociations of polyclonal T-cell populations with a large fraction of very fast kinetics that would be systemically underrepresented in the k_{off}-rate as analyzed by the *un*constrained method.

The constrained method, however, does remedy this by including the pre-dissociation MFI thereby perceiving fast kinetics as a large difference between pre-dissociation MFI and the MFI after the initial drop.

Both methods show similar results in the analysis of monoclonal populations (**Figure 5-3**E). However, because the novel constrained analysis method led to much-improved curve fitting for fast dissociation kinetics while still preserving good fittings for long dissociation kinetics, it was deemed more appropriate for the analysis of murine polyclonal TCR-ligand dissociations.

It should be noted, however, that this limits the comparability with values acquired by the unconstrained methods from other works which apply the streptamer-based flow cytometric TCR-ligand k_{off}-rate assay. Populations with fast dissociation kinetics remain challenging to measure accurately with this methodology.

6.1.2 Distinct sub-kinetics in dissociations of polyclonal populations

Some infection-induced polyclonal dissociations showed 2 or more distinct kinetics within the overall dissociation (**Figure 5-4**C, **Figure 5-14**A). This most likely reflects the presence of large subpopulations or even clones with distinct levels of avidity. This line of thought is supported by the similarity of the biclonal dissociations resulting from the overlay of two monoclonal dissociations (**Figure 5-9**).

These distinct kinetics seem to be rare and exclusively occurred in dissociations of antigen-specific populations after secondary infection (compare **Figure 5-4**C and **Figure 5-14**A with **Figure 5-11**). A reason for this could be an increased presence of high-avidity T cells and narrowing of the T-cell response after a recall infection due to “avidity maturation” (Busch und Pamer 1999; Savage et al. 1999).

This phenomenon could conceivably be leveraged to measure the frequency of subpopulations with distinct TCR avidities by gating on the sub-kinetics. However, this would require a higher resolution of these sub-kinetics and was not possible to robustly perform in this work.

Novel technological developments in measuring TCR avidity on a single-cell level with a high throughput or further refinements of the resolution of the streptamer-based TCR-ligand k_{off}-rate assay might allow for such analyses in the near future.

6.1.3 Global k_{off}-rates merging subclonal k_{off}-rates into a parameter for TCR structural avidity of polyclonal populations

After demonstrating the feasibility of acquiring dissociation kinetics of polyclonal antigen-specific T-cell populations, it was unclear how to analyze them to yield a meaningful parameter of TCR avidity. The herein developed ‘global’ k_{off}-rate utilizes the one-phase exponential decay curve fitting model which was already used to analyze monoclonal populations. However, as the name suggests, it was developed to be fit to one-phase decays, but polyclonal populations would naturally exhibit multiple decay processes simultaneously. Moreover, it was unclear whether dissociation kinetics of higher or lower avidity would equally influence the curve fitting process or whether this mode of analysis was biased towards certain avidity levels. Lastly, in a polyclonal population, T cells of differing avidity could conceivably interact during the dissociation process, leading to distortions in their individual dissociation kinetics and the assessment of the global avidity (Martin-Blanco et al. 2018).

Several in vitro and in silico experiments with pooled or overlayed monoclonal populations showed that the frequency-weighted sums of the $t_{1/2}$ and MFIs of the ‘one-phase exponential decay’ curve fitting model of the constituent dissociations predicted the global $t_{1/2}$ of mixed populations very precisely. The validity of these results was corroborated by ex vivo color coding, pooling, and measuring multiple pairs of monoclonal antigen-specific TCR transgenic populations. They also excluded the possibility of major interference of dissociation kinetics by T-cell populations among each other as the k_{off}-rates of each individual clone in the biclonal populations was comparable to their k_{off}-rates when measured alone (compare **Figure 5-7** and **Figure 5-9**).

This supports the use of the ‘one-phase exponential decay’ curve fitting model also for polyclonal populations. Several attempts at fitting a multiple decay model to the dissociation kinetics of physiological polyclonal populations showed poor fits (data not shown). This is likely due to the vast number of kinetics these populations usually exhibit which are hard to capture accurately with this assay. Moreover, yielding multiple k_{off}-rates within a population comes at the cost of having a single parameter of TCR avidity that can be correlated with functional parameters.

Another factor was that the data demonstrated that high- and low-avidity kinetics were weighted equally by the global k_{off}-rate analysis according to their frequency in the overall population. Therefore, this method was analogous to measuring each clone individually and proportionally adding their k_{off}-rates into a global k_{off}-rate. This conceptually links the global k_{off}-rate of the flow cytometric TCR-ligand k_{off}-rate assay to taking the mean of the k_{off}-rates measured of the individual T cells in the microscopic version of this assay. However, a thorough comparison of the global k_{off}-rate and the mean of the k_{off}-rates acquired by the microscopic assay was not done in this work.

6.2 APL-induced polyclonal T-cell populations as a model to link global k_{off}-rates and functionality

To investigate the impact of global k_{off}-rates on functional parameters, a method was needed that robustly yielded polyclonal T-cell populations with differing global k_{off}-rates, but otherwise similar properties.

Zehn and colleagues previously showed that a variety of APLs of the OVA epitope could still stimulate monoclonal OT-1-TCR transgenic $CD8^+$ T cells (whose cognate ligand is the OVA epitope), but with decreasing strength (Zehn et al. 2009). This setup showed promise to examine the link between TCR ligand k_{off}-rate and functionality with the OT-1 TCR and different APLs but would once more be restricted to a monoclonal population.

To yield polyclonal T-cell populations of tiered avidity towards the OVA epitope, "recombinant *Listeria monocytogenes* strains stably expressing chicken Ovalbumin ($AA_{134–387}$) containing either the native ligand $SIINFEKL_{257–264}$ ['OVA'] or the APL" A2, Y3, and Q4 (as described and used in (Zehn et al. 2009) were used to infect mice. Because the *L.m.* strains genetically only differed in the short sequence coding for OVA/the APL, they would putatively cause similar courses of infection and induce very similar T-cell populations varying only in their structural avidities towards OVA/the APL.

Indeed, the $CD8^+$ T-cell populations induced by *L.m.* OVA and *L.m.* APL strains did not vary significantly in phenotypic composition (**Figure 5-21**), TRBV diversity (**Figure 5-19**), or structural avidity towards the inducing epitopes (**Figure 5-12**, **Figure 5-14**).

TRBV assessments also demonstrated polyclonality in all populations (**Figure 5-19**). This is, however, a contentious claim as there is no widely accepted cutoff for oligoclonality/polyclonality. A2-induced populations especially showed markedly different TRBV compositions. Moreover, testing for clonality with flow cytometry is limited to antibody binding to ~15 variants of the Vβ-chain of the TCR. Therefore, different clones using the same Vβ-chain, but exhibiting potentially very different structural avidity get grouped together, obscuring true clonality. Modern sequencing methods are able to paint a vastly more detailed picture of clonality and could have shown a more diverse clonal landscape in these experiments. For the purposes of this project, however, Vβ-chain staining sufficed to exclude monoclonality by demonstrating heterogenous Vβ-chain usage. The populations therefore served as a good model for polyclonal T-cell responses.

A noteworthy difference between groups was the frequency of cognate multimer-binding T cells depending on the infecting strain (**Figure 5-10**). The reasons for this are unclear. Potential factors are possible differences in the immunogenicity between OVA and the APLs. APLs can reportedly lead to higher or lower stability of the pMHC complex at the cell surface leading to size differences in the responding $CD8^+$ T-cell populations (Slansky et al. 2000; Shorter et al. 2016). However, a report using alanine substitutes to probe pMHC stability has found, *e.g.*, H-$2k^b$/SAINFEKL (A2) to be as stable as H-$2k^b$/OVA (Jameson und Bevan 1992). Differences in the quality of the refolded pMHC molecules used as staining agents could also influence the frequency of T cells binding to the multimers leading to under- or overestimation of the antigen-specific population. Notwithstanding, the frequencies of OVA $Mult^+$ cells in the APL-induced T-cell populations (especially in the A2-induced populations as they show similar frequencies of $Mult^+$ cells when stained with A2/OVA Mult) hint at a correct detection of the frequency of APL-specific T cells by cognate multimer staining (**Figure 5-16**, **Figure 5-17**). Lastly, differences in the virulence of the strains despite their common ancestry could not be excluded as a reason for the difference in frequency of the antigen-specific $CD8^+$ T-cell response. The difference in frequency of cognate multimer-binding T cells is, however, not expected to have an influence on the relationship between the global k_{off}-rate and functional aspects.

6.2.1 Structural avidity of OVA- or APL-induced CD8⁺ T-cell populations

The APL and OVA-induced CD8⁺ T-cell populations exhibited very comparable global k_{off}-rates (**Figure 5-12**, **Figure 5-14**). This underscored that the APL-induced populations did not carry TCRs of generally lower structural avidity. All groups showed a trend towards an increase in structural avidity towards their cognate epitope in the recall setting pointing towards avidity maturation (**Figure 5-15**). When tested against the OVA epitope, however, they did robustly show faster global k_{off}-rates (**Figure 5-13**, **Figure 5-14**).

Surprisingly, A2-induced populations showed no significant difference in global k_{off}-rates towards the OVA epitope compared to the OVA-induced populations. This is congruent with the observation that the vast majority of A2 multimer stainable CD8⁺ T cells were cross-reactive, *i.e.*, could also be stained with OVA multimer (**Figure 5-16**, **Figure 5-17**, **Figure 5-18**). This points towards a subordinate role of the first isoleucine of the SIINFEKL peptide in the binding of H-2k^b/OVA multimers to TCRs. In line with this, substituting isoleucine for alanine is often considered to be a relatively inert change as alanine, too, is hydrophobic and has a short chemical residue. The marked difference in Vβ-chain distributions in the A2 vs. OVA groups do, however, show that the two peptides recruit different TCRs. While the reasons for the consistently similar structural avidity of both groups towards OVA despite their differences in the TCR composition remains unclear, it represents an excellent internal control for the APL-OVA model at large. This is because any functional differences observed in the A2-induced populations compared to the OVA-induced populations were putatively due to particularities of the APL system itself instead of differences in structural avidity.

Q4-induced populations were hard to probe for structural avidity towards OVA as they showed very low frequencies of cross-reactive OVA multimer-binding T cells (**Figure 5-16**, **Figure 5-17**, **Figure 5-18**). Q4-induced populations with sizable OVA multimer-binding subpopulations did show very fast OVA MHC dissociation kinetics, but background noise was too intense for accurate k_{off}-rate quantification (data not shown). This points towards Q4-induced populations being of very low structural avidity towards OVA, but low frequencies of cross-reactive T cells and differences in their phenotypic composition warrant caution when assuming low structural avidity and interpreting functional differences in this population.

Y3-induced populations allowed for the best comparison of levels of structural avidity as they were well measurable with OVA reagents and robustly showed a significantly faster global k_{off}-rate compared with OVA or A2-induced populations (**Figure 5-13**, **Figure 5-14**). Therefore, many experiments focused on the comparison of the well-measurable OVA, A2, and Y3 groups with Q4 as additional low-avidity group where assays and cell numbers allowed.

While having 3-4 groups represent the broad spectrum of avidity is a limitation for the validity of this project, this number of groups is as large as the scope of the project allowed and more representative of physiological avidity distribution than many previous works on TCR avidity utilizing few monoclonal populations of differing avidity (Gannon et al. 2015; Allard et al. 2017). Moreover, the direct measurement of the global k_{off}-rate and correlation with functional parameters of every single T-cell population (see below) confirms the trends seen in the other experiments and gives much more granular insights beyond the group clusters.

Overall, the APL-OVA infection setup served as a model for otherwise comparable physiological CD8⁺ T-cell populations of robustly tiered global k_{off}-rates towards the OVA epitope which provided the basis for experiments on the relationship between structural avidity and functionality.

6.2.2 Functional avidity of OVA-/APL-induced CD8⁺ T-cell populations

Peptide sensitivity, *i.e.*, the concentration of a peptide stimulus at which 50% of a T-cell population will produce cytokines (EC_{50}, also called 'functional avidity'), is often used as the primary in vitro readout to approximate the population's effector capacity in vivo and has been

linked to structural avidity multiple times (Viganò et al. 2012). The EC_{50} as the average measure of peptide sensitivity in a heterogenous, polyclonal T-cell population also conceptually overlaps with the idea of the global k_{off}-rate as an average measure of structural avidity. Therefore, it particularly lent itself to establishing a correlation between global k_{off}-rate and functionality. The production of IFN-γ was chosen as readout because it is readily produced by $CD8^+$ T cells. Increasingly, the production of multiple cytokines is used as a more comprehensive readout, but this was outside of the scope of this work.

The OVA-/APL-induced populations were firstly stimulated with the inducing epitope and showed similar EC_{50} values (**Figure 5-20**). This underscored that the APL-induced populations were not of generally lower functional avidity compared to the OVA-induced populations.

The frequency of $CD8^+$ T cells producing IFN-γ when stimulated with the highest concentration of cognate peptide was lower than the frequency of cognate multimer binding $CD8^+$ T cells across all groups (compare **Figure 5-20** and **Figure 5-10**). This phenomenon has been previously observed, is highly variable depending on infection setting, time points, as well as the concentration of the reagents, and is in part due to exhaustion of antigen-specific T cells (Wooldridge et al. 2009). The ratio of IFN-γ-producing $CD8^+$ T cells over multimer-binding $CD8^+$ T cells was variable within groups, but the average ratio was consistently around 0.5-0.6 for all groups, epitopes, combinations, and infection settings (data not shown). This limits the validity of the association between global k_{off}-rate and functional avidity as only ~50% of the cells that participated in the k_{off}-rate measurements, *i.e.,* multimer-binding cells, seemed to produce IFN-γ. It would be interesting to identify the subgroup of IFN-γ-producing during k_{off}-rate measurements and compare their global k_{off}-rate to that of the non-IFN-γ-producing subgroup. Unfortunately, multimer staining was not possible after peptide stimulation due to TCR downregulation (data not shown), making these subgroups extremely hard to study. Lastly, the IFN-γ-producing $CD8^+$ T cells and multimer-binding $CD8^+$ T cells were not formally shown to overlap as no cell-sorting was used prior to peptide stimulation. Though the overlap is presumed to be very large as previous works have shown (Wooldridge et al. 2009), this further restricts the conclusiveness of the results.

When stimulated with the OVA epitope, the OVA-/APL-induced $CD8^+$ T-cell populations exhibited highly significant and very robust differences in functional avidity (**Figure 5-20**). These differences could not be explained by differences in phenotypic composition or frequency of naïve T cells between groups (**Figure 5-21**). These results provided strong evidence that a higher structural avidity of a T-cell population also translated to higher functional avidity. To get a more detailed view of the correlation between structural and functional avidity, peptide stimulation assays and TCR-ligand k_{off}-rate assays were performed simultaneously for the same populations with the same epitopes. Indeed, both parameters showed a significant positive correlation in both the primary and secondary infection setting (**Figure 5-22**).

The primary and secondary infection settings do however display some variability in the extent of the correlation. The primary infection setting shows a more linear relationship whereas the secondary infection setting displays a flipped “L”-shaped correlation suggesting a structural avidity threshold of $t_{1/2}$ around 15s beyond which all populations exhibit high functionality (**Figure 5-22**). In the recall setting, however, the points clustered around a cognate epitope and a foreign epitope group (*e.g.*, the Y3-induced populations exclusively displayed values at the upper end of the spectrum when measured with the Y3 epitope and displayed values at the lower end when measured with the OVA epitope). This makes the correlation more susceptible to inter-group variation and bias (**Figure 5-22**). The reason for the structural and functional ‘focus’ on the cognate epitope might again be due to avidity maturation and subsequent narrowing of the TCR repertoire, leading to less cross-reactivity towards foreign epitopes. However, there is some evidence suggesting the opposite in very specific circumstances (van den Boorn et al. 2006). Moreover, A2-induced populations still consistently displayed high values with both OVA and A2 epitopes, leaving the reasons for the discrepancy between the shape of the correlations ultimately unclear.

The subgroup of OVA-induced populations in this correlation is of particular interest. Their structural and functional avidity toward the A2 and Y3 epitopes cluster surprisingly closely with the flipped combination of APL-induced populations measured against the OVA epitope (**Figure 5-22**). This corroborates the link between structural and functional avidity previously seen in the APL-induced populations. It also supports the hypothesis that the combination of APL-induced populations tested against the OVA epitope is representative of a broad range of antigen-specific populations and epitopes. The degree to which the inducing epitope and the epitope used in the k_{off}-rate/functional assays seemed to be interchangeable to receive similar results was nevertheless astounding.

The particular order and tiering of functional and structural avidity of the groups towards the OVA epitope and those of the OVA-induced populations towards APL epitopes was reminiscent of the order of the APLs' ability to stimulate the OT-1 TCR (Zehn et al. 2009). This provided external validation of the herein acquired data and hinted at a representativity of the OT-1 TCR and APL system in terms of cross-reactivity. More studies into the comparability of the OT-1/APL system and the herein established OVA/APL system are warranted. Likewise, the more physiological approach of the latter paired with its ease of establishment and availability may contribute to further research in this field.

6.3 Tumor killing capacity in vitro and in vivo

To test whether the findings on functionality also held true for tumor killing and protection, OVA-expressing tumors were used as target cells in in vitro and in vivo experiments.

For all experiments, fixed cell numbers of OVA streptamer-binding $CD8^+$ T cells were sorted from the APL-/OVA-induced populations to compensate for their significant differences in frequencies of OVA-specific T cells. Limitingly, the intermediate sorting step made the following results less comparable with those from the peptide sensitivity assays, because the populations under study were streptamer-binding $CD8^+$ T cells only instead of bulk splenocytes. Moreover, Q4-induced populations harbored too few OVA streptamer-binding $CD8^+$ T cells to include in these experiments. An alternative approach to potentially isolate higher numbers of OVA-specific T cells was magnetic separation. However, preliminary experiments yielded many more apoptotic cells and contamination with other cell types as compared to cell sorting with flow cytometry, which would have introduced more confounding factors. Therefore, the latter method was chosen even though this meant that Q4-induced populations could not be included in the experiments.

6.3.1 In vitro tumor killing and its link to global k_{off}-rates

Tumor killing was assessed with the xCELLigence assay which allows for real-time analysis of cytolysis via confluence and adherence of the target cells. The MC38OVA cell line, which was used in the in vivo experiments, was tested for the xCELLigence assay, but did not show a stable enough signal of confluence and adherence (data not shown). Therefore, PancOVA tumor target cells were chosen because of their ability to adhere to the bottom of the wells of the special microtiter plates. Moreover, T cells from recall populations were used in the in vitro setting for higher cell numbers as opposed to the in vivo experiments which featured cells from primary infections. This limits the comparability of the results of the in vitro and in vivo settings.

The difference in the cell indices between the control wells and the wells to which the OVA streptamer-sorted $CD8^+$ T cells were added was assessed after 48h and quantified as cytolysis in percent (**Figure 5-24**). However, as the cell index is a unitless number, a true percentage of tumor cells killed cannot be acquired using this methodology. Caution is warranted especially when comparing groups with small differences in the cytolysis values.

T cells sorted from the OVA- and the A2-induced recall populations led to stark cytolysis at both effector-to-target ratios whereas the cells derived from the Y3-induced recall populations facilitated little to no cytolysis of the OVA-expressing tumor cells. The non-significant difference

between the A2 and the OVA group and the highly significant difference between them both compared to the Y3 group mirrored the results from the peptide sensitivity and TCR-ligand k_{off}-rate assays. The correlation with the corresponding global k_{off}-rates was positive and highly significant for both E:T ratios and closely reflected the correlation found in the peptide sensitivity assays in the recall setting. These results strongly corroborated the results from the peptide sensitivity assays and strengthened the link between global k_{off}-rates and functional parameters.

Another limitation of the xCELLigence assay was the relatively high inter-experiment variability of tumor cell growth. This was likely in part due to the growth behavior of the PancOVA cell line as it seemed to decrease its doubling time slightly with every splitting procedure of the cell line in cell culture (data not shown), leading to less pronounced differences between control/treatment wells in later experiments. Moreover, due to the high temperature sensitivity of the confluence of the tumor cell lines, small perturbations during the experiments (like the frequent use of the incubator), could have led to differences in the growth kinetics. However, as the readout was set relative to control wells running in parallel, cytolysis after 48h was very comparable between experiments.

Further experiments with different cell lines and other tumor-killing assays like the Chromium- or Europium-release assays could have lend more validity to these results. However, issues of accessibility and time restraints put such experiments out of the scope of this work.

6.3.2 In vivo protection from OVA-expressing tumor cells

In vivo protection was tested in mice via irradiation, same-day adoptive transfer of OVA streptamer-sorted T cells, and subcutaneous tumor graft one day later.

The irradiation of the otherwise immunocompetent mice was critical for tumor engraftment and for the attributability of the anti-tumor effect to the adoptively transferred T cells as it severely immunocompromises the host (Kajioka et al. 2000). This immunodepletion prior to adoptive T-cell transfer might have had increased the observed effect size compared to a non-irradiated setting, but was deemed an adequate intervention in these experiments as it is a common intervention in clinical practice to improve effectiveness, *e.g.*, via lymphodepleting chemotherapy prior to CAR-T-cell infusion (Fabrizio et al. 2022).

The protection from tumor growth differed significantly between all groups (all-curve difference), but sample size and effect size were not large enough to achieve significance between individual groups. However, a trend in the survival curves and median survival of the OVA and A2 groups and the Y3 and the control groups could be observed. This trend mirrored the group differences observed in the in vitro tumor killing, peptide sensitivity, and TCR-ligand k_{off}-rate assays (**Figure 5-25**).

A probable reason for the less pronounced effect compared to the abovementioned assays was that the adoptively transferred cells were derived from primary infections. Most of the transferred T cells likely died shortly thereafter as T-cell populations rapidly contract ~7 days after an acute *L.m.* infection. Therefore, the protection from the OVA-expressing tumors was likely conferred by only a small number of T cells and did not usually lead to tumor clearance. Higher cell numbers or T cells of a different phenotypic composition could presumably confer superior protection and demonstrate a more pronounced difference in the survival curves. However, experiments with larger recall T-cell populations were not feasible due to time constraints. Likewise, simultaneous measurements of global k_{off}-rates were not possible due to insufficient cell numbers as all splenocytes were consumed during cell sorting.

Despite the modest difference between groups and the lack of granular global k_{off}-rate data on each transferred T-cell population, the results fit seamlessly into the previously acquired data on functionality. Previous works have established the link between TCR-ligand k_{off}-rates (as measured by our streptamer-based assay) and protective capacity in vivo for monoclonal $CD8^+$ T cells (Nauerth et al. 2013). These data reaffirm this link and extend it to polyclonal

populations. Such results are a prerequisite for clinical applications and provide a rationale for further investigations into TCR-ligand avidity in T-cell therapeutics.

6.4 Global k_{off}-rates of human polyclonal T-cell populations and their predictability from constituent T-cell clones

The link between functionality and global k_{off}-rates from the abovementioned experiments was established in murine polyclonal T-cell populations. A similar link was to be expected in human polyclonal T-cell populations as TCR-ligand k_{off}-rates and functionality were similarly found to correlate in human T-cell lines and clones (Nauerth et al. 2013; Allard et al. 2017; Hombrink et al. 2013). The previously published work showcasing the double multimer staining and ex vivo TCR-ligand k_{off}-rate measurements did already feature the measurement of two very small virus-specific $CD8^+$ T-cell populations (Nauerth et al. 2016). However, the acquired dissociation kinetics were highly monomorphic and not tested for clonality. It is therefore unclear whether these examples represented measurements of global k_{off}-rates of polyclonal T-cell populations.

To analyze global k_{off}-rates of polyclonal $CD8^+$ T-cell populations more rigorously, YFV-specific $CD8^+$ T cells of T_{scm} phenotype were sorted from a blood sample of a YFV-vaccinated donor and single-cell expanded. The arising clones were then uniquely color coded, pooled, and stained for the TCR-ligand k_{off}-rate assay. After the measurement, the color codes allowed for the identification of all clones so that the global k_{off}-rate of the mixed, 'polyclonal' population, as well as the k_{off}-rate of each individual clone, could be analyzed.

The mode of analysis however differed from the murine setting: As detailed in section 5.1.3, the pMHC molecules in the human setting are often subject to quenching, subduing the pMHC MFI before the start of the dissociation (nicely visible in **Figure 5-27**B, clone k). Unlike the standard for murine measurements, the initial MFI could therefore not be used as starting value of the dissociation. Therefore, the unconstrained one-phase decay after exclusion of pre-dissociation data had to be chosen as the mode of analysis. This was the standard for human k_{off}-rates in our group and was consistent with the methods used in (Nauerth et al. 2016). Limitingly, this divergence in the mode of analysis made the absolute $t_{1/2}$ values less comparable between the human and the murine setting. This technical difference might be resolvable with different reagents in the human setting. Unlabeled Strep-Tactin protein is available for purchase and might eliminate the quenching of the pHLA molecules. Moreover, novel approaches for production of pHLA molecules are being developed (Effenberger et al. 2019), possibly ameliorating or eliminating quenching, enabling the incorporation of the initial MFI into the human k_{off}-rate analysis.

The global $t_{1/2}$ of a simulated human biclonal population very closely matched the arithmetic mean of the $t_{1/2}$ of the constituent clones, mirroring the results of the murine setting (**Figure 5-27**). Simulations with more clones at different frequencies confirmed that in both settings alike subclonal avidities contribute to the global k_{off}-rate linearly (according to their frequency), equitably (high- and low-avidity clones contribute equally), and without confounding phenomena. To validate the results from this one experiment, the analysis was repeated on data of 7 human TCRs specific for HLA-A2/$pp65_{495\text{-}503}$ from a TCR library. The equation predictions yielded the very same results of very high fidelity and overlap with the dissociation fit output (data not shown, refer to supplementary information of (Lückemeier et al. 2022) for graphs and details).

Limitingly, the precision of predictions of the global k_{off}-rates will likely be less accurate when applied to mixing cell products from pre-characterized TCRs in TCR libraries or cell banks. This is because of assay-related fluctuations around the 'real' k_{off}-rate of each clone during the global k_{off}-rate measurement, which will scale with the number of clones added to the mixed population. However, this should be alleviated by repeat measurements of the global k_{off}-rate and constitute only a small deviation from the predicted value as inter-measurement variations are low for the streptamer-based TCR-ligand k_{off}-rate assay.

These data demonstrated that the model equation accurately reflected how global k_{off}-rates merge from subclonal k_{off}-rates. It thereby unveiled a methodology to compose oligo- to polyclonal T-cell populations with a planned global k_{off}-rate from well characterized T-cell clones, *e.g.*, from a TCR library. Taken together with the substantial correlations of global k_{off}-rates with several functional parameters, this created a strong rationale for the design of polyclonal T-cell products.

However, to thoroughly proof the predictability of the global k_{off}-rate and its associated functionality of manually mixed polyclonal T-cell products from pre-characterized TCRs, more experiments are needed. Mixing T-cell clones from a TCR library at different frequencies, measuring their functionality in conjunction with their global k_{off}-rates and comparing those to the predicted values and established correlations would greatly enhance the impact of the findings of this project. This was, however, outside the scope of this work and requires further studies.

TCR-transgenic T-cell transfer is an increasingly popular approach to specifically target cancerous cells and viral reactivations and important advances to facilitate these therapies have recently been made (Schober et al. 2020a). A multitude of clinical trials utilizing transgenic TCR T-cell products with well-characterized TCRs specific for a plethora of epitopes are currently ongoing. To the best of our knowledge, none of these trials are investigating more than one TCR with the same specificity. However, this approach might offer advantages by combining the roles and functionalities of T cells with high and low TCR-ligand avidity: High-avidity transgenic T cells initially provide strong efficacy against the target cells, but might be prone to exhaustion due to chronic antigen exposure (Schober et al. 2020b), which is particularly pertinent in the fields in which T-cell therapy shows most promise: cancer and viral reactivation. Therefore, a transfer of a bi- or polyclonal T-cell product which includes lower-avidity T cells might lead to more durable responses. Moreover, lower-avidity antigen receptors were shown to confer less on-target/off-tumor toxicity (Caruso et al. 2015; Park et al. 2017), while higher avidity is usually associated with superior efficacy, highlighting the potential for synergies within mixed-avidity T-cell products.

The findings in this work could prove critical in the design process of T-cell products from multiple previously characterized TCRs and in evaluating their global k_{off}-rates to aid in striking the right balance of TCR avidity.

7. Bibliography

Allard, Mathilde; Couturaud, Barbara; Carretero-Iglesia, Laura; Duong, Minh Ngoc; Schmidt, Julien; Monnot, Gwennaëlle C. et al. (2017): TCR-ligand dissociation rate is a robust and stable biomarker of CD8+ T cell potency. In: *JCI insight* 2 (14). DOI: 10.1172/jci.insight.92570.

Ashton-Rickardt, P. G.; Bandeira, A.; Delaney, J. R.; van Kaer, L.; Pircher, H. P.; Zinkernagel, R. M.; Tonegawa, S. (1994): Evidence for a differential avidity model of T cell selection in the thymus. In: *Cell* 76 (4), S. 651–663. DOI: 10.1016/0092-8674(94)90505-3.

Buchholz, Veit R.; Flossdorf, Michael; Hensel, Inge; Kretschmer, Lorenz; Weissbrich, Bianca; Gräf, Patricia et al. (2013): Disparate individual fates compose robust CD8+ T cell immunity. In: *Science (New York, N.Y.)* 340 (6132), S. 630–635. DOI: 10.1126/science.1235454.

Busch, D. H.; Pamer, E. G. (1999): T cell affinity maturation by selective expansion during infection. In: *The Journal of experimental medicine* 189 (4), S. 701–710. DOI: 10.1084/jem.189.4.701.

Call, Matthew E.; Pyrdol, Jason; Wiedmann, Martin; Wucherpfennig, Kai W. (2002): The Organizing Principle in the Formation of the T Cell Receptor-CD3 Complex. In: *Cell* 111 (7), S. 967–979. DOI: 10.1016/s0092-8674(02)01194-7.

Carreno, Beatriz M.; Magrini, Vincent; Becker-Hapak, Michelle; Kaabinejadian, Saghar; Hundal, Jasreet; Petti, Allegra A. et al. (2015): Cancer immunotherapy. A dendritic cell vaccine increases the breadth and diversity of melanoma neoantigen-specific T cells. In: *Science (New York, N.Y.)* 348 (6236), S. 803–808. DOI: 10.1126/science.aaa3828.

Carretero-Iglesia, Laura; Couturaud, Barbara; Baumgaertner, Petra; Schmidt, Julien; Maby-El Hajjami, Hélène; Speiser, Daniel E. et al. (2019): High Peptide Dose Vaccination Promotes the Early Selection of Tumor Antigen-Specific CD8 T-Cells of Enhanced Functional Competence. In: *Frontiers in immunology* 10, S. 3016. DOI: 10.3389/fimmu.2019.03016.

Caruso, Hillary G.; Hurton, Lenka V.; Najjar, Amer; Rushworth, David; Ang, Sonny; Olivares, Simon et al. (2015): Tuning Sensitivity of CAR to EGFR Density Limits Recognition of Normal Tissue While Maintaining Potent Antitumor Activity. In: *Cancer research* 75 (17), S. 3505–3518. DOI: 10.1158/0008-5472.CAN-15-0139.

Chen, Lieping; Flies, Dallas B. (2013): Molecular mechanisms of T cell co-stimulation and co-inhibition. In: *Nature reviews. Immunology* 13 (4), S. 227–242. DOI: 10.1038/nri3405.

Cole, David K.; Pumphrey, Nicholas J.; Boulter, Jonathan M.; Sami, Malkit; Bell, John I.; Gostick, Emma et al. (2007): Human TCR-binding affinity is governed by MHC class restriction. In: *Journal of immunology (Baltimore, Md. : 1950)* 178 (9), S. 5727–5734. DOI: 10.4049/jimmunol.178.9.5727.

Corr, M.; Slanetz, A. E.; Boyd, L. F.; Jelonek, M. T.; Khilko, S.; al-Ramadi, B. K. et al. (1994): T cell receptor-MHC class I peptide interactions: affinity, kinetics, and specificity. In: *Science (New York, N.Y.)* 265 (5174), S. 946–949. DOI: 10.1126/science.8052850.

Crawford, Frances; Kozono, Haruo; White, Janice; Marrack, Philippa; Kappler, John (1998): Detection of Antigen-Specific T Cells with Multivalent Soluble Class II MHC Covalent Peptide Complexes. In: *Immunity* 8 (6), S. 675–682. DOI: 10.1016/S1074-7613(00)80572-5.

Davis, Simon J.; van der Merwe, P. Anton (2011): Lck and the nature of the T cell receptor trigger. In: *Trends in immunology* 32 (1), S. 1–5. DOI: 10.1016/j.it.2010.11.003.

Effenberger, Manuel (2020): Isolation, Characterization and Functional Re-Expression of T Cell Receptors with Therapeutic Value for Adoptive T Cell Therapy. Dissertation. Technische Universität München, München.

Effenberger, Manuel; Stengl, Andreas; Schober, Kilian; Gerget, Maria; Kampick, Maximilian; Müller, Thomas R. et al. (2019): FLEXamers: A Double Tag for Universal Generation of Versatile Peptide-MHC Multimers. In: *Journal of immunology (Baltimore, Md. : 1950)* 202 (7), S. 2164–2171. DOI: 10.4049/jimmunol.1801435.

Fabrizio, Vanessa A.; Boelens, Jaap Jan; Mauguen, Audrey; Baggott, Christina; Prabhu, Snehit; Egeler, Emily et al. (2022): Optimal fludarabine lymphodepletion is associated with improved outcomes after CAR T-cell therapy. In: *Blood advances* 6 (7), S. 1961–1968. DOI: 10.1182/bloodadvances.2021006418.

Felix, Nathan J.; Allen, Paul M. (2007): Specificity of T-cell alloreactivity. In: *Nature reviews. Immunology* 7 (12), S. 942–953. DOI: 10.1038/nri2200.

Fife, Brian T.; Bluestone, Jeffrey A. (2008): Control of peripheral T-cell tolerance and autoimmunity via the CTLA-4 and PD-1 pathways. In: *Immunological Reviews* 224 (1), S. 166–182. DOI: 10.1111/j.1600-065X.2008.00662.x.

Fuertes Marraco, Silvia A.; Soneson, Charlotte; Cagnon, Laurène; Gannon, Philippe O.; Allard, Mathilde; Abed Maillard, Samia et al. (2015): Long-lasting stem cell-like memory CD8+ T cells with a naïve-like profile upon yellow fever vaccination. In: *Science translational medicine* 7 (282), 282ra48. DOI: 10.1126/scitranslmed.aaa3700.

Gannon, Philippe O.; Wieckowski, Sébastien; Baumgaertner, Petra; Hebeisen, Michaël; Allard, Mathilde; Speiser, Daniel E.; Rufer, Nathalie (2015): Quantitative TCR:pMHC Dissociation Rate Assessment by NTAmers Reveals Antimelanoma T Cell Repertoires Enriched for High Functional Competence. In: *Journal of immunology (Baltimore, Md. : 1950)* 195 (1), S. 356–366. DOI: 10.4049/jimmunol.1403145.

Garcia, K. C.; Scott, C. A.; Brunmark, A.; Carbone, F. R.; Peterson, P. A.; Wilson, I. A.; Teyton, L. (1996): CD8 enhances formation of stable T-cell receptor/MHC class I molecule complexes. In: *Nature* 384 (6609), S. 577–581. DOI: 10.1038/384577a0.

Gáspár, R.; Bagossi, P.; Bene, L.; Matkó, J.; Szöllosi, J.; Tozsér, J. et al. (2001): Clustering of class I HLA oligomers with CD8 and TCR: three-dimensional models based on fluorescence resonance energy transfer and crystallographic data. In: *Journal of immunology (Baltimore, Md. : 1950)* 166 (8), S. 5078–5086. DOI: 10.4049/jimmunol.166.8.5078.

Grommé, Monique; Neefjes, Jacques (2002): Antigen degradation or presentation by MHC class I molecules via classical and non-classical pathways. In: *Molecular Immunology* 39 (3-4), S. 181–202. DOI: 10.1016/s0161-5890(02)00101-3.

Hamad, A. R.; O'Herrin, S. M.; Lebowitz, M. S.; Srikrishnan, A.; Bieler, J.; Schneck, J.; Pardoll, D. (1998): Potent T cell activation with dimeric peptide-major histocompatibility complex class II ligand: the role of CD4 coreceptor. In: *The Journal of experimental medicine* 188 (9), S. 1633–1640. DOI: 10.1084/jem.188.9.1633.

Hayday, A. C. (2000): gammadelta cells: a right time and a right place for a conserved third way of protection. In: *Annual review of immunology* 18, S. 975–1026. DOI: 10.1146/annurev.immunol.18.1.975.

He, Xiao; He, Xi; Dave, Vibhuti P.; Zhang, Yi; Hua, Xiang; Nicolas, Emmanuelle et al. (2005): The zinc finger transcription factor Th-POK regulates CD4 versus CD8 T-cell lineage commitment. In: *Nature* 433 (7028), S. 826–833. DOI: 10.1038/nature03338.

Hebeisen, Michael; Schmidt, Julien; Guillaume, Philippe; Baumgaertner, Petra; Speiser, Daniel E.; Luescher, Immanuel; Rufer, Nathalie (2015): Identification of Rare High-Avidity, Tumor-Reactive CD8+ T Cells by Monomeric TCR-Ligand Off-Rates Measurements on Living Cells. In: *Cancer research* 75 (10), S. 1983–1991. DOI: 10.1158/0008-5472.CAN-14-3516.

Hofmann, Susanne; Schmitt, Michael; Götz, Marlies; Döhner, Hartmut; Wiesneth, Markus; Bunjes, Donald; Greiner, Jochen (2019): Donor lymphocyte infusion leads to diversity of specific T cell responses and reduces regulatory T cell frequency in clinical responders. In: *International journal of cancer* 144 (5), S. 1135–1146. DOI: 10.1002/ijc.31753.

Hombrink, Pleun; Raz, Yotam; Kester, Michel G. D.; Boer, Renate de; Weißbrich, Bianca; Borne, Peter A. von dem et al. (2013): Mixed functional characteristics correlating with TCR-ligand koff -rate of MHC-tetramer reactive T cells within the naive T-cell repertoire. In: *European journal of immunology* 43 (11), S. 3038–3050. DOI: 10.1002/eji.201343397.

Hu, Zhuting; Leet, Donna E.; Allesøe, Rosa L.; Oliveira, Giacomo; Li, Shuqiang; Luoma, Adrienne M. et al. (2021): Personal neoantigen vaccines induce persistent memory T cell responses and epitope spreading in patients with melanoma. In: *Nature medicine* 27 (3), S. 515–525. DOI: 10.1038/s41591-020-01206-4.

Huang, Jun; Zarnitsyna, Veronika I.; Liu, Baoyu; Edwards, Lindsay J.; Jiang, Ning; Evavold, Brian D.; Zhu, Cheng (2010): The kinetics of two-dimensional TCR and pMHC interactions determine T-cell responsiveness. In: *Nature* 464 (7290), S. 932–936. DOI: 10.1038/nature08944.

Huppa, Johannes B.; Axmann, Markus; Mörtelmaier, Manuel A.; Lillemeier, Björn F.; Newell, Evan W.; Brameshuber, Mario et al. (2010): TCR-peptide-MHC interactions in situ show accelerated kinetics and increased affinity. In: *Nature* 463 (7283), S. 963–967. DOI: 10.1038/nature08746.

Jacobs, Collin; Duewell, Peter; Heckelsmiller, Klaus; Wei, Jiwu; Bauernfeind, Franz; Ellermeier, Jonathan et al. (2011): An ISCOM vaccine combined with a TLR9 agonist breaks immune evasion mediated by regulatory T cells in an orthotopic model of pancreatic carcinoma. In: *International journal of cancer* 128 (4), S. 897–907. DOI: 10.1002/ijc.25399.

Jameson, S. C.; Bevan, M. J. (1992): Dissection of major histocompatibility complex (MHC) and T cell receptor contact residues in a Kb-restricted ovalbumin peptide and an assessment of the predictive power of MHC-binding motifs. In: *European journal of immunology* 22 (10), S. 2663–2667. DOI: 10.1002/eji.1830221028.

Jönsson, Peter; Southcombe, Jennifer H.; Santos, Ana Mafalda; Huo, Jiandong; Fernandes, Ricardo A.; McColl, James et al. (2016): Remarkably low affinity of CD4/peptide-major histocompatibility complex class II protein interactions. In: *Proceedings of the National Academy of Sciences of the United States of America* 113 (20), S. 5682–5687. DOI: 10.1073/pnas.1513918113.

Kajioka, Eric H.; Andres, Melba L.; Li, Jun; Wen Mao, Xiao; Moyers, Michael F.; Nelson, Gregory A. et al. (2000): Acute Effects of Whole-Body Proton Irradiation on the Immune System of the Mouse. In: *Radiation Research* 153 (5), S. 587–594. DOI: 10.1667/0033-7587(2000)153[0587:AEOWBP]2.0.CO;2.

Keller, Michael D.; Bollard, Catherine M. (2020): Virus-specific T-cell therapies for patients with primary immune deficiency. In: *Blood* 135 (9), S. 620–628. DOI: 10.1182/blood.2019000924.

Knall, Robert (2007): Direct ex vivo identification of individual antigen specific T-Cells with optimal avidity for protection. Dissertation. Technische Universität München, München. Fakultät Wissenschaftszentrum Weihenstephan.

Kolb, H. J.; Mittermuller, J.; Clemm, C.; Holler, E.; Ledderose, G.; Brehm, G. et al. (1990): Donor leukocyte transfusions for treatment of recurrent chronic myelogenous leukemia in marrow transplant patients. In: *Blood* 76 (12), S. 2462–2465. DOI: 10.1182/blood.V76.12.2462.2462.

Lauer, Peter; Chow, Man Yin Nora; Loessner, Martin J.; Portnoy, Daniel A.; Calendar, Richard (2002): Construction, characterization, and use of two Listeria monocytogenes site-specific phage integration vectors. In: *Journal of bacteriology* 184 (15), S. 4177–4186. DOI: 10.1128/jb.184.15.4177-4186.2002.

Laugel, Bruno; van den Berg, Hugo A.; Gostick, Emma; Cole, David K.; Wooldridge, Linda; Boulter, Jonathan et al. (2007): Different T cell receptor affinity thresholds and CD8 coreceptor dependence govern cytotoxic T lymphocyte activation and tetramer binding properties. In: *The Journal of biological chemistry* 282 (33), S. 23799–23810. DOI: 10.1074/jbc.M700976200.

Lever, Melissa; Maini, Philip K.; van der Merwe, P. Anton; Dushek, Omer (2014): Phenotypic models of T cell activation. In: *Nature reviews. Immunology* 14 (9), S. 619–629. DOI: 10.1038/nri3728.

Liu, Baoyu; Zhong, Shi; Malecek, Karolina; Johnson, Laura A.; Rosenberg, Steven A.; Zhu, Cheng; Krogsgaard, Michelle (2014): 2D TCR-pMHC-CD8 kinetics determines T-cell responses in a self-antigen-specific TCR system. In: *European journal of immunology* 44 (1), S. 239–250. DOI: 10.1002/eji.201343774.

Lückemeier, Philipp; Molter, Katherine L.; Jarosch, Sebastian; Huppertz, Patrick; Purcarea, Anna; Effenberger, Manuel J. P. et al. (2022): Global koff -rates of polyclonal T-cell populations merge subclonal avidities and predict functionality. In: *European journal of immunology*. DOI: 10.1002/eji.202149597.

Luescher, I. F.; Vivier, E.; Layer, A.; Mahiou, J.; Godeau, F.; Malissen, B.; Romero, P. (1995): CD8 modulation of T-cell antigen receptor-ligand interactions on living cytotoxic T lymphocytes. In: *Nature* 373 (6512), S. 353–356. DOI: 10.1038/373353a0.

Majzner, Robbie G.; Mackall, Crystal L. (2018): Tumor Antigen Escape from CAR T-cell Therapy. In: *Cancer discovery* 8 (10), S. 1219–1226. DOI: 10.1158/2159-8290.CD-18-0442.

Martin-Blanco, N.; Blanco, R.; Alda-Catalinas, C.; Bovolenta, E. R.; Oeste, C. L.; Palmer, E. et al. (2018): A window of opportunity for cooperativity in the T Cell Receptor. In: *Nature communications* 9 (1), S. 2618. DOI: 10.1038/s41467-018-05050-6.

Martinez, Ryan J.; Andargachew, Rakieb; Martinez, Hunter A.; Evavold, Brian D. (2016): Low-affinity CD4+ T cells are major responders in the primary immune response. In: *Nature communications* 7, S. 13848. DOI: 10.1038/ncomms13848.

Martínez-Usatorre, Amaia; Donda, Alena; Zehn, Dietmar; Romero, Pedro (2018): PD-1 Blockade Unleashes Effector Potential of Both High- and Low-Affinity Tumor-Infiltrating T Cells. In: *Journal of immunology (Baltimore, Md. : 1950)* 201 (2), S. 792–803. DOI: 10.4049/jimmunol.1701644.

Matsushita, Hirokazu; Vesely, Matthew D.; Koboldt, Daniel C.; Rickert, Charles G.; Uppaluri, Ravindra; Magrini, Vincent J. et al. (2012): Cancer exome analysis reveals a T-cell-dependent mechanism of cancer immunoediting. In: *Nature* 482 (7385), S. 400–404. DOI: 10.1038/nature10755.

Maude, Shannon L.; Laetsch, Theodore W.; Buechner, Jochen; Rives, Susana; Boyer, Michael; Bittencourt, Henrique et al. (2018): Tisagenlecleucel in Children and Young Adults with B-Cell Lymphoblastic Leukemia. In: *The New England journal of medicine* 378 (5), S. 439–448. DOI: 10.1056/NEJMoa1709866.

Nagasaki, Joji; Inozume, Takashi; Sax, Nicolas; Ariyasu, Ryo; Ishikawa, Masakazu; Yamashita, Kazuo et al. (2022): PD-1 blockade therapy promotes infiltration of tumor-attacking exhausted T cell clonotypes. In: *Cell reports* 38 (5), S. 110331. DOI: 10.1016/j.celrep.2022.110331.

Nauerth, Magdalena (2012): Development of a novel TCR avidity assay for human CD8+ T cells. München, Technische Universität München, Diss., 2012. Universitätsbibliothek der TU München, München.

Nauerth, Magdalena; Stemberger, Christian; Mohr, Fabian; Weißbrich, Bianca; Schiemann, Matthias; Germeroth, Lothar; Busch, Dirk H. (2016): Flow cytometry-based TCR-ligand Koff -rate assay for fast avidity screening of even very small antigen-specific T cell populations ex vivo. In: *Cytometry. Part A : the journal of the International Society for Analytical Cytology* 89 (9), S. 816–825. DOI: 10.1002/cyto.a.22933.

Nauerth, Magdalena; Weißbrich, Bianca; Knall, Robert; Franz, Tobias; Dössinger, Georg; Bet, Jeannette et al. (2013): TCR-ligand koff rate correlates with the protective capacity of antigen-specific CD8+ T cells for adoptive transfer. In: *Science translational medicine* 5 (192), 192ra87. DOI: 10.1126/scitranslmed.3005958.

Neelapu, Sattva S.; Locke, Frederick L.; Bartlett, Nancy L.; Lekakis, Lazaros J.; Miklos, David B.; Jacobson, Caron A. et al. (2017): Axicabtagene Ciloleucel CAR T-Cell Therapy in Refractory Large B-Cell Lymphoma. In: *The New England journal of medicine* 377 (26), S. 2531–2544. DOI: 10.1056/NEJMoa1707447.

Neuenhahn, M.; Albrecht, J.; Odendahl, M.; Schlott, F.; Dössinger, G.; Schiemann, M. et al. (2017): Transfer of minimally manipulated CMV-specific T cells from stem cell or third-party donors to treat CMV infection after allo-HSCT. In: *Leukemia* 31 (10), S. 2161–2171. DOI: 10.1038/leu.2017.16.

Nguyen, Hoang Hiep; Park, Jeho; Kang, Sebyung; Kim, Moonil (2015): Surface plasmon resonance: a versatile technique for biosensor applications. In: *Sensors (Basel, Switzerland)* 15 (5), S. 10481–10510. DOI: 10.3390/s150510481.

Oliveira, Giacomo; Stromhaug, Kari; Klaeger, Susan; Kula, Tomasz; Frederick, Dennie T.; Le, Phuong M. et al. (2021): Phenotype, specificity and avidity of antitumour CD8+ T cells in melanoma. In: *Nature* 596 (7870), S. 119–125. DOI: 10.1038/s41586-021-03704-y.

OLS OMNI Life Science GmbH: Live Cell Analysis System xCELLigence. Hg. v. OLS OMNI Life Science GmbH. Online verfügbar unter https://www.ols-bio.de/products/live-cell-analysis-system-xcelligence#rtca-family.

Park, Spencer; Shevlin, Enda; Vedvyas, Yogindra; Zaman, Marjan; Park, Susan; Hsu, Yen-Michael S. et al. (2017): Micromolar affinity CAR T cells to ICAM-1 achieves rapid tumor elimination while avoiding systemic toxicity. In: *Scientific reports* 7 (1), S. 14366. DOI: 10.1038/s41598-017-14749-3.

Peter Patrick Huppertz (2016): Optimization of a Screening Platform for Finding Therapeutically Relevant T Cell Receptors.

Pope, C.; Kim, S. K.; Marzo, A.; Masopust, D.; Williams, K.; Jiang, J. et al. (2001): Organ-specific regulation of the CD8 T cell response to Listeria monocytogenes infection. In: *Journal of immunology (Baltimore, Md. : 1950)* 166 (5), S. 3402–3409. DOI: 10.4049/jimmunol.166.5.3402.

Rius, Cristina; Attaf, Meriem; Tungatt, Katie; Bianchi, Valentina; Legut, Mateusz; Bovay, Amandine et al. (2018): Peptide-MHC Class I Tetramers Can Fail To Detect Relevant Functional T Cell Clonotypes and Underestimate Antigen-Reactive T Cell Populations. In: *Journal of immunology (Baltimore, Md. : 1950)* 200 (7), S. 2263–2279. DOI: 10.4049/jimmunol.1700242.

Robert, Caroline; Long, Georgina V.; Brady, Benjamin; Dutriaux, Caroline; Maio, Michele; Mortier, Laurent et al. (2015): Nivolumab in previously untreated melanoma without BRAF mutation. In: *The New England journal of medicine* 372 (4), S. 320–330. DOI: 10.1056/NEJMoa1412082.

Rosenberg, S. A.; Packard, B. S.; Aebersold, P. M.; Solomon, D.; Topalian, S. L.; Toy, S. T. et al. (1988): Use of tumor-infiltrating lymphocytes and interleukin-2 in the immunotherapy of patients with metastatic melanoma. A preliminary report. In: *The New England journal of medicine* 319 (25), S. 1676–1680. DOI: 10.1056/NEJM198812223192527.

Rosenberg, Steven A.; Yang, James C.; Sherry, Richard M.; Kammula, Udai S.; Hughes, Marybeth S.; Phan, Giao Q. et al. (2011): Durable complete responses in heavily pretreated patients with metastatic melanoma using T-cell transfer immunotherapy. In: *Clinical cancer research : an official journal of the American Association for Cancer Research* 17 (13), S. 4550–4557. DOI: 10.1158/1078-0432.CCR-11-0116.

Sahin, Ugur; Derhovanessian, Evelyna; Miller, Matthias; Kloke, Björn-Philipp; Simon, Petra; Löwer, Martin et al. (2017): Personalized RNA mutanome vaccines mobilize poly-specific therapeutic immunity against cancer. In: *Nature* 547 (7662), S. 222–226. DOI: 10.1038/nature23003.

Sallusto, F.; Lenig, D.; Förster, R.; Lipp, M.; Lanzavecchia, A. (1999): Two subsets of memory T lymphocytes with distinct homing potentials and effector functions. In: *Nature* 401 (6754), S. 708–712. DOI: 10.1038/44385.

Savage, Peter A.; Boniface, J.Jay; Davis, Mark M. (1999): A Kinetic Basis For T Cell Receptor Repertoire Selection during an Immune Response. In: *Immunity* 10 (4), S. 485–492. DOI: 10.1016/S1074-7613(00)80048-5.

Saxena, Mansi; van der Burg, Sjoerd H.; Melief, Cornelis J. M.; Bhardwaj, Nina (2021): Therapeutic cancer vaccines. In: *Nature reviews. Cancer* 21 (6), S. 360–378. DOI: 10.1038/s41568-021-00346-0.

Schadendorf, Dirk; Hodi, F. Stephen; Robert, Caroline; Weber, Jeffrey S.; Margolin, Kim; Hamid, Omid et al. (2015): Pooled Analysis of Long-Term Survival Data From Phase II and Phase III Trials of Ipilimumab in Unresectable or Metastatic Melanoma. In: *Journal of clinical oncology : official journal of the American Society of Clinical Oncology* 33 (17), S. 1889–1894. DOI: 10.1200/JCO.2014.56.2736.

Schatz, David G.; Swanson, Patrick C. (2011): V(D)J recombination: mechanisms of initiation. In: *Annual review of genetics* 45, S. 167–202. DOI: 10.1146/annurev-genet-110410-132552.

Schmidt, Julien; Guillaume, Philippe; Irving, Melita; Baumgaertner, Petra; Speiser, Daniel; Luescher, Immanuel F. (2011): Reversible major histocompatibility complex I-peptide multimers containing Ni(2+)-nitrilotriacetic acid peptides and histidine tags improve

analysis and sorting of CD8(+) T cells. In: *The Journal of biological chemistry* 286 (48), S. 41723–41735. DOI: 10.1074/jbc.M111.283127.

Schober, Kilian; Müller, Thomas R.; Busch, Dirk H. (2020a): Orthotopic T-Cell Receptor Replacement-An "Enabler" for TCR-Based Therapies. In: *Cells* 9 (6). DOI: 10.3390/cells9061367.

Schober, Kilian; Voit, Florian; Grassmann, Simon; Müller, Thomas R.; Eggert, Joel; Jarosch, Sebastian et al. (2020b): Reverse TCR repertoire evolution toward dominant low-affinity clones during chronic CMV infection. In: *Nature immunology* 21 (4), S. 434–441. DOI: 10.1038/s41590-020-0628-2.

Schumacher, Ton N.; Schreiber, Robert D. (2015): Neoantigens in cancer immunotherapy. In: *Science (New York, N.Y.)* 348 (6230), S. 69–74. DOI: 10.1126/science.aaa4971.

Shimizu, Kenji; Sugiura, Daisuke; Okazaki, Il-Mi; Maruhashi, Takumi; Takemoto, Tatsuya; Okazaki, Taku (2021): PD-1 preferentially inhibits the activation of low-affinity T cells. In: *Proceedings of the National Academy of Sciences of the United States of America* 118 (35). DOI: 10.1073/pnas.2107141118.

Shorter, Shayla K.; Schnell, Frederick J.; McMaster, Sean R.; Pinelli, David F.; Andargachew, Rakieb; Evavold, Brian D. (2016): Viral Escape Mutant Epitope Maintains TCR Affinity for Antigen yet Curtails CD8 T Cell Responses. In: *PloS one* 11 (2), e0149582. DOI: 10.1371/journal.pone.0149582.

Sibener, Leah V.; Fernandes, Ricardo A.; Kolawole, Elizabeth M.; Carbone, Catherine B.; Liu, Fan; McAffee, Darren et al. (2018): Isolation of a Structural Mechanism for Uncoupling T Cell Receptor Signaling from Peptide-MHC Binding. In: *Cell* 174 (3), 672-687.e27. DOI: 10.1016/j.cell.2018.06.017.

Slansky, J. E.; Rattis, F. M.; Boyd, L. F.; Fahmy, T.; Jaffee, E. M.; Schneck, J. P. et al. (2000): Enhanced antigen-specific antitumor immunity with altered peptide ligands that stabilize the MHC-peptide-TCR complex. In: *Immunity* 13 (4), S. 529–538. DOI: 10.1016/s1074-7613(00)00052-2.

Snyder, Alexandra; Makarov, Vladimir; Merghoub, Taha; Yuan, Jianda; Zaretsky, Jesse M.; Desrichard, Alexis et al. (2014): Genetic basis for clinical response to CTLA-4 blockade in melanoma. In: *The New England journal of medicine* 371 (23), S. 2189–2199. DOI: 10.1056/NEJMoa1406498.

Sprent, J.; Tough, D. F. (2001): T cell death and memory. In: *Science (New York, N.Y.)* 293 (5528), S. 245–248. DOI: 10.1126/science.1062416.

Tian, Shaomin; Maile, Robert; Collins, Edward J.; Frelinger, Jeffrey A. (2007): CD8+ T cell activation is governed by TCR-peptide/MHC affinity, not dissociation rate. In: *Journal of immunology (Baltimore, Md. : 1950)* 179 (5), S. 2952–2960. DOI: 10.4049/jimmunol.179.5.2952.

van den Boorn, Jasper G.; Le Poole, I. Caroline; Luiten, Rosalie M. (2006): T-cell avidity and tuning: the flexible connection between tolerance and autoimmunity. In: *International reviews of immunology* 25 (3-4), S. 235–258. DOI: 10.1080/08830180600743081.

Viganò, Selena; Utzschneider, Daniel T.; Perreau, Matthieu; Pantaleo, Giuseppe; Zehn, Dietmar; Harari, Alexandre (2012): Functional avidity: a measure to predict the efficacy of effector T cells? In: *Clinical & developmental immunology* 2012, S. 153863. DOI: 10.1155/2012/153863.

Voit, Florian Maximilian (2021): Avidity dependent evolution of the T cell receptor repertoire during chronic viral infection. Dissertation. Technische Universität München, München. Fakultät für Medizin. Online verfügbar unter https://mediatum.ub.tum.de/603846?query=anna+purcarea&show_id=1596243&srcnodeid=603846, zuletzt geprüft am 07.06.2022.

Waldman, Alex D.; Fritz, Jill M.; Lenardo, Michael J. (2020): A guide to cancer immunotherapy: from T cell basic science to clinical practice. In: *Nature reviews. Immunology* 20 (11), S. 651–668. DOI: 10.1038/s41577-020-0306-5.

Weiden, P. L.; Flournoy, N.; Thomas, E. D.; Prentice, R.; Fefer, A.; Buckner, C. D.; Storb, R. (1979): Antileukemic effect of graft-versus-host disease in human recipients of allogeneic-marrow grafts. In: *The New England journal of medicine* 300 (19), S. 1068–1073. DOI: 10.1056/NEJM197905103001902.

Weißbrich, Bianca (2015): T cell receptor binding avidity of antigen-specific T cell receptor binding avidity of antigen-specific CD8+ cytotoxic T cells in chronic infection. Dissertation. Technische Universität München, München.

Wilde, Susanne; Sommermeyer, Daniel; Leisegang, Matthias; Frankenberger, Bernhard; Mosetter, Barbara; Uckert, Wolfgang; Schendel, Dolores J. (2012): Human antitumor CD8+ T cells producing Th1 polycytokines show superior antigen sensitivity and tumor recognition. In: *Journal of immunology (Baltimore, Md. : 1950)* 189 (2), S. 598–605. DOI: 10.4049/jimmunol.1102165.

Wooldridge, Linda; Lissina, Anna; Cole, David K.; van den Berg, Hugo A.; Price, David A.; Sewell, Andrew K. (2009): Tricks with tetramers: how to get the most from multimeric peptide-MHC. In: *Immunology* 126 (2), S. 147–164. DOI: 10.1111/j.1365-2567.2008.02848.x.

Zareie, Pirooz; Szeto, Christopher; Farenc, Carine; Gunasinghe, Sachith D.; Kolawole, Elizabeth M.; Nguyen, Angela et al. (2021): Canonical T cell receptor docking on peptide-MHC is essential for T cell signaling. In: *Science (New York, N.Y.)* 372 (6546). DOI: 10.1126/science.abe9124.

Zehn, Dietmar; Lee, Sarah Y.; Bevan, Michael J. (2009): Complete but curtailed T cell response to very low affinity antigen. In: *Nature* 458 (7235), S. 211–214. DOI: 10.1038/nature07657.

Zhang, Yikai; Liu, Zhipeng; Wei, Wei; Li, Yangqiu (2022): TCR engineered T cells for solid tumor immunotherapy. In: *Exp Hematol Oncol* 11 (1), S. 38. DOI: 10.1186/s40164-022-00291-0.

Zhao, Yangbing; Bennett, Alan D.; Zheng, Zhili; Wang, Qiong J.; Robbins, Paul F.; Yu, Lawrence Y. L. et al. (2007): High-affinity TCRs generated by phage display provide CD4+ T cells with the ability to recognize and kill tumor cell lines. In: *Journal of immunology (Baltimore, Md. : 1950)* 179 (9), S. 5845–5854. DOI: 10.4049/jimmunol.179.9.5845.

Zhong, Shi; Malecek, Karolina; Johnson, Laura A.; Yu, Zhiya; Vega-Saenz de Miera, Eleazar; Darvishian, Farbod et al. (2013): T-cell receptor affinity and avidity defines antitumor response and autoimmunity in T-cell immunotherapy. In: *Proceedings of the National Academy of Sciences of the United States of America* 110 (17), S. 6973–6978. DOI: 10.1073/pnas.1221609110.

Zinkernagel, R. M.; Doherty, P. C. (1974): Restriction of in vitro T cell-mediated cytotoxicity in lymphocytic choriomeningitis within a syngeneic or semiallogeneic system. In: *Nature* 248 (5450), S. 701–702. DOI: 10.1038/248701a0.

8. Danksagung

Zunächst möchte ich mich bei Prof. Dirk Busch und der gesamten AG Busch für dieses spannende Projekt und die herzliche Aufnahme in die Welt der Wissenschaft bedanken. Als Mediziner gab es viel aufzuholen und alle Kollegen haben mich dabei bedingungslos unterstützt.

Die ersten Schritte haben mir Magdalena Nauerth, Florian Voit, Immanuel Andrä, und Katherine Molter beigebracht und ihre große Geduld weiß ich sehr zu schätzen. Erstere hat mit ihrer Vorarbeit und genialen Ideen den Grundstein für mein gesamtes Projekt gelegt und mir alle Grundlagen der TCR k_{off}-rates vermittelt. Kilian Schober hat mich und mein Projekt schließlich adoptiert, immer wieder auf Kurs gebracht, und mich bis zum Schluss exzellent betreut; dafür auch ein herzliches Dankeschön. Prof. Busch hat derweil die Fäden in der Hand behalten, mich auf die wichtigen Dinge fokussiert und auch in den Details beraten ohne mir dabei die Freiräume zu nehmen. Dieses Engagement und das freundschaftliche Verhältnis weiß ich sehr zu schätzen.

Das Rückgrat meines Projekts war jedoch die einzigartige Zusammenarbeit im Institut. Bei technischen Fragen konnte ich mich immer auf die Expertise von Immanuel Andrä, Anna Hochholzer, Monika Hammel, Ingeborg Hensel und Katherine Molter verlassen. Bei Analysen und Methodik waren Diskussionen mit Kilian Schober, Manuel Effenberger, Thomas Müller, Marten Plambeck, Fabian Mohr und Simon Grassmann von unschätzbarem Wert. Außerdem haben Anna Purcarea und Sebastian Jarosch mit ihrer einzigartigen Expertise und Experimenten einen herausragenden Beitrag für dieses Projekt geleistet. Für das freundschaftliche Miteinander und die unzähligen Hilfeleistungen möchte ich mich auch bei Andreas Wanisch, Atefeh Kazeroonian, Bianca Weißbrich, Elvira D'Ippolito, Jonas Mir, Kristof Wing, Lena Appel, Lorenz Kretschmer, Lorenz Mihatsch, Lynette Henkel, Mortimer Svec, Patrick Huppertz, Sarah Dötsch, Shwetha Lakshmipathi, Simon Fräßle und Susi Dürr bedanken.

Die unermüdliche Arbeit der Mitarbeiter des Tierstalls, der Veterinärmedizin und der Spülküche macht Projekte wie meines überhaupt erst möglich und dafür möchte ich mich ebenfalls herzlich bedanken.

Besonders hervorheben möchte ich die selbstlose Unterstützung durch Katherine Molter, die ich dank diesem Projekt kennen und lieben gelernt habe. Ohne sie hätte ich weder meine wichtigsten Experimente noch die Vollendung meiner Dissertation schaffen können. Thank you so much!

Zuletzt möchte ich noch meiner Familie danken, die mich stets auf meinem Weg unterstützt und meinen Werdegang ermöglicht hat. Meine Gedanken sind besonders bei meinem Vater, der den Abschluss meiner Promotion leider nicht mehr miterleben kann.